UNIVERSITY OF UDINE - ITALY

Department of Physics

Ph.D. Thesis

SEARCHING FOR INTRINSIC ANISOTROPIES OF THE UNIVERSE THROUGH THE STUDY OF KAON LIFETIMES

Supervisors:

Prof. ALESSANDRO DE ANGELIS

Dott. MARIO ANTONELLI

Dott. MARCO DREUCCI

Candidate:

MARIA MICHELA DE MARIA

Doctorate of Philosophy in Mathematics and Physics

XXI cycle

AY 2009/2010

Preface and Summary of my work

This thesis is divided in two parts: the first one is related to the work I did within the KLOE Collaboration at the Laboratori Nazionali di Frascati of INFN, and the second one to the work made within the MAGIC Collaboration.

1. The first part describes two analysis works: the measurement of the lifetime of the K_S^0 meson (the short lived neutral kaon) performed with KLOE, and a test of the isotropy of the lifetimes of K_S^0 parallel and antiparallel with respect to assigned directions in a frame of reference fixed to the solar system. An outlook of the first part of this thesis follows.

   - In Chapter 1 a brief discussion of the phenomenology of the neutral kaon system is presented.
   - In Chapter 2 the KLOE detector and its performance are described.
   - In Chapter 3 the Special theory of Relativity is briefly discussed, together with some test theories and experiments.
   - In Chapter 4 the measurement of the K_S^0 lifetime is described, together with a test of the isotropy of the lifetimes of K_S^0 parallel and antiparallel with respect to assigned directions in a frame of reference fixed to the solar system.
   - Appendix A contains a brief description of the algorithms used in the analysis of the lifetime of K_S^0 in the galactic frame, and in particular of the calculations made to transform directions in the laboratory frame to directions fixed to the solar system.
   - Appendix B contains tables summarizing the results of the main experiments performed to test Special Relativity.

2. MAGIC is a telescope devoted to the detection of gamma-rays of astrophysical origin in the energy region above 30 GeV (Very-High-Energy). It is located in the Observatory of Roque de Los Muchachos, in the Canary Island of La Palma. The second part describes the work I did in MAGIC; I mostly contributed as a system administrator of the computers dedicated to the data acquisition in La Palma.

After a brief introduction to the MAGIC telescopes, a summary of the recent results obtained, and a description of the computer systems that support the MAGIC data acquisition, are presented.

An article entitled "Measurement of K_S^0 Lifetime" has been written [KLOE10a] from the work documented in the first part of the thesis. The article presents the third most precise measurement of the K_S^0 lifetime in the literature and the most precise limit on a possible asymmetry; the draft is circulating within the KLOE collaboration, and it is likely to be submitted to an international journal after the revision by the internal referees.
I am also in the Author list of 11 collaboration publications by the MAGIC collaboration (see appendix B).

Contents

First Part

Abstract

The aim of physics is the observation and explanation of natural phenomena to improve the understanding and description of Nature. A new success in theory, experiment or technology, can trigger new impulses on other areas. When Albert Einstein presented Special Relativity [Einst1905] in his work "Zur Elektrodynamik bewegter Körper", he provided a new view on time and space.

Many experiments were then carried out to look for deviations from the predictions of Special Relativity, searching for a preferential reference system (the ether or aether) and in general for a possible anisotropy of physical processes. This anisotropy is investigated by using beams of light travelling in closed path, or by making cosmic observations of one-way trips of light in different seasons, or at different hours of the day. The closed-path experiments are insensitive to effects linear in the velocity of the laboratory with respect to ether; for most of the scientists both classes of experiments would fail to detect an ether such that the velocity of light is constant in modulus for every frame.

The one-way constancy of the speed of light has been recently questioned [AbGue05]. Several non-relativistic theories assume that there is only one frame where the one-way speed of light in vacuum c is the same in all directions. This frame is identified with the rest system. The one-way speed of light in vacuum in moving inertial frames is not c (the two-way speed of light is). Furthermore, as in Newton's theory, simultaneity is absolute, contrary to Einstein's relativity. An alternative derivation of the effects is described in the work of Aronson et al. [Aron83] and De Angelis and Smalska [DeSm96]. A crucial test could be measuring the one-way time dilation for particles traveling with different direction with respect to the ether [DeSm96] – other tests of time dilation using particle lifetimes do not exclude that the lifetime depends on the direction of flight.

In this work, from a sample of more than 100 million K^0_S decays recorded by the KLOE detector at the DAΦNE accelerator in Frascati, a test of the isotropy of time dilation is done by comparing the lifetimes of K^0_S parallel and antiparallel with respect to assigned

directions in a frame of reference fixed to the Solar System. A possible anisotropy is tested with respect to different directions, with unprecedented sensitivity.

This result sets limits to non-relativistic theories, and to possible anisotropical interactions of neutral kaons with the matter in the universe, in a domain that is to the knowledge of the authors unexplored, and suggests a new technique of investigation of anisotropies.

The analysis has lead also to one of the most precise measurements of the K_S^0 lifetime in the literature.

1

The Standard Model and the neutral kaon system

1.1 Introduction

In this chapter a brief overview of the Standard Model is given, focusing on the areas relevant to this thesis, in particular for the study of the K meson. The Standard Model (SM) is a Quantum Field Theory that attempts to explain all the phenomena of particle physics in terms of the properties and interactions of a small number of *elementary* particles. According to SM, all matter in the Universe is made up of three distinct types of particles: two spin -$\frac{1}{2}$ families of fermions called *leptons* (e, ν_e, μ, ν_μ, τ, ν_τ) and *quarks* (u, d, s, c, b, t), and one family of spin-1 bosons called gauge bosons which act as force carriers in the theory. In addition at least one spin-0 particle, called the Higgs boson, is postulated to explain the origin of mass.

The constituent particles of the Standard Model and some of their properties are listed in Table 1.1, 1.2. The gauge bosons and the forces they mediate are listed in Table 1.3.

The Standard Model requires the W^+, W^-, Z, and γ spin-one or gauge bosons to mediate the electroweak force and eight massless gauge bosons called gluons that are color anticolor bound states.

1.1.1 The fundamental particles

According to the Standard Model, there are 24 fundamental matter particles (see Tables 1.1 and 1.2) – six quarks (the up, down, strange, charm, bottom and top quarks)

coming in three different colors and six leptons (the electron, muon, tau, and their neutrins) [PDG08].

Table 1.1: Properties of the quarks.

Name	Symbol	Charge
Up Quark	u	$+2/3$
Down Quark	d	$-1/3$
Strange Quark	s	$-1/3$
Charm Quark	c	$+2/3$
Bottom Quark	b	$-1/3$
Top Quark	t	$+2/3$

Table 1.2: Properties of the leptons.

Name	Symbol	Mass	Charge
Electron	e	$0.511\,\mathrm{MeV}/c^2$	-1
Muon	μ	$105.6\,\mathrm{MeV}/c^2$	-1
Tau	τ	$1.777\,\mathrm{GeV}/c^2$	-1
Electron Neutrino	ν_e	$< 3\,\mathrm{eV}/c^2$	0
Muon Neutrino	ν_μ	$< 0.17\,\mathrm{MeV}/c^2$	0
Tau Neutrino	ν_τ	$< 18\,\mathrm{MeV}/c^2$	0

The strong force binds the quarks together into composites. A combination of a quark and an antiquark is a meson (e.g., a pion or kaon), and a combination of three quarks is a baryon (e.g., a proton or neutron). Mesons and baryons are collectively called hadrons. While the vast majority of the everyday life matter consists only of up and down quarks, the other four quarks are equally as fundamental. The essential difference is only in their greater masses.

The leptons do not interact via the strong force. Instead each lepton generation consists of a lepton which interacts via both the weak force and the electromagnetic force, with negative electric charge and a second type of lepton, called neutrino, which interacts only via the weak force and as such has zero electric charge. The muon and tau differ from the electron only in mass. Neutrinos are emitted during weak processes and only interact weakly, and therefore are extremely difficult to detect. All of these fundamental fermions have anti-matter partners.

1.1.2 The fundamental forces

The fundamental particles interact through four different forces. The forces of the Standard Model are all described by the exchange of force-carrying particles, the gauge bosons (see Table 1.3).

Table 1.3: Properties of the gauge bosons.

Name	Symbol	Mass	Charge
Photon	γ	0	0
W Boson	$W^{\pm}$	$80.4\,\mathrm{GeV}/c^2$	± 1
Z Boson	Z^0	$91.2\,\mathrm{GeV}/c^2$	0
Gluon	g	0	0

Gravity is the force of attraction between massive bodies. However, due to the smallness of the masses of the fundamental particles, the force of gravity between any of them is negligible.

Electromagnetism is the force responsible for the repulsion between like charges, the attraction between opposite charges, the deflection of charged particles in magnetic fields, etc. In the Standard Model, the force is due to the exchange of virtual photons, which interact with any charged body. In addition, in Quantum Electrodynamics (QED), the Standard Model theory of electromagnetism, photons can convert to electrons and positrons, an electron can emit a photon, electrons and positrons can annihilate into photons, etc.

The strong force acts only on quarks, and is due to the exchange of gluons. Similar to the electric charge for electromagnetism, the strong force proceeds through a charge of its

own, the "color" charge. But unlike in electromagnetism, where the photon has no electric charge of its own, gluons do carry color charge, allowing them to interact among themselves and thus creating a much more complex situation. The strong force binds quarks tightly into hadrons, so tightly that the quarks never appear unbound. The Standard Model theory of the strong force is Quantum Chromodynamics (QCD).

Finally, the weak force affects all of the fundamental particles. It is carried by the $W^{\pm}$ and Z bosons. Nuclear beta decay is the most familiar example of this force, where one of the down quarks of a neutron converts to an up quark by emitting a W^{-}, which subsequently decays to an electron and an electron antineutrino.

The weak and electromagnetic forces are explained in the Standard Model as arising from the same fundamental interaction, the electroweak interaction. The electroweak theory [Quigg01] requires a new particle, called the Higgs Boson. The search for the Higgs Boson, the last of the Standard Model particles to be experimentally undiscovered, is one of the major efforts of contemporary experimentally high energy physics.

1.2 C, P, T symmetries

Symmetry is an ancient concept that has its roots in Greek philosophy and esthetics. The $\sigma\upsilon\mu\mu\varepsilon\tau\rho\iota\alpha$ is made up of two separate words $\sigma\upsilon\nu$ and $\mu\varepsilon\tau\rho\upsilon\nu$ in ancient Greek had the meaning of well proportioned, and as such was related to harmony and beauty. But symmetry immediately acquired a further, more general meaning, with commensurability representing a particular case: that of a proportion relation, grounded on (integer) numbers, and with the function of harmonizing the different elements into a unitary whole (Plato, Timaeus).

Symmetry is a strong tool for the development of science. From the very first days of Natural Philosophy, (Pythagoras VI century BC), symmetry has given insight into the laws of physics and the nature of the Cosmos. These insights found always a constant evolution with time, and it is worth to briefly point out some landmarks.

Isaac Newton and G.W. Leibniz in XVII century formulated the infinitesimal calculus and developed the analytic notation, which replaced geometry as the essential tool to study physical systems. In the following century J.-L. Lagrange and W. Hamilton developed the Lagrangian formalism that permits to incorporate in all the symmetries of the system

and to reveal the deep connections with the conservation laws. At the same time, mathematicians P. Ruffini, N. Abel, and E. Galois (who first used the term) defined the Group Theory having argued that it is the correct formalism for treating symmetries [Weyl83].

At current day, symmetry is one of the chief concepts of modern physics and mathematics. In her paper "Invariante Varlationsprobleme"[1] Emmy Noether proved two theorems and their converses which revealed the general connection between symmetries and conservation laws in physics. They conduct to a deeper understanding of laws such as the principles of conservation of energy, angular momentum, etc., and also were instrumental in the great discoveries of gauge field symmetries of the XX century.

The two tools of theoretical development of the XX century, Relativity and Quantum Theory, are strongly associated to the notions of symmetry. The image of the balance is linked with the concept of bilateral symmetry of modern time and grounded on a equality relation between elements that are opposed. In a famous lesson Feynman [Feyn63] said that in physics the word symmetry is used with a special meaning, and therefore needs to be defined. Hermann Weyl has given this definition of symmetry: a thing is symmetrical if one can submit it to a certain operation and it appears exactly the same after this operation. Reflection symmetry has a precise definition in terms of invariance. Symmetries in physics come in a number of different varieties, distinguished by terms as "global", "local", "continuous", "discrete". The spatial and temporal invariance of mechanical laws was known and used for a long time in physics, such in the Galilean invariance of Newtonian mechanics, and in the Lorentz invariance of the Special Theory of Relativity. Global spacetime symmetries are intended to be valid for all the laws of nature for all the processes that unfold in the spacetime.

In this context, symmetries indicate specific properties of theoretically formulated laws of physics. Because symmetries establish simple and reliable relations between the abstract law and specific, observable quantities, they are very useful for the experimental investigation of the laws. The symmetry properties of the experimental data directly reflect symmetry properties of the physical law. The study of observed symmetries have often been used as a tool in the construction of theoretical models.

[1] presented to the July 16, 1918 meeting of the Könighche Gesellschaft der Wissenschaften zu Göttingen by Felix Klein presumably because Noether was not a member of the Gesellschaft.

Some of the most fundamental symmetries in physics are the space-time symmetries of Lorentz transformations, which preserve the laws of physics under boosts and rotations, and CPT, the combination of charge conjugation (C), parity inversion (P) and time reversal (T). CPT appears experimentally to be an exact symmetry, while C, P and T appear to be individually violated. If CPT is an exact symmetry, the violation of T is equivalent to the violation of CP.

The property of the CPT symmetry entails the existence of antimatter, and the equality of the masses and the decay widths of a particle and of its antiparticle.

The CPT symmetry is not implied by quantum mechanics (QM): it has to be implemented as an extra property of the Hamiltonian in the Schrödinger equation.

1.3 The Standard Model

In the late 1960s Weinberg, Salam, and Glashow described how it would be possible to treat electromagnetic and weak interactions as different aspects of a single electroweak interaction, with a single coupling given by the elementary electric charge, e. In 1972 Gell-Mann and Fritzsch first introduced the term "color" and the first proposal of what is known as Quantum Chromodynamics (QCD) [GelMa64] was given in the parallel session talk of Fritzsch and Gell-Mann at the XVI International Conference on High Energy Physics held at the University of Chicago [Adl04].

The Standard Model provides a framework for the unification of the Glashow-Salam-Weinberg Model [Glash61] of electroweak interaction and QCD for strong nuclear forces. It is a non-abelian gauge theory based on the $SU(3)_{Colour} \times SU(2)_{Weak} \times U(1)_{EM}$ symmetry group, which describes strong, weak and electromagnetic interactions.

The Standard Model Lagrangian can be written as

$$\begin{aligned} \mathcal{L}_{SM} &= \underbrace{\mathcal{L}_H(\phi)}_{\text{Higgs}} + \underbrace{\mathcal{L}_G(W,Z,G)}_{\text{Gauge}} + \underbrace{\sum_{\psi=\text{fermions}} \bar{\psi} i \not{D} \psi}_{\text{gauge-fermion}} \\ &\quad + \underbrace{\sum_{\psi,\psi'=\text{fermions}} g_{\psi\psi'} \bar{\psi} \phi \psi'}_{\text{Yukawa}} \quad . \end{aligned} \tag{1.1}$$

The electromagnetic force is described by the 1-dimensional abelian unitary group $U(1)_{EM}$,

whereas the other two forces are described by non-abelian special and unitary transformations: the weak force by $SU(2)_{Weak}$, QCD by $SU(3)_C$. The Lagrangian of a gauge theory is invariant under local "gauge" transformations of a symmetry group. Such a symmetry can be used to generate dynamics - the *gauge interactions*. The prototype gauge theory is quantum electrodynamics (QED) with its abelian $U(1)$ local symmetry.

The gauge group of strong interactions is the non-abelian group $SU(3)_C$ which has eight generators. These correspond to the gluons that communicate the strong force between objects carrying color charge (therefore the "C" as subscript). Also the gluons themselves are colored and interact directly with each other.

Electromagnetic and weak forces are unified by introducing two symmetries, $U(1)_Y$ in the hypercharge-space and $SU(2)_L$ acting on isospin-$\frac{1}{2}$ doublets containing only the left handed components ("L" subscript) of matter fields. Force carriers, i.e. vector bosons of spin-1 are associated to these two group transformations; their mass eigenstates are the photon, the W and the Z bosons.

Fermions are ordered into three families. Each of these contains one left-handed lepton doublet, one left-handed quark doublet, one right-handed charged lepton singlet and two right-handed quark singlet. Singlets and doublets refer to their behaviour under $SU(2)_L$. Left and right-handedness refers to the helicity of the field, that is the projection of its spin along its momentum.

Quarks:	$\begin{pmatrix} u \\ d' \end{pmatrix}_L$	$\begin{pmatrix} c \\ s' \end{pmatrix}_L$	$\begin{pmatrix} t \\ b' \end{pmatrix}_L$
	u_R	c_R	t_R
	d_R	s_R	b_R
Leptons:	$\begin{pmatrix} \nu_e \\ e^- \end{pmatrix}_L$	$\begin{pmatrix} \nu_\mu \\ \mu^- \end{pmatrix}_L$	$\begin{pmatrix} \nu_\tau \\ \tau^- \end{pmatrix}_L$
	e_R	μ_R	τ_R

All these particles are accompanied by their corresponding antiparticle with the same mass and opposite charge. The masses and flavour quantum numbers of the three families are different, but they have the same properties under gauge interactions.

1.4 Transitions and the CKM matrix

Quarks are ordered into three families. The strong interaction conserves the flavor of quarks; the weak interaction, instead, can change the quark content. Only flavor changing charged currents exist.

The amplitude of transitions between different quarks is given [Cab63, KM73] by the Cabibbo–Kobayashi–Maskawa (CKM) matrix ($V_{CKM} = (V_{ij})$):

$$\begin{pmatrix} V_{ud} & V_{us} & V_{ub} \\ V_{cd} & V_{cs} & V_{cb} \\ V_{td} & V_{ts} & V_{td} \end{pmatrix} . \tag{1.2}$$

The diagonal elements of V_{CKM} represent coupling between quarks of the same generation and the smaller, off diagonal terms represent coupling between quarks of different generations.

The CKM-matrix V_{CKM} is a general complex unitary matrix so, in theory, it should depend on 9 real parameters. However, part of these independent parameters can be eliminated by a new definition of the phases of the quark fields. The matrix V_{CKM} thus contains four independent parameters.

In terms of the four free constants of the CKM matrix, various parameterizations are possible. A popular one is that of Wolfenstein, written in the form of an expansion in $\lambda = \sin\theta_C$ (the sine of the Cabibbo angle, which is the parameter coupling the s and the u quarks).

To order λ^4 the CKM matrix in the Wolfenstein parametrization is

$$\begin{pmatrix} 1-\frac{\lambda^2}{2} & \lambda & A\lambda^3(\rho - i\eta) \\ -\lambda & 1-\frac{\lambda^2}{2} & A\lambda^2 \\ A\lambda^3(1-\rho-i\eta) & -A\lambda^2 & 1 \end{pmatrix} , \tag{1.3}$$

where λ can be measured accurately in K decays (involving the $\bar{s} \to u$ transition), A is determined from semileptonic B decays to charmed particles with an accuracy of $\simeq 6\%$, and ρ and η are least known.

In the Standard Model framework the V_{CKM} matrix is unitary ($V^\dagger V$=1). It means that the only allowed transitions in neutral current interactions that involve the Z boson are $d \leftrightarrow d$ $s \leftrightarrow s$ etc., while transition such $d \leftrightarrow s$ do not occur.

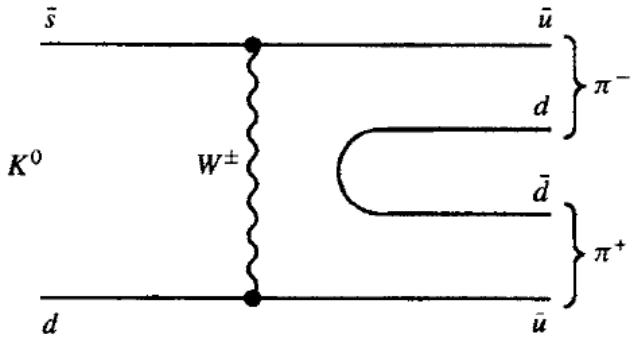

Figure 1.1: Feynman diagram of the K^0 decay into $\pi^+\pi^-$.

The current knowledge of the elements of the CKM matrix is summarized in [PDG08]:

$|V_{us}| = 0.2255 \pm 0.0019$ $\quad$ $|V_{cb}| = (41.2 \pm 1.1) \times 10^{-3}$,

$|V_{ud}| = 0.097418 \pm 0.00027$ $\quad$ $|V_{cd}| = 0.230 \pm 0.011$

$|V_{cs}| = 1.04 \pm 0.06$ $\quad$ $|V_{ub}| = (3.93 \pm 0.36) \times 10^{-3}$

$|V_{ts}| = 38.7 \pm 2.3$, $\quad$ $|V_{td}| = (8.1 \pm 0.6) \times 10^{-3}$

$|V_{tb}|$ 0.74 ± 0.011.

1.4.1 The matrix element V_{us}

This thesis is mostly related to the K^0_S decay. The dominant process in the decay is the transition of a s quark into an u quark; the relevant element in the transition is thus V_{us} (Figure 1.1).

The matrix element $|V_{us}|$ is best determined from analysis of the semileptonic K decays, in particular

$$K^0_L \to \pi e \nu \,.$$

This yields the value $|V_{us}| = 0.2255 \pm 0019$ [PDG08].

1.4.2 CP symmetry violation in the Standard Model

CP violation requires the presence of a complex phase. More specifically, CP violation is present if $\eta \neq 0$ in (1.3).

The CKM mechanism for CP violation requires several conditions. All the CKM-matrix

elements must be different from zero and the quarks of a given charge and different families can not have the same mass. In addition, CP can be violated only in processes where the three generations are involved.

The violations of the CP symmetry are small since the CP-violating observables must be proportional to a given combination of CKM-matrix elements that is itself small [Jarlsk85]

$$J_{CP} = \mathrm{Im}(V_{ai}V_{bj}V_{aj}^{*}V_{bi}^{*}) = \eta A^2\lambda^6 + \mathcal{O}\left(()\,\lambda^8\right) \leq 10^{-4}\,. \tag{1.4}$$

1.5 K mesons

The neutral K mesons have played an important role in the history of elementary particle physics and have been a rich source of phenomena associated with their production, decay and propagation in both vacuum and matter. The study of the features of the K mesons system and of kaon decays has been a powerful tool to achieve results of unique importance in the development of particle physics.

Kaons can be produced in pairs through strong interactions of non strange particles (i.e., with total strangeness $S = 0$), but their decay can occur only through the weak interactions into non-strange particles (violating strangeness).

Gell-Mann and Pais suggested to represent the decay eigenstates of neutral kaons as eigenstates of the charge conjugation operator C. At the time, charge conjugation was supposed to be a valid symmetry for all the interactions. Since these eigenstates would decay through different channels, they should have different lifetimes. In particular the state with C = -1 (K_L^0) would not decay into the 2π state, and would therefore have a longer lifetime[2] than the state with C = + 1(K_S^0).

In 1956 a long-lived neutral particle consistent with the hypothesis of a K^0-type particle with a lifetime $\tau > 1$ ns was observed. In spite of that, the decisive proof for the theory proposed by Gell-Mann and Pais came from regeneration experiments.

In 1957, experiments suggested by Lee and Yang [LeYo56] proved the revolutionary hypothesis of parity violation in weak interactions [Wu57,Eisl57,Garw57]. Nevertheless Lee, Oehme and Yang [LeYo56] pointed out that making only the assumption of CPT invariance, the main features of the GellMann-Pais theory would remain. At the same time,

[2]The main reason for this difference is the different phase space available for the decay.

Landau [Land57] suggested the validity of the combined symmetry CP of space-inversion and charge-conjugation, noting that the GellMann-Pais theory would remain the same with the replacement of C with CP.

The interactions involving the $K^0\bar{K}^0$ pairs can be understood as follows. In strong-production processes only the eigenstates of the strong Hamiltonian are produced, namely $|K^0\rangle, |\bar{K}^0\rangle$. However these states are superposition of the $|K_1^0\rangle, |K_2^0\rangle$ which are eigenstates of the weak Hamiltonian:

$$\begin{aligned} |K_1^0\rangle &= (|K^0\rangle + |\bar{K^0}\rangle)/\sqrt{2} \qquad CP|K_1^0\rangle = +|K_1^0\rangle \\ |K_2^0\rangle &= (|K^0\rangle - |\bar{K^0}\rangle)/\sqrt{2} \qquad CP|K_2^0\rangle = -|K_2^0\rangle\,. \end{aligned} \tag{1.5}$$

In 1963, Cronin and Fitch began a series of experiments to investigate the behavior of neutral K mesons to know more about the process by which a beam of neutral K-mesons could be separated into two parts, one consisting of short-lived neutral K-mesons that decay into two π-mesons and another consisting of long-lived neutral K-mesons that decay into three π-mesons [Belt05, Gatti02].

The experiments soon provided supporting evidence for the concept of CP violation. Until 1964, it was believed that, although weak interactions were known to violate C and P invariance separately, CP symmetry was respected.

In 1964 Christenson, Cronin, Fitch and Turlay [Christ64] announced the discovery of the decay into two pions for the long-lived kaon. They established a frequency of the decay:

$$BR(K_L^0 \to \pi^+\pi^-) = (2.0 \pm 0.4) \times 10^{-3} \tag{1.6}$$

showing that CP was not conserved in the weak decays of kaons. This is called indirect CP violation, since it can be explained by an oscillation in-flight of the K_L^0 into a K_S^0.

The first evidence for direct CP violation (i.e., not due to the mixing between K_L^0 and K_S^0) was found by CERN/NA31 in 1988; subsequent tests were performed at fixed target. Since summer 1999 at the Frascati Laboratory of INFN the KLOE experiment has started its data taking for studying CP violation in K physics. The KLOE experiment, which will be described in detail in the next Chapter, has an important role because it is a collider experiment, based on a completely different technique with respect to the fixed target experiments. The K_S^0 and K_L^0 mesons are generated simultaneously from the decay of the ϕ meson, that is produced in $e^-\ e^+$ collisions at $\sqrt{s} = 1020$ MeV.

Considering that K_S^0 and K_L^0 are always generated in pairs the identification of a K_L^0 (K_S^0) provides also an elegant tag for the K_S^0 (K_L^0). For instance K_L^0 tagging is performed by the identification of a $K_S \to \pi^0\pi^0$ or a $K_S \to \pi^+\pi^-$.

1.6 K_S^0 lifetime

The decades after the discovery of the failure of CP symmetry in the neutral kaon system (1964, Nobel Prize in 1980) are rich of experiments studying the properties of the neutral kaon system and the kaon decays. The consequences of such experiments are not only a more and more precise measurement of CP parameters, but also the estimation of many other kaon parameters such as the mass difference Δm for the mass eigenstates, the branching ratios and the lifetimes $\tau_{\mathrm{L,S}}$ for the K_L^0 and the K_S^0.

A historical measurement of K_S^0 lifetime was made by Elihu Boldt, David Caldwell and Yash Pal [BCP58] observing the decay with a multiplate cloud chamber at the Brookhaven Cosmotron.

The K_S^0 lifetime is presently known with a relative precision of about 0.5 parts per thousand. The PDG reports two average values [PDG08] depending on whether or not the CPT symmetry is assumed.

$$\begin{aligned} \tau_S &= (89.53 \pm 0.05)\ \mathrm{ps} \qquad \text{Assuming CPT} \\ \tau_S &= (89.58 \pm 0.05)\ \mathrm{ps} \qquad \text{Not assuming CPT} \quad . \end{aligned}$$

The most precise result (not used in the PDG 2008) is a very recent measurement of τ_{S} from the KTEV experiment [Wor09], which individually has the same accuracy of the world average (and it includes all the KTEV results):

$$\tau_S = (89.62 \pm 0.05)\,\mathrm{ps}\,.$$

The second more accurate result uses the NA48 data, and is of 89.60 ± 0.07 ps summing in quadrature the statistical and systematic uncertainties.

The measurement of the neutral kaon decay parameters requires a source of K_L^0 and K_S^0 decays and a detector to reconstruct the final states $\pi^-\ \pi^+$ and $\pi^0\pi^0$. For this purpose different apparatus and different techniques of analysis have been conceived, often allowing careful checks of the results from experiments with independent sources of systematic errors.

2

KLOE

2.1 Introduction

In 1989 the Istituto Italiano di Fisica Nucleare, INFN, decided to construct an e^+e^- collider designed to operate at around 1020 MeV, slightly above the mass of the ϕ meson. The ϕ decays mostly to pairs kaons, neutral or charged. This ϕ–factory, called DAΦNE, is located at the Laboratori Nazionali di Frascati, LNF, INFN's high energy physics laboratory near Rome [KLOE08].

2.1.1 DAΦNE

The DAΦNE layout is shown in Fig. 2.1. DAΦNE is housed in the ADONE building at LNF, see Fig. 2.2. The collider consists of two "rings" in which 120 bunches of electrons and positrons are stored. Each bunch collides with its counterpart once per turn. The electrons and the positrons are injected in the rings at final energy, $\sim$510 MeV. The collider luminosity $\mathcal{L}$ is an intrinsic characteristic of any accelerator and can be expressed in terms of the beam parameters by:

$$\text{event rate} = \mathcal{L} \times \text{cross section}.$$

A ϕ factory is a copious source of tagged and monochromatic kaons, both neutral and charged: indeed the dominant decay modes of ϕ meson are charged kaon pairs (49%), neutral kaon pairs (34%), $\rho\pi$ (15%), and $\eta\gamma$ (1.3%).

Electrons and positrons collide at an angle of π-0.025 radians; thus the ϕ produced in the collisions move in the laboratory system toward the center of the storage rings with a momentum of about 13 MeV corresponding to $\beta_\phi \sim 0.015$, $\gamma_\phi \sim 1.0001$. K mesons from

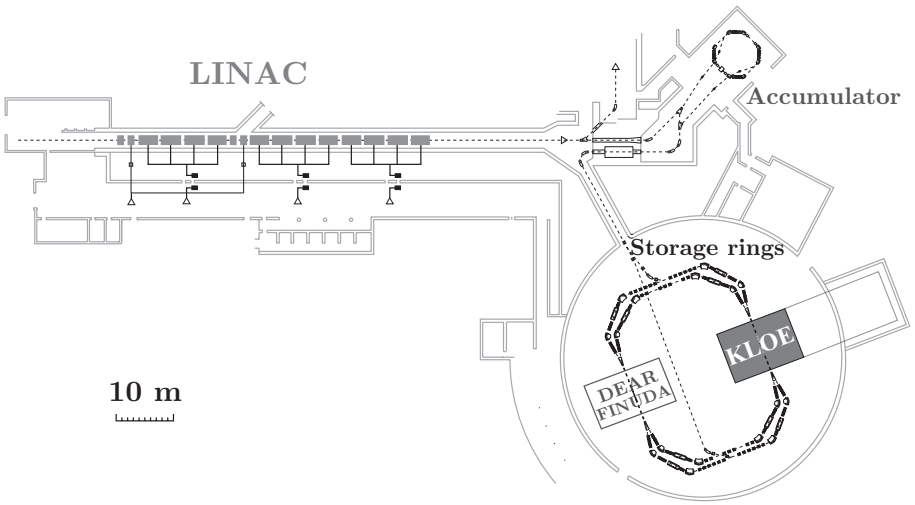

Figure 2.1: The DAΦNE complex.

Figure 2.2: The Adone building.

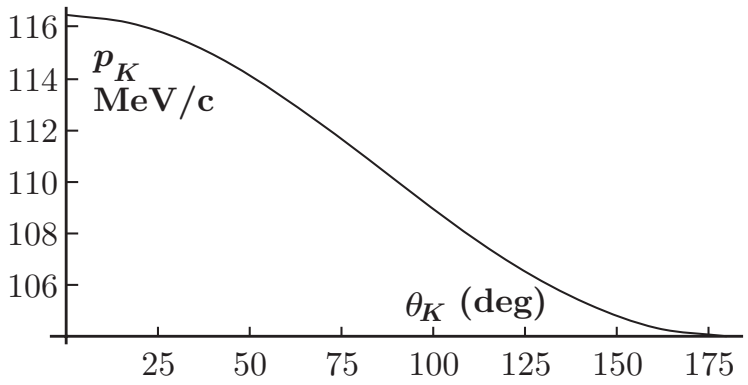

Figure 2.3: Momentum in the laboratory vs. angle to the x-axis for K^0 mesons.

ϕ-decay are therefore not monochromatic in the laboratory (Fig. 2.3). The momentum of neutral kaons varies between 104 and 116 MeV and is a single valued function of the angle between the kaon momentum in the laboratory and the ϕ-momentum, i.e., the x-axis[1]. The knowledge of the kaon direction to a few degrees allows to return to the ϕ center of mass, Fig. 2.3. The mean momentum of charged kaons is 127 MeV.

2.1.2 KLOE

The KLOE detector at DAΦNE, the Frascati ϕ-factory, has started taking data in April 1999 and, by the end of '99, collected a total integrated luminosity of 2.4 pb^{-1}, corresponding to $\sim$8 millions ϕ decays. In the subsequent seven years KLOE has produced data of such precision that the kaon got its definitive 21st century portrait re-mapped with high precision, 60 years after its discovery. Most KLOE data were taken during two running periods. The 2001–2002 run yielded 450 pb^{-1} of data, corresponding to approximately 140 million tagged K_S^0 decays, 230 million tagged K_L^0 decays, and 340 million tagged $K^{\pm}$ decays. The analysis of this data set is essentially complete. KLOE also took data in 2004–2005, after completion of a number of DAΦNE modifications intended to increase the luminosity. About 2000 pb^{-1} were collected, giving a fivefold increase in statistics. In total, KLOE has collected during the years 1999 - 2005 a luminosity of $\sim$2.5 fb^{-1} .

2.2 The detector

The KLOE detector (Fig. 2.4), built in the Frascati assembly building, consists of a large cylindrical drift chamber (DC), approximately 125 cubic meters (Fig. 2.4), and of a hermetic electromagnetic calorimeter (EMC). A solenoidal magnetic field of about 0.52 T[2] is provided by a superconducting coil surrounding the apparatus.

The dimensions of the apparatus have been dictated by the fact that the K_L^0 produced in the ϕ decays live in average about 51 ns. Kaons from ϕ decaying at rest, travel at approximately one fifth of the speed of light; the mean path travelled by a K_L^0, $\lambda_L = \gamma\beta c\tau$ is 3.4 m. A detector which can catch $1 - 1/e$=63% of all decaying neutral long-lived kaons

[1] In the standard detector coordinates, the x-axis lies in the horizontal plane, toward the center of DAΦNE, the y axis vertical point upwards and the z-axis bisects the angle of the of the $e^{\pm}$ beam line.

[2] It can be increased up to 0.6 T.

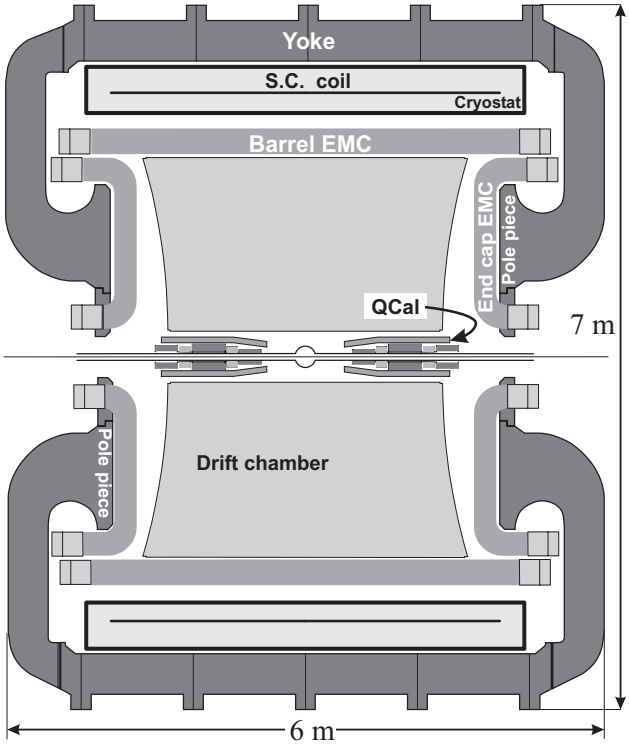

Figure 2.4: Vertical cross section of the KLOE detector, showing the interaction region, the DC, the EMC, the superconducting coil, and the return yoke of the magnet.

Figure 2.5: DC all stereo geometry.

must have a radius of some three and a half meters. A depth of two meters allows catching some 40% of those decays. Less than that in fact, since some fiducial volume is inevitably lost around the beam interaction point, IP, and some more is lost at the outer edge.

2.2.1 Drift Chamber

The KLOE DC is a cylinder with internal radius of 25 cm, external radius of 2 m and length of 3.3 m. The KLOE tracking chamber is thought to measure with great precision the properties of charged particles crossing it.

When a charged particle travels in a medium (a gas in this case) it releases some of its energy by ionization. Thus when the particle enters the DC, electrons of the ion pairs created along its trajectory drift to the positive voltage wires and from an avalanche multiplication mechanism a detectable signal appears at the wire's end. The sophisticated electronics mounted at the wire's end senses the tiny signals and provides the drift charge and time measurement; this allows to know the total energy released by the initial particle. Measuring the drift time locates the distance of the track from the anode wires which is then used to reconstruct in three dimensions the trajectory of the particles. The information on the specific energy loss is suitable to perform particle identification (PID). The actual path of the particle is altered by multiple scattering, the multiple scattering angle being $\propto 1/\sqrt{X_0}$, where X_0 is the radiation length which is roughly proportional to $1/Z^2$, in g/cm^2; while moving towards the anode, the drifting ionization undergoes diffusion, the amount of which is a function of the density of the gas mixture of the DC. In order to avoid the $K_L^0 \rightarrow K_S^0$ regeneration (K_S^0 generated from the strong interaction of a K_L^0 with the traversed medium: this effect might simulate CP-violating decays), a Helium-based gas mixture (90% He and 10% C_4O_{10}) was chosen to minimize multiple scattering and density. The average value of the radiation length in the DC volume is $X_0 \sim 900$ m, including the contribution from the wires. The mechanical structure of the chamber is constructed out of a carbon fiber composite: this material has been chosen for the low-Z and low density to minimize K_L^0 regeneration, multiple Coulomb scattering and the absorption of photons before they can reach the calorimeter. The chamber volume is delimited by an outer cylinder of 2 m radius, an inner cylinder of 25 cm radius and closed by two 9 mm thick annular endplates. The KLOE DC has ∼52,000 wires, about

12,500 of them are sense wires, the remaining ones shape the electric field in 12,500 almost square cells located on cylindrical layers around the z-axis (defined by the bisector of the two crossing beams). Particles from the ϕ decays are produced with small momenta and therefore track density is much higher at small radii. This motivated the choice of having the 12 innermost layers made up of 2×2 cm^2 cells and the remaining 48 layers with 3×3 cm^2 cells. A particle crossing the entire chamber get dozens of space points from which reconstructing a track: the track of a pion from $K_S^0 \to \pi^+\pi^-$ decay has $\sim$60 space points in average. An all-stereo geometry allows the measurement of the z coordinate. Fig. 2.5 shows the wire geometry during the DC construction. The wires form a nonzero angle with the z-axis (Fig. 2.6 left), the stereo angle ϵ. Consecutive layers have alternating signs of this angle and its absolute value increases from 60 to 150 mrad with the layer radius while keeping fixed for all the layers the difference between R_p and R_0 distances (1.5 cm), defined in Fig. 2.6 left. This design results in a uniform filling of the sensitive volume with almost-square drift cells.

In order to extract the space position from the measured drift time of the incident particle, is necessary to know the space-time relation describing the cell response. The whole DC can be described using 232 space-time relations, parametrized in terms of the angles β and $\tilde{\phi}$ defined in Fig. 2.6 right. The β angle characterizes the geometry of the cell, directly related to the electric field responsible of the avalanche multiplication mechanism. The $\tilde{\phi}$ angle gives the orientation of the particle trajectory in the cell's reference frame, defined in the transverse plane and with origin in the sense wire of the cell.

A signal localized 3-dimensionally is called hit. The procedure for the event reconstruction uses the wire geometry, space-time relations and the map of the magnetic field getting through the pattern recognition, the track fit, and the vertex fit. The pattern recognition associates hits close in space to form track candidates and gives a first estimate of the track parameters. The track fit provides the final values of these parameters minimizing a χ^2 function based on the difference between the fit and the expected drift distances, residuals, as evaluated from a realistic knowledge of the cells' response (measured drift times and space-time relation). Finally the vertex fit searches for possible secondary vertices separated from the IP, on the basis of the distance of closest approach between tracks. The hits in the DC are also associated to a charge measurement directly related to

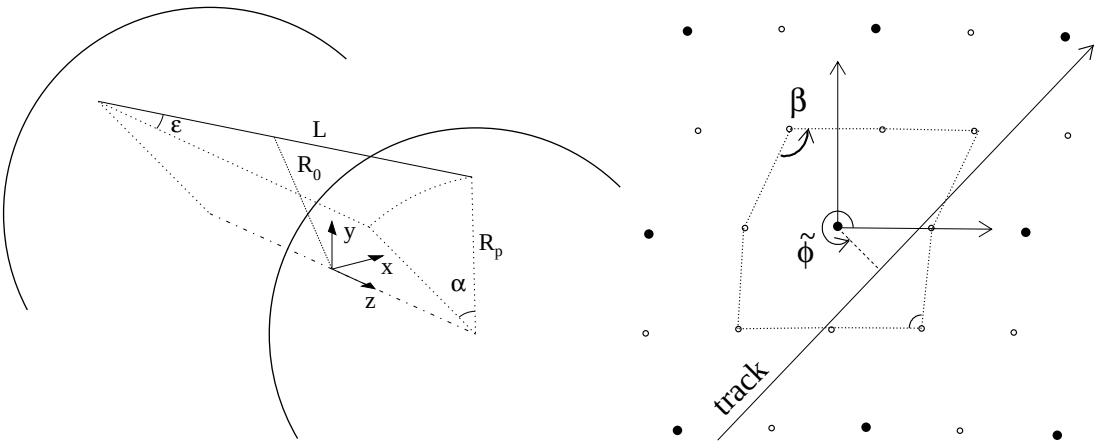

Figure 2.6: Left: Wire geometry with the definition of stereo angle ϵ between the wire of length L and the z-axis. Right: Definition of β and $\tilde{\phi}$ characterizing the shape of the cell and the angle of the incident track.

the energy released in the cell from the incident particle. The amount of charge collected depends on the particle's track length in the crossed cell. The energy deposited in a sample of finite thickness fluctuates and exhibits a Landau distribution, with a long tail at high energies. Therefore to improve the energy resolution, the energy deposited is sampled many times for each track and a truncated mean technique is used. To use the charge information for particle identification purposes it is necessary to normalize the charge to the track length and define the specific ionization dE/dx: $K^{\pm}$ tracks exhibit fro example $\sim$120 counts/cm.

The final resolution in the bending plane is better than 200 μm; the resolution on the z measurement is of $\sim$1-2 mm. The particle's momentum is defined from the curvature of its trajectory in the magnetic field with a fractional accuracy better than $\sim$0.4% for polar angles larger than 45°. The calibration of the absolute momentum scale has a fractional accuracy of few 10^{-4}, verified using several two- and three-body decays ($e^+e^- \rightarrow e^+e^-$,$e^+e^- \rightarrow \mu^+\mu^-$, $K_L \rightarrow \pi l\nu$, $K_L \rightarrow \pi^+\pi^-\pi^0$, $K^{\pm} \rightarrow \mu^{\pm}\nu$,$K^{\pm} \rightarrow \pi^{\pm}\pi^0$) covering a wide momentum range. The resolution on the specific ionization measurement, computed using $K^{\pm}$ two- and three-body decays and Bhabha scattering events, is $\sim$ 6% for pions and $\sim$ 7% for electrons, using 60 truncated samples.

The DC system's complexity requires the response of each cell to an incoming particle to

be known accurately. The cell response is a function of its geometry and of the voltage applied to the wires. Thus the position of the DC, mechanical structure as well as wires, had to be surveyed, in situ, together with the other KLOE components. To set and register the voltages applied to the wires there is the Slow Control monitoring system fully embedded in the Data Acquisition process which sends the information to the read-out electronics and controls its proper functioning. The gas mixture parameters (composition, temperature and pressure) enter directly in the space-time relations used in reconstructing the particle trajectory, to extract the space position from the measured drift time of the incident particle. The Slow Control System also monitors the gas parameters.

To ensure the stability in time of the DC performance, the system has to be calibrated periodically by acquiring samples of cosmic muons suitable for the measurement of the $\sim$200 different space-time relations. The calibration program, incorporated into the KLOE online system, automatically starts at the beginning of each run and selects about 80,000 cosmic-ray events. These events are tracked using the existing space-time relations and the average value of the residuals for hits in the central part of the cells is monitored. If the residuals exceed 40 μm then about 300,000 cosmic-ray events are collected, with about 30 Hz rate, and a new set of calibration constants is obtained. At the beginning of each data-taking period a complete calibration of the space-time relations is needed together with the measurement of the DC time offsets, the latter from some 10^7 cosmic-ray events. During data taking the DC performance is monitored using selected samples of Bhabha events.

2.2.2 ElectroMagnetic Calorimeter

The neutral pions possibly produced by kaon decays into two photons; photons might also be directly produced in K decays. Most of these photons have energies larger than a few MeV and might convert into electron-positron pairs that in turn radiate photons when traversing matter. Thus, a photon or an electron, traveling through dense materials, repeatedly undergoes radiation and pair production in cascade, until all its energy is expended in a so called shower of e^+e^- and photons. From the detection of these particles and their energy one measures the original photon's (or electron's) energy. This is done with a "calorimeter", which also usually pinpoints the position of the electromagnetic

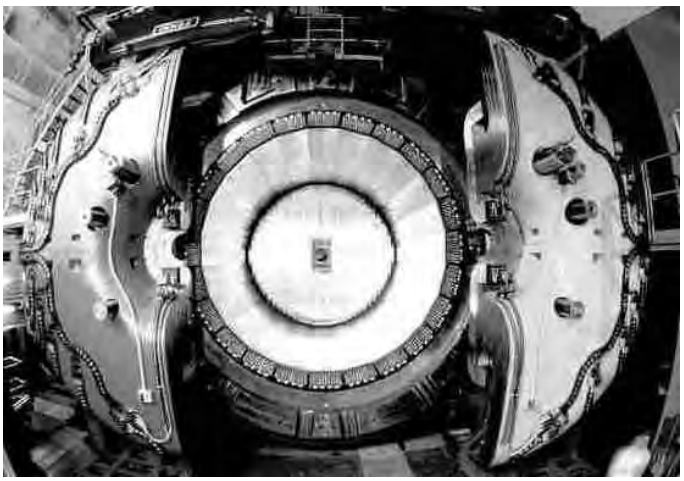

Figure 2.7: EMC viewed before DC insertion.

cascade (or shower) as well.

The KLOE calorimeter, EMC, has been designed and built to provide a hermetic detection of low energy photons (from 20 to 500 MeV) with high efficiency, a reasonable energy resolution and an excellent time resolution to reconstruct the vertex for the K_L^0 neutral decays. The calorimeter response has also to be fast since its signals are used to provide the main trigger of the events.

The EMC (Fig. 2.7) is a sandwich of lead converter layers, and of scintillating fiber sensing layers, read by photomultipliers. The fibers run parallel to the axis of the detector in the barrel, vertically in the endcaps.

The energy calibration starts by a first equalization in cell response to minimum ionizing particles (m.i.p.) at the calorimeter center and by determining the attenuation length of each single cell with a dedicated cosmic ray trigger. This is done before the start of each long data taking period. The determination of the absolute energy scale in MeV relies instead on a monochromatic source of 510 MeV photons: the $e^+e^- \to \gamma\gamma$ sample. This last calibration is routinely carried out each 200- 400 nb^{-1} of collected luminosity.

For the timing, the relative time offsets of each channel, T_i^0, related to cable lengths and electronic delays and the light velocity in the fibers are evaluated every few days with high momentum cosmic rays selected with DC information. An iterative procedure uses the extrapolation of the tracks in the calorimeter to minimize the residuals between

the expected and measured times in each cell. A precision of few tens of picoseconds is obtained for these offsets.

The high photon yield and the frequent sampling enable cluster energies to be measured with a resolution of $\sigma_E/E = 5.7\%/\sqrt{E\ (\mathrm{GeV})}$, as determined with the help of the DC using radiative Bhabha events. The absolute time resolution $\sigma_t = 57\ \mathrm{ps}/\sqrt{E\ (\mathrm{GeV})}$ is dominated by photoelectron statistics, which is well parametrized by the energy scaling law. A constant term of 140 ps has to be added in quadrature, as determined from $e^+e^- \to \gamma\gamma$, radiative ϕ decays and $\phi \to \pi^+\pi^-\pi^0$ data control samples. This constant term is shared between a channel by channel uncorrelated term and a common term to all channels. The uncorrelated term is mostly due to the calorimeter calibration while the common term is related to the uncertainty of the event T_0.

Cluster positions are measured with resolutions of 1.3 cm in the coordinate transverse to the fibers, and, by timing, of $1.2\ \mathrm{cm}/\sqrt{E\ (\mathrm{GeV})}$ in the longitudinal coordinate. These performances enable the 2γ vertex in $K_L^0 \to \pi^+\pi^-\pi^0$ decays to be localized with $\sigma \approx 2$ cm along the K_L^0 line of flight, as reconstructed from the tagging K_S^0 decay. Incidentally, the thin lead layers used and the high photon yield allows high reconstruction efficiency for low energy photons.

2.2.3 Beam Pipe and Quadrupole Calorimeter

To observe rare K_S^0 decays and $K_L^0 K_S^0$ interference with no background from $K_S^0 \to K_L^0$ regeneration, a reasonably large decay volume around the IP must remain in vacuum. The beam pipe surrounds the interaction point, with a sphere of 20 cm inner diameter, with walls 0.5 mm thick made of a Be-Al sintered compound. This sphere provides a vacuum path $\sim 10\times$ the K^0 amplitude decay length, effectively avoiding all $K_S^0 \to K_L^0$ regeneration.

Permanent quadrupoles for beam focusing are inside the apparatus at a distance of 46 cm from the IP, and surrounding the beam pipe. The quadrupoles are equipped with two lead/scintillating-tile calorimeters, QCAL, of $\sim 5X^0$ thickness, with the purpose of detecting photons that would be otherwise absorbed on the quadrupoles.

2.2.4 Trigger

Event rates at DAΦNE are high; at the maximum luminosity of 10^{32} cm^{-2}s^{-1} up to 300ϕ s^{-1} and 30,000 Bhabha events/s are produced within the KLOE acceptance window. The trigger design has been optimized to retain all ϕ decays. Moreover, all Bhabha and $\gamma\gamma$ events produced at large polar angles are accepted for detector monitoring and calibration, as well as a downscaled fraction of cosmic-ray particles, which cross the detector at a rate of $\sim$ 3000 Hz. Finally, the trigger provides efficient rejection on the two main sources of background: small angle Bhabha events, and particle lost from the DAΦNE beams, resulting in very high photon and electron fluxes in the interaction region.

The trigger electronic logic system rapidly recognizes topologies and energy releases of interest, processing the signals coming both from EMC and DC. Since ϕ decay events have a relatively high multiplicity, they can be efficiently selected by the EMC trigger by requiring two isolated energy deposits (trigger sectors) in the calorimeter above a threshold of 50 MeV in the barrel and 150 MeV in the endcaps. Events with only two fired sectors in the same endcap are rejected, because this topology is dominated by machine background. Moreover, events with charged particles in the final state give a larger number of hit wires in the DC than do background events. The DC trigger employs this information, requiring the presence of $\sim$15 hits in the DC within a time window of 250 ns from beam crossing. An event satisfying at least one of the two above conditions generates a first level trigger, T1, which is produced with minimal delay and is synchronized with the DAΦNE master clock. The T1 signal initiates conversion in the front-end electronics modules, which are subsequently read out following a fixed time interval of $\sim 2\mu$s, which is ultimately driven by the typical drift distances travelled by electrons in the DC cells. In case of DC trigger, a validation of the first level decision is required by asking for $\sim$120 hits within a 1.2-μs time window.

The KLOE trigger also implements logic to flag cosmic-ray events, which are recognized by the presence of two energy deposits above 30 MeV in the outermost calorimeter layers. For most data taking, such events were rejected after partial reconstruction by an online software filter.

2.2.5 Data acquisition and processing

At a luminosity of $\sim$100 $\mu b^{-1}/s$, the trigger rate is $\sim$2000 Hz. Of these $\sim$500 Hz are from ϕ decays or Bhabha scattering. All digitized signals from the calorimeter, drift chamber, calibration and monitoring systems are fed via fiber optics from the electronics, sitting on platforms mounted on the KLOE iron yoke, to the computers in the next building. The Data Acquisition architecture has been designed to sustain a throughput of 50 Mbytes/s all along this path. In the near-by control room one can see real time displays of reconstructed charged tracks traversing the DC and photons depositing energy clusters in the EMC. The display of two events is shown in Fig. 2.8.

The events are reconstructed, meaning that charged tracks and energy deposits that occurred at the same instant in time on the various subcomponents of KLOE are associated together, properly labelled and packed into a unique file. To optimize the event reconstruction the constants for the time and energy scales are continuously recalibrated. Furthermore, background hits are acquired using a random trigger, which are recorded in order to be used in the simulation of KLOE events (MC). The MC simulation program reproduces accurately the detector geometry, the response of the apparatus and the trigger requirements, but of course cannot foretell the moment to moment variation of the background.

All raw data, background, reconstructed and MC events are recorded on tape. At reconstruction time, events are classified into broad categories, or "streams". Data summary tapes are produced with a separate procedure.

The KLOE analysis includes making data summary tapes and extensive modeling of the detector response. This requires generation of large number of Monte Carlo (MC) events for each process under study.

2.2.6 Monte Carlo simulation

KLOE has to has to be kept under continuous control, both to guarantee efficient data taking, and for safety reasons. Parameters such as high and low voltage settings, the temperature of the electronics components, or the status of the drift chamber gas system are set and monitored by a dedicated system fully embedded in the Data Acquisition process: the Slow Control. This system also records some machine parameters, and provides to

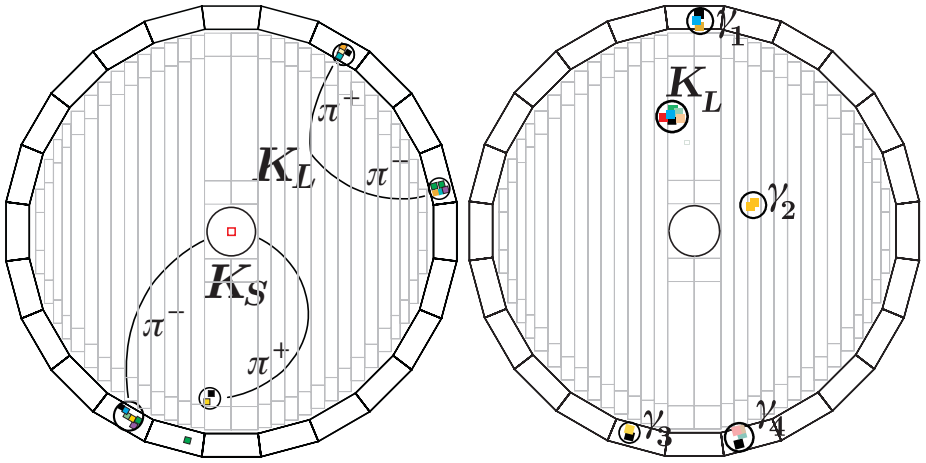

Figure 2.8: $K^0_S K^0_L$ events in KLOE. Left: both K^0_L and K^0_S decay to charged pions $\pi^+\pi^-$. Color patches indicate energy in the calorimeter. Right: 5 neutral particles. γ_1 trough γ_4 are showers from 4 photons from $K^0_S \to \pi^0\pi^0 \to 4\gamma$. The K^0_L reaches the calorimeter before decaying. It literally crashes in the EMC, producing a huge energy release.

the DAΦNE team information about KLOE including the on line measurements of the luminosity and of the background levels.

2.3 Reconstruction performance

KLOE provides a continuous monitoring of the machine working point, providing feedback to DAΦNE continuously as well. The most important parameters are the beam energies and crossing angle, which are obtained from the analysis of Bhabha scattering events with $e^\pm$ polar angles above 45 degrees.

The average value of the center-of-mass (CM) energy is evaluated online during data taking with a precision of $\sim$ 50 keV for each 200 nb^{-1} of integrated luminosity. This determination is further refined with offline analysis to achieve a precision of $\sim$ 20 keV, as discussed later.

The position of the e^+e^- primary vertex, with coordinates X_{PV}, Y_{PV}, and Z_{PV}, is reconstructed run-by-run from the same sample of Bhabha events. X_{PV} and Y_{PV} are determined with typical accuracy of about 10 μm, and have widths $L(X)$ and $L(Y)$ which are about 1 mm and few tens of μm, respectively. Z_{PV} is also reconstructed online with $100-200$ μm

	EMC parametrization		DC parametrization
σ_E/E	$5.7\%/\sqrt{E(GeV)}$	$\sigma_p/p(\theta > 45^0)$	~ 0.4 %
$\sigma(M)$ (MeV)	15 (π^0), 40 (η,K)	$\sigma(M)$ (MeV)	1 (η,K)
$\sigma_{x,y}$ (cm)	$\sim$1.3	$\sigma_{x,y}$ (μm)	150
σ_z (cm)	$1.2\ /\sqrt{E(GeV)}$	σ_z (mm)	2
σ_t (ps)	$57\ /\sqrt{E(GeV)} + 140$	$< \frac{dE}{dx} > \frac{counts}{cm}$	$\sim$120 ($K^{\pm}$), $\sim$15 (μ, π from $K^{\pm}_{\mu 2,\pi 2}$)
σ_{R_v} (cm)	2-3	$\sigma_{Xv,Yv}$ (mm)	$\sim$2 (@IP), $\sim$3 (@L $\sim$1m)

Table 2.1: Summary table of the EMC and DC performances.

accuracy, but it has a natural width of $12-14$ mm, determined by the bunch length itself.

2.3.1 Overview of DC and EMC performance

KLOE is a general purpose apparatus with good performances of the two main detectors, the DC and the EMC, its real strength manifests when joining the reconstruction capability of both detectors.

The table 2.1 summarizes the parametrized resolution for neutral particles (mainly photons) and for charged tracks (mainly electrons/pions). The resolution on invariant masses are also reported in the same table as well as the reconstruction capability for neutral and charged vertices.

In KLOE, the single particle reconstruction efficiency can be determined from data control samples, as well as from Monte Carlo simulation. As an example, the photon reconstruction efficiency as a function of the photon energy can be estimated from $\phi \to \pi^+\pi^-\pi^0$ events, where a redundant determination of the decay photon kinematics is possible using the charged pion momenta as measured from the DC. For charged particles produced at the interaction point, the track efficiency can be measured from $K^0_S \to \pi^+\pi^-$ events selected with the requirement of having at least one track fulfilling the two-body decay kinematics. A high reconstruction efficiency is observed for both detectors on data and Monte Carlo. For each specific analysis, the event selection efficiency is evaluated from Monte Carlo. To take into account data-MC difference in the cluster/track efficiencies, the calculation is usually performed by weighting each particle in the final state with the

ratio of data/MC reconstruction efficiencies.

The particle identification, PID, is started extrapolating tracks on the calorimeter surface and associating tracks to clusters. The identification of photons is based on clusters not associated to any track and on the difference between expected and reconstructed time of flight, ToF, for straight trajectories. The PID of charged tracks, which at the considered energy are electrons, pions and muons, is based on a combined usage of EMC and DC, by looking at ToF, E/p and cluster shape. At low momenta, $p < 200$ MeV, the ToF is usually the winning handle while at higher momenta variables based on cluster shape are used. Often these information are combined together in a likelihood identification variable or using a neural network identify charged kaons used instead dE/dx, given the excellent separation provided by the specific ionization measurement between kaons and the other charged particles produced in the apparatus.

2.3.2 Absolute energy scale

An improved determination of the CM energy, W, is obtained for each run by fitting the e^+e^- invariant-mass distribution for Bhabha events to a Monte Carlo (MC) generated function, which includes radiative effects. Initial state radiation (ISR), where one or both initial colliding particles radiate a photon before interacting, affects the e^+e^- CM energy and therefore the final state invariant mass. The ISR is mostly collinear to the beam, and in general is not detected. MC Bhabha events were generated using the `Babayaga` event generator, which accounts for both final and initial state radiation.

The absolute energy scale is calibrated by measuring the visible cross section for the $\phi \to K_S^0 K_L^0$ process. The cross section peak is fitted to a theoretical function, which depends on the ϕ parameters, takes into account the effect of ISR, and includes the interference with the $\rho(770)$ and the $\omega(782)$ mesons. The ϕ mass, total width, and peak cross section are the only free parameters of the fit, the $\rho(770)$ and the $\omega(782)$ parameters being fixed. The results of the fit to the data are shown in Fig. 2.9. The ϕ mass value obtained from the fit is $m_\phi = 1019.329 \pm 0.011$ MeV, which has to be compared with $m_\phi = 1019.483 \pm 0.011 \pm 0.025$ MeV, measured by CMD-2 at VEPP-2M. For CMD-2 the absolute energy scale is accurately determined from beam induced resonant depolarization: the ratio $m_\phi^{CMD}/m_\phi^{KLOE} = 1.00015$ is used to correct the determination of the center of mass

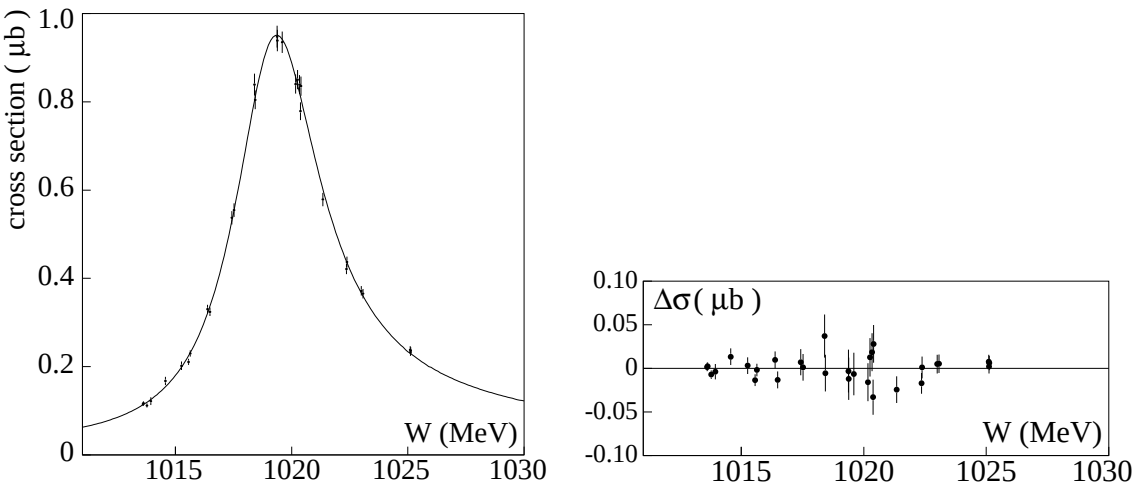

Figure 2.9: Left: Cross section for $e^+e^- \to \phi \to K_S K_L$ as a function of the CM energy (line:fit). Right: Fit residuals.

energy. This corresponds to a shift in the value of W of ∼150 keV.

2.3.3 Luminosity

The tagging capability of the calorimeter trigger allowed to perform fast luminosity measurements, providing a robust estimate of the DAΦNE luminosity with few per cent accuracy. This was achieved by counting Bhabha events in the acceptance of the calorimeter barrel selecting the events with two trigger sectors fired on the barrel, imposing a higher discrimination threshold than the one used in the standard acquisition chain. The tight angular selection, which reduces the available statistics by a factor of $\sim$ 6, was motivated by the need to keep under control the overwhelming machine background, which is concentrated at small angle.

Additional cuts on the position of the fired sectors and on the time difference between the two signals were added to improve rejection on the residual background, from cosmic-ray events. When operating at $\mathcal{L}$=100 μb^{-1}/s, the luminosity measurement was updated every 15 s, with a statistical error of $\sim$ 3%. Fig. 2.10 top shows the monthly integrated luminosity by KLOE since January 2001, while in the bottom the year integrated luminosity is shown. These data have been collected almost exclusively at the ϕ peak. In early 2006, KLOE also collected ∼200 pb^{-1} of data at $\sqrt{s}$ = 1000 MeV, at which $\sigma(e^+e^- \to \phi \to \pi^+\pi^-\pi^0)$ drops to 5% of its peak value.

A more accurate measurement of the integrated luminosity is performed offline, using Bhabha events in the polar angle range $55^\circ < \theta < 125^\circ$, the so-called VLAB events. The effective cross section for these events, $\sim$ 430 nb, is large enough to reduce the statistical error at a negligible level. The luminosity is obtained by counting the number of VLAB candidates, $N_{\rm VLAB}$, and normalizing it to the effective Bhabha cross section, $\sigma^{\rm MC}_{\rm VLAB}$, obtained from MC simulation, after subtraction of the background, $\delta_{\rm bkg}$:

$$\int \mathcal{L}dt = \frac{N_{\rm VLAB}}{\sigma^{\rm MC}_{\rm VLAB}}(1-\delta_{\rm bkg}). \tag{2.1}$$

The precision of the measurement depends on the correct inclusion of higher-order terms in computing the Bhabha cross section using `Babayaga`, which include the QED radiative corrections in the framework of the parton-shower method. The quoted precision is 0.5%, although an updated version of this generator, `Babayaga@NLO`, has been released recently. The new predicted cross section decreased by 0.7% and the theoretical systematic uncertainty improved from 0.5% to 0.1%.

The VLAB events are selected with requirements on variables that are well reproduced by the KLOE MC. The acceptance cut on the electron and positron polar angle, $55^\circ < \theta_{+,-} < 125^\circ$ is based on the calorimeter clusters, while the momentum selection, $p_{+,-} > 400$ MeV, is based on the DC determination. The background from $\mu^+\mu^-(\gamma)$, $\pi^+\pi^-(\gamma)$, and $\pi^+\pi^-\pi^0$ events is well below 1% and is subtracted. All selection efficiencies (trigger, cluster and track reconstruction) are greater than 99%, as obtained from MC and confirmed with data control samples. Finally, corrections are applied on a run-by-run basis to follow the small variations in the CM energy and in the detector calibration. The uncertainty in the determination of the acceptance due to experimental effects is 0.3% .

2.4 K^0_S beams

Each neutral kaon pair from $\phi \to K^0\overline{K}^0$ is in a pure $J^{PC} = 1^{--}$ state. Therefore the initial two-kaon state can be written, in the ϕ-rest frame, as

$$\begin{aligned} |\, K\overline{K}, t=0\,\rangle &= \left(|\, K^0, \mathbf{p}\,\rangle |\, \overline{K}^0, -\mathbf{p}\,\rangle - |\, \overline{K}^0, \mathbf{p}\,\rangle |\, K^0, -\mathbf{p}\,\rangle\right)/\sqrt{2} \\ &= \left(|\, K^0_S, \mathbf{p}\,\rangle |\, K^0_L, -\mathbf{p}\,\rangle - |\, K^0_L, \mathbf{p}\,\rangle |\, K^0_S, -\mathbf{p}\,\rangle\right)/\sqrt{2}, \end{aligned} \tag{2.2}$$

where the identity holds even without assuming CPT invariance. Detection of a K^0_S thus signals the presence of, "tags", a K^0_L and vice versa. DAΦNE give pure K^0_S and K^0_L beams

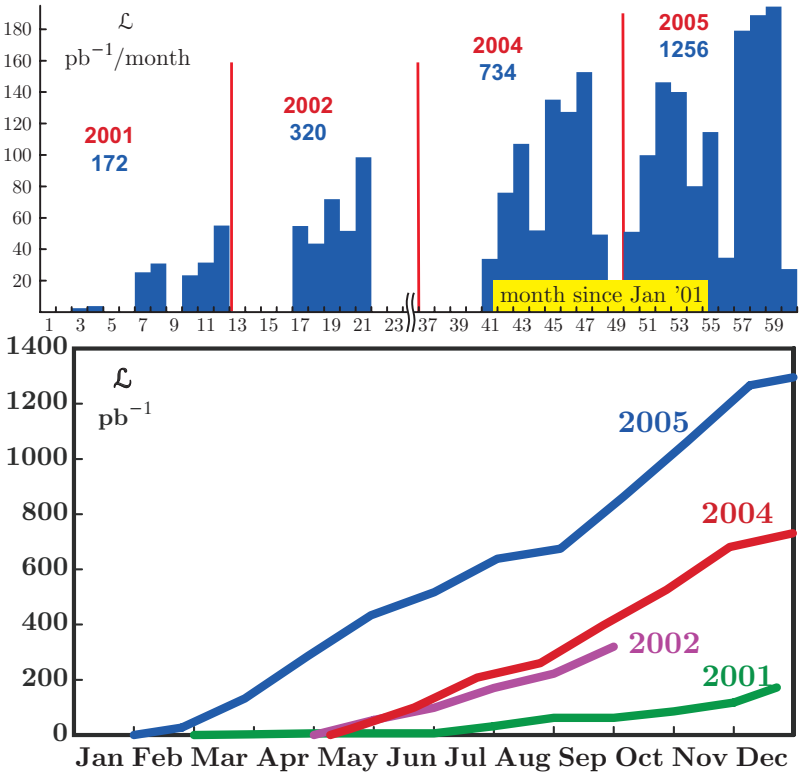

Figure 2.10: Integrated luminosity since January 2001: by month (top) and by year (bottom).

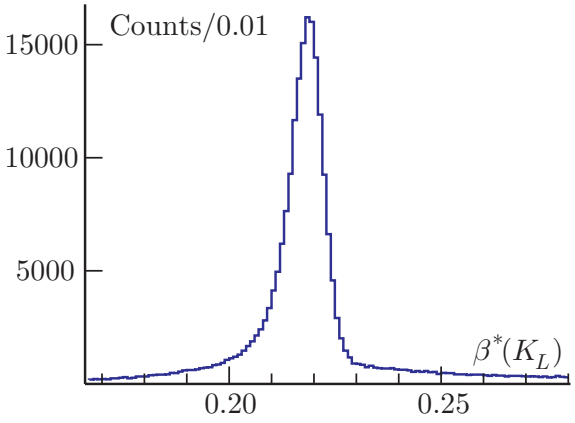

Figure 2.11: K_L^0 velocity in ϕ-frame from time of flight.

of precisely known momenta (event by event) and flux beams.

Because of the exceptional timing capabilities of the EMC and the slowness of the kaons from ϕ-decays, a ToF technique can be used to tag K^0_S in a unique way. As already mentioned, neutral kaons have a velocity $\beta = 0.2162$ in the ϕ frame and β=0.193 to 0.239 in the lab, and 60% of them reach the calorimeter in a time $\geq$31 ns. K^0_L interact in the calorimeter with an energy release up to their mass, 497 MeV. For an energy release of 100 MeV the time resolution is $\sim$0.3 ns, i.e. about a $\sim$1% accuracy on K^0_L velocity, shown in Fig. 2.11.

In KLOEa K^0_L interaction in the EMC is called a "K-crash", and it is used it as a tag for the K^0_S. Note that the above error on $\beta(\ K^0_L)$ corresponds to an error on the kaon energy of $\sim$0.25 MeV or $\sim$1 MeV for its momentum, with just one event. Adding the information about the position of the energy release, the direction of the K^0_L line of flight is determined with $\sim 1^\circ$ angular accuracy. Using the previous value of K^0_L momentum, and the average value of the ϕ momentum evaluated from Bhabha events, it is possible to know the K^0_S momentum from $p_S = p_\phi - p_L$, with the same accuracy as for K^0_L.

2.5 K^0_S physical parameters and decays

Since the kaons discovery, knowledge of its properties, e.g. masses, lifetimes, and branching ratios (BR), has been accumulated over hundreds of individual experiments, performed at various laboratories all over the world. Each experiment has its own peculiarity, contingent upon the particle beam available and its own equipments acceptance range, which can result in highly accurate measurements from a statistical point of view (namely based on thousands of data events) but with hidden corrections peculiar to it. The particle data group in charge of compiling the results, can only average the various results according to their nominal errors and apply a scale factor to these errors when faced with two inconsistent measurements. The validity of this procedure is sometimes dubious: having a consistent set of results would make the results more reliable.

The mission of KLOE is to measure most of the properties of the kaon system to high accuracy, with a single detector simultaneously. One problem that consistently plagues the interpretation of older measurements is the lack of clarity about accounting for radiative contributions. All the measurements of kaon decays with charged particles in the final state

are fully inclusive of radiation. Radiation is automatically accounted for in the acceptance correction. The MC generators incorporate radiation as described in [Gatti06]. Because of the availability of tagged and pure kaon beams of known momenta, KLOE is the only experiment that can at once measure the complete set of experimental inputs, branching ratios, lifetimes and form factor parameters for both charged kaons and long lived neutral kaons. In addition KLOE is the only experiment that can measure K^0_S branching ratios at the sub-percent level.

2.5.1 K^0 mass

Kaon masses are about 500 MeV, very close to one half the ϕ mass, known to an accuracy of $\sim 2\times 10^{-5}$, by the use of the g-2 depolarizing resonances, [PDG06]. The events $\phi \to K^0_S K^0_L$ offer a unique possibility to obtain a precise value of the neutral kaon mass. If the ϕ is at rest the kaon mass can be extracted from the kaon momentum using the relation:

$$m_K = \sqrt{\frac{m_\phi^2}{4} - p_K^2}; \qquad \frac{\Delta m_K}{m_K} \simeq \frac{p_K^2}{m_K^2}\frac{\Delta p_K}{p_K} \sim \beta^2 \frac{\Delta p_K}{p_K}\,. \tag{2.3}$$

Since $p_K \simeq 110$ MeV, measuring it at 1% level, well within the KLOE capability, results in a measurement of the K^0 mass better than 0.1%. 50,000 events are enough to reach a statistical accuracy of about 1 keV.

ϕ mesons are produced with a momentum along the x axis, $p_\phi = 12.5$ MeV at DAΦNE. The measure of the K^0_S momentum is given from the measured momenta of the two pions $K^0_S \to \pi^+\pi^-$: the K^0_L momentum is obtained from $\vec{p}_{K^0_L} = \vec{p}_\phi - \vec{p}_{K^0_S}$, where $\vec{p}_\phi$ is the average ϕ momentum measured with Bhabha events collected in the same runs. The center of mass energy of the $K^0_S K^0_L$ pair (W_{KK}) is related to the kaon mass m_K, according to:

$$W_{KK}(m_K) = \sqrt{2M_K^2 + 2E_{K^0_S}E_{K^0_L} - 2\vec{p}_{K^0_S}\cdot\vec{p}_{K^0_L}}$$

with

$$E_{K^0_S} = \sqrt{p^2_{K^0_S} + m^2_K} \qquad E_{K^0_L} = \sqrt{p^2_{K^0_L} + m^2_K}.$$

On the other hand the collision center of mass energy W is computed from Bhabha events. Corrections due to ISR have to be taken into account when relating W to W_{KK}. The correction function $f_K(W)$ has been evaluated using a full detector simulation where the radiation from both beams has been implemented, and W_{KK} is reconstructed as

in the data. The expression of the radiator function has been taken from [KLOE95], including $\mathcal{O}(\alpha^{\in})$ corrections. The correction $|1-f_K(W)|$ is very small below the resonance, corresponding to a shift in W_{KK} of 40 keV. For W above the ϕ mass, W_{KK} increases up to 100 keV. The neutral kaon mass is then obtained solving the equation:

$$W = f_K(W) \times W_{KK}(m_K)\,. \tag{2.4}$$

The single event mass resolution is about 430 keV. Contributions to the mass resolution are: about 370 keV from experimental resolution, about 220 keV from beam energy spread, as measured by KLOE in agreement with machine theory, and about 100 keV from ISR. The systematic error due to the momentum miscalibration has been evaluated by changing the momentum scale in computing the pion momenta. A momentum miscalibration, $\delta p/p$, translates to a miscalibration on the mass $\delta m_K/m_K = 0.06\delta p/p$, in agreement with the above qualitative calculation. The momentum scale is obtained by using several processes covering a wide momentum range, from 50 to 500 MeV ($K^0_L \to \pi^+\pi^-\pi^0$, $K^0_L \to \pi\ell\nu$, $\phi \to \pi^+\pi^-\pi^0$). The fractional accuracy obtained (below 2×10^{-4}), is in agreement with that estimated using Bhabha events [KLOE04], which results in a systematic error δm_K of 6 keV.

The systematic error coming from theoretical uncertainty on the radiator function has been evaluated considering the contribution from higher order terms in α. The correction function $f_K(W)$ has been evaluated by excluding the constant term in the $\mathcal{O}(\alpha^{\in})$. The corresponding change in $f_K(W)$ is 1.3×10^{-5}, corresponding to a variation on m_K of 7 keV. Additional systematics come from the dependence of the measured mass from the value of W. They have been evaluated by comparing the mass values obtained with data collected at $W < 1020$ MeV and $W > 1021$ MeV, where the value of $f_K(W)$ is more than a factor two larger. The difference between the two mass values is $m_K(W < 1020) - m_K(W > 1021) = 9 \pm 10$ keV, consistent with zero.

Other sources of systematics are due to the uncertainties on the W calibration, i.e., the statistic and systematic error on m_ϕ^{CMD-2} and on m_ϕ obtained from the fit, discussed in sect. 2.3.2. The total contribution from these sources amounts to a mass uncertainty of 15 keV. Systematic uncertainties are treated as uncorrelated. The result is:

$$m_{K^0} = 497.583 \pm 0.005_{\rm stat} \pm 0.020_{\rm syst} \quad \text{MeV}. \tag{2.5}$$

Mode	BR(mode)/BR($\pi^+\pi^-$)	BR(mode)
$\pi^+\pi^-$	—	$(69.196 \pm 0.024 \pm 0.045)\%$
$\pi^0\pi^0$	$1/(2.2549 \pm 0.0054)$	$(30.687 \pm 0.024 \pm 0.045)\%$
$\pi^- e^+ \nu$	$(5.099 \pm 0.082 \pm 0.039) \times 10^{-4}$	$(3.528 \pm 0.057 \pm 0.027) \times 10^{-4}$
$\pi^+ e^- \bar{\nu}$	$(5.083 \pm 0.073 \pm 0.042) \times 10^{-4}$	$(3.517 \pm 0.050 \pm 0.029) \times 10^{-4}$
$\pi e \nu$	$(10.19 \pm 0.11 \pm 0.07) \times 10^{-4}$	$(7.046 \pm 0.076 \pm 0.051) \times 10^{-4}$

Table 2.2: KLOE measurements of K_S^0 branching ratios.

2.5.2 K_S^0 decays

KLOE has measured K_S^0 branching ratios, whose values span six orders of magnitude.

$K_S^0 \to \pi^+\pi^-(\gamma)$, $\pi^0\pi^0$

The K_S^0 decays mostly (99.9% of the times) into two pions: $\pi^0\pi^0$ and $\pi^+\pi^-$.
Given the tag, the $K_S^0 \to \pi^+\pi^-(\gamma)$ events are selected by requiring the presence of two tracks of opposite charge with their point of closest approach to the origin inside a small fiducial volume around the IP, and with momentum in the range $120 < p < 300$ MeV. $K_S^0 \to \pi^0\pi^0$ events are identified by the prompt photon clusters from π^0 decays. A calorimeter cluster is considered as a prompt photon if its velocity, evaluated by ToF, is compatible with $\beta = 1$ within the expected resolution. Moreover, it must not be associated to any track. To accept a $K_S^0 \to \pi^0\pi^0$ event, three or more prompt photons are required, with a minimum energy of 20 MeV, to reduce contamination from machine background.

$K_S^0 \to \pi e \nu(\gamma)$

The K_S^0 decays semileptonically less than one per cent of the time. To pick out such decays where the event contains an unseen neutrino is non-trivial. Yet, KLOE has isolated a very pure sample of ∼13,000 semileptonic K_S^0 decays and accurately measured the BRs for $K_S^0 \to \pi^+ e^- \bar{\nu}(\gamma)$ and $K_S^0 \to \pi^- e^+ \nu(\gamma)$ [KLOE06].

3

Symmetries in Einstein's relativity

3.1 Introduction

At the beginning of the XX century, Einstein formulated the theories of Special and General Relativity that constitute the foundation of the best existing description of nature at the fundamental level.

A very short review of the principles underlying Special Relativity (SR), their meaning, their consequences and some relations important for this experiment is given. Since one of the aims of this work is to look for possible anisotropies of the K_S^0 lifetime, some test theories and experiments testing the foundations are also illustrated.

3.2 The relativity principle as a symmetry

≪Rinserratevi con qualche amico nella maggiore stanza che sia sotto coverta di alcun gran naviglio, e quivi fate d'aver mosche, farfalle e simili animaletti volanti: siavi anco un gran vaso d'acqua, e dentrovi de' pescetti; sospendasi anco in alto qualche secchiello, che a goccia a goccia vada versando dell'acqua in un altro vaso di angusta bocca che sia posto a basso; e stando ferma la nave, osservate diligentemente come quelli animaletti volanti con pari velocità vanno verso tutte le parti della stanza. [..] Osservate che avrete diligentemente tutte queste cose, benché niun dubbio ci sia mentre il vascello sta fermo non debbano succedere cosi' fate muovere la nave con quanta si voglia velocità ché (pur di moto uniforme e non fluttuante in qua e in là) voi non riconoscerete una minima mutazione in tutti li nominati effetti; né da alcuno di quelli potrete comprendere se la nave cammina,

o pure sta ferma. ≫ [Gal1632] [1]

In this way in the Second Day of the "Dialogo sopra i due massimi sistemi del mondo" Galilei's fictional advocate Salviati thought an experiment asserting the experimental equivalence of two ships in uniform relative motion and Galilei gave the first modern formulation of the relativity principle.

Newton makes the important restriction of considering only uniform motion along straight lines, i.e., Inertial Reference Frames (IRF). Newton thought that there existed one absolute space and a multitude of inertial systems. Even if empirical observations cannot detect if a certain body is at absolute rest, Newton felt the need to introduce this concept anyway. Then first Poincaré formulated the fundamental law of physics that he referred to as the principle of relativity (PR): "The principle of relativity", according to which the laws of physical phenomena must be the same, whether for a fixed observer, as also for one dragged in a motion of uniform translation, so that we do not and cannot have any means to discern whether or not we are dragged in a such motion. Over the years the principle of relativity and the concept of absolute space have been transformed, extended and exploited to great effect by, among others, Poincaré, Leibniz, Huygens and Mach. A privileged reference frame was considered by several eminent scientists, such as Poincaré and Lorentz. But it has been Einstein who instituted a major change in the physics paradigm concerning the absolute space with his postulates.

[1] Lock yourself with some friend in the main cabin below decks on some large ship, and have with you there some flies, butterflies, and other small flying animals. Have a large bowl of water with some fish in it; hang up a bottle that empties drop by drop into a wide vessel beneath it. With the ship standing still, observe carefully how the little animals fly with equal speeds to all sides of the cabin. The fish swim indifferently in all directions; the drops fall into the vessel beneath; and in throwing anything to your friend, you need throw it no more strongly in one direction than another, the distances being equal; jumping with your feet together, you pass equal spaces in every direction. When you have observed all these things carefully (though there is no doubt that when the ship is standing still everything must happen this way), have the ship proceed with any speed you like, so long as the motion is uniform and not fluctuating this way and that. You will discover that not the least change in all the effects named, nor could you tell from any of them whether the ship was moving or standing still. Dialogue Concerning the Two Chief World Systems (1632)

3.3 Einstein's postulates and the Lorentz transformation

The traditional formulation of SR, leading to Lorentz transformations, is constructed in accordance with two postulates of Einstein.

Relativity principle:

In every inertial frame the laws of physics are the same.

I.e., there is no possibility to detect absolute motion and no preferred frame exists.

Invariance of the velocity of light:

The velocity of light in vacuum is constant and equal in all inertial frames.

From these two postulates Einstein deduced the Lorentz transformations. Let S denote the reference frame with origin O and with coordinates x, y, z, and time t. Let S' be another reference frame whose origin O' moves with *speed* v ($v > 0$), relative to S, in the direction of the positive x-axis of S, and let x', y', z' denote the coordinates in S', and t' the time in S'. Let suppose also that the origins O and O' of S and S' coincide at time $t = 0$ which is also the time $t' = 0$. The y'- and z'- axes of S' are assumed to remain parallel to the y- and z- axes of S, respectively. Then, the coordinates x, y, z, and time t in S of an event are related to the coordinates x', y', z', and time t' in S' of the same event by the following Lorentz transformation:

$$x' = \gamma(x - vt) \qquad y' = y \qquad z' = z \quad t' = \gamma(t - \frac{vx}{c^2}) \tag{3.1}$$

where c denotes the speed of light in S *and* S' and $\gamma = 1/\sqrt{(1-\beta^2)}$ with $\beta = v/c$. Note that $\gamma > 1$. The transformation (3.1) has an inverse, namely:

$$x = \gamma(x' + vt') \qquad y = y' \qquad z = z' \qquad t = \gamma(t' + \frac{vx'}{c^2}). \tag{3.2}$$

If the origin O' of S' were to move in the direction of the negative x- axis of S, with *speed* v ($v > 0$) then in (3.1) and (3.2), is necessary to replace v by $-v$.

The electric field vector $\vec{E}$ of a monochromatic plane wave with the frequency ν in I is given by

$$\vec{E}(\vec{x}) = \vec{E}_0 e^{i(\omega t - \vec{k}\vec{x})} \tag{3.3}$$

where ω=$2\pi\nu$ is the angular frequency of the wave, $\vec{k}$ is the wave number vector with an absolute value of ω/c . The phase $\phi = \omega t - \vec{k}\mathbf{x}$ is a Lorentz invariant and does not change when transformed from one frame to another frame

$$\phi = \omega t - \vec{k}\vec{x} = \omega' t' - \vec{k}'\vec{x}' = \omega t - kx\cos\theta = \omega' t' - k' x' \cos\theta' \,. \tag{3.4}$$

Being the time derivative of the phase, the observed frequency $\nu' = \omega'/(2\pi)$ in S' can be determined as $\nu' = 1/(2\pi) \cdot d\phi/dt'$. The result is the relativistic Doppler formula:

$$\nu' = \nu\gamma(1 - \frac{v}{c}\cos\theta) \tag{3.5}$$

where θ is the angle between the direction of the wave and the direction of motion of S' with respect to S, measured in S. If the wave is parallel ($\theta = 0$) or antiparallel ($\theta = \pi$) to the direction of motion and ν' should be equal for both cases, the frequency ν_p for $\theta = 0$ and ν_a for $\theta = \pi$ is given by

$$\nu' = \nu_p\gamma(1 - \frac{v}{c}) \tag{3.6}$$

$$\nu' = \nu_a\gamma(1 + \frac{v}{c}) \,. \tag{3.7}$$

The fundamental hypothesis of SR is what Einstein defined as the principle of relativity [Einst1905], is in more modern terms called Local Lorentz Invariance (LLI) [Will93]. The LLI postulates roughly state that the outcome of any local test experiment is independent of the velocity of the apparatus. LLI can be viewed as a constituent part of the Einstein Equivalence Principle which is fundamental to General Relativity (GR) and all metric theories of gravitation [Will93]. A physical system is said to have "Lorentz symmetry" if the relevant laws of physics are unaffected by Lorentz transformations (rotations and boosts). Lorentz symmetry underlies the theory of relativity and all accepted theoretical descriptions of nature at the fundamental level. A decisive role in establishing both the rotation and boost components of Lorentz symmetry has been played by experimental studies of the properties of light. The foundation of SR rests on the postulate that the speed of light does not depend on the relative velocity of the source and observer, the direction of the light beam, or its wavelength. Much of modern physics is based on the concept of symmetry and invariance, describing how all measured quantities are seen by different observers in relative motion.

3.4 Testing SR

According to Kuhn [Kuhn70] "A paradigm is what members of a scientific community, and they alone, share". It includes models and theories, concepts, knowledge, assumptions, and values that scientists accept and work with. Of course all paradigms are affected by anomalies and encounter the crises that are "a necessary precondition for the emergence of novel theories and ask next how scientists respond to their existence". A crisis occurs when the scientific community is ready to try new ideas, maybe also previously discarded and abandon a previously used paradigm to choose a new paradigm to work with.

At the end of XIX century the Newton's Universe where length and time were the same everywhere, was in trouble because of the need for absolute space and time events or interactions to be referred to reference frames. The (then) newly formulated theory of electromagnetic waves seemed to involve a medium for light propagation.

Before Einstein's formulation of relativity was ongoing a crisis in the concepts of light propagation, absolute space, reality of ether and relative motion. In fact the controversy about the existence of a preferred reference frame dates back to the birth of the Theory of Relativity i.e. to the basic differences between Einstein's SR and the Lorentz-Poincaré point of view. Looking for a new theory of electromagnetism, Poincaré tried to preserve as much as he could of the old. He was fond of ether and continued to believe in it, even when his own theory showed that it was unobservable. In his version of relativity the new idea of local time, depending on the motion of the observer, was worked out in the conventional framework of absolute space and time defined by a rigid, immovable ether. Einstein, on the other hand, considered the conventional framework as cumbersome and unnecessary and was delighted to get rid of it [Dyson03]. Today the Einstein's interpretation is generally accepted. However, in spite of the deep conceptual differences, it is not so obvious how to experimentally distinguish between the two interpretations since the basic quantitative ingredients, i.e. the Lorentz transformations, are the same in both formulations.

Indeed, SR arose at the beginning of the XX century as a response to the conflict between the electromagnetism and nonrelativistic mechanics. At about the same time, quantum mechanics was introduced as a response to the mismatch between electromagnetic radiation equilibrium (blackbody radiation) and classical statistical mechanics (which is based on non-relativistic mechanics).

Einstein's SR has triggered straight from its birth, which occurred nearly a century ago, an unprecedented debate. For some, it represents a fundamental unification in physics, the need of which had been felt since Faraday's and Maxwell's, which in the XIX century created a contradiction with Newtonian mechanics. For others, SR appears to be an example of a theory constructed expressly to explain a puzzling experimental finding and the second postulate to be suggested by the Michelson-Morley experiment (Brush 1999, Norton 2004) [Sar96] even if Einstein in his paper did not refer to the Michelson-Morley experiment and apparently was not motivated by it.

Also today some technical critiques are raised against Einstein's work[2]. According to such minority views the traditional null interpretation of the ether-drift experiments should be challenged whereas the alternative view with a preferred frame would be entirely consistent, and perhaps in better agreement, with the results of the classical experiments.

However some experimental evidence for an energetic ether seems to be emerging. If a non-zero vacuum energy exists, the physical vacuum of present particle physics might represent a preferred reference frame. In the physical universe there is one clearly preferred reference frame: the Cosmic Microwave Background (CMB). The presence of CMB is the proof that matter in motion exists everywhere in outer space. The CMB is a unique rest frame: with respect to that the solar system is moving at a velocity of (369 ± 2) km/s [PDG08]. Even if this is not proving any breaking of Lorentz symmetry, the existence of this natural rest frame revitalizes the field of experimental relativity because it provides a rational framework for the interpretation of any asymmetry that may be discovered. As far as currently known the Universe is isotropic: a separate, and open, question is whether there is any preferred direction in space. Copernicus's idea that nothing distinguishes the position of Earth's from any other place in the Universe is now questioned.

A testable determination of any dependence of the speed of light on motion or direction would contradict the notion of isotropy of space and would lead to the first (needed) modification of SR. It would have profound implications for the development of cosmology, high energy astrophysics, particle astrophysics, and basic physics, including particle

[2]See e.g. the dissident journals Galilean Electrodynamics, Physics Essays, Apeiron, Journal of New Energy, Infinite Energy or the books by dissident authors Harold Aspden, Stoyan Stag, Petr Beckmann, Peter and Neal Graneau, Ronald Hatch, Herbert Ives, Thomas Phipps, Jr., Franco Selleri, Maurice Allais, Vasco Guerra, Rodrigo Abreu and Reginald Cahill.

physics and relativity.

While the impact of a positive result would be impressive, even a non-detection would be highly significant. A refined upper limit would give new orientation to theoreticians would reduce the parameter space available to attempts to unify quantum mechanics, particle physics and gravity.

Nevertheless in more than one hundred years since Einstein's first paper [Einst1905] SR has passed many stringent tests. In the majority view this clearly demonstrates that, that for all practical purposes, in the Universe there is no preferred reference frame. The tests have provided a solid basis to any present fundamental theory of physics. As a consequence SR is today underpinning all of present day physics.

It is however very difficult to believe that Einstein's ideas are final, immutable forms of knowledge. Even Einstein in March 1949, answering his friend Maurice Solovine who had sent him a letter for his seventieth birthday, wrote: "You imagine that I look backwards on the work of my life with calm satisfaction. But from nearby it looks very different. There is not a single concept of which I am convinced that it will resist firmly". [SolEin87] Einstein did not hide the probable transitory nature of his creations. On April 4, 1955, he wrote the last paper of his life. It was a three page long preface (in German) to a book celebrating the fiftieth anniversary of the theory of relativity it ended with the following words: "The last, quick remarks must only demonstrate how far in my opinion we still are from possessing a conceptual basis of physics, on which we can somehow rely". [Sel04]

That fact continues to push experimentalists to search for new experiments, or improve on previous ones, in order to uncover a possible violation of SR, as that would most certainly lead the way to a new conception of physics and of the Universe. Additional incentives for such tests come from unification theories (e.g. quantum gravity), some of which [KosSam89, Dam97, GaPu05] suggest a violation of SR at some, a priori unknown, level.

How to perform a test of SR? There are essentially two possibilities: testing the postulates, and testing the consequences.

It would be useful to have test theories (i.e., theories which depend on parameters whose value describe the violation) in order to have a guideline at hand how to make a complete test of SR, and to relate the first and the second possibility above. A couple of test theories

are described in the next subsection.

3.4.1 Test theories

Robertson and Robertson-Mansouri-Sexl

Robertson [Robn49] invented a test theory which singled out three tests which - given particular results - will prove the validity of SR. These three tests are

1. tests of the isotropy of the velocity of light: in an arbitrarily moving frame the velocity of light is independent of the direction of propagation;[3]

2. test of the independence of the velocity of light from the velocity of the source or of the laboratory;

[3]The possibility of reliable experimental tests of the one-way speed of light went through all along the history of SR, because of the inescapable entanglement between remote synchronization and one-way velocity of light. In [Einst1905] Einstein defines the synchronization of two clocks at two places A and B: *We have not defined a common "time" for A and B, for the latter cannot be defined at all unless we establish* by definition *that the "time" required by light to travel from A to B equals the "time" it requires to travel from B to A. Let a ray of light start at the "A time"* t_{A} *from A towards B, let it at the "B time"* t_{B} *be reflected at B in the direction of A, and arrive again at A at the "A time"* t'_{A}*. In accordance with definition the two clocks synchronize if* $t_{\mathrm{B}} - t_{\mathrm{A}} = t'_{\mathrm{A}} - t_{\mathrm{B}}$.;

A particular analysis (see f.i. [AVS98], [Sel04, Sel03, Sel98, Sel99]) seems to unveil that no actual experiment, among the ones mentioned by the authors quoted before, is a genuine "one-way" measurement of the speed of light. As a consequence, it seems reasonable to suspect that the parameters appearing in the test-theories could actually be beyond the reach of experimental knowledge: in other words, these parameters could be "conventional" in the sense that their numerical values have no effect on the output of any actual experiment.

Likewise, it seems reasonable to suspect that some claims mentioned before could arise from circular arguments, in the sense that the conclusions could be hidden, from the very beginning, in the hypotheses.

In 1977, an anisotropy in the cosmic microwave background CMB due to the motion of the Solar System was discovered [SmGoMu77, Smoot07]. The result of this observation was interpreted as a possible "new ether drift", a manifestation of the Doppler effect because of the absolute motion of the Solar System at a velocity known today as $u_S = (369 \pm 2)$ km/s with respect to a preferred cosmological reference frame toward the Leo constellation. It seemed possible that the preferred reference frame [MaSe77a] found its place in physics as the reference frame in which relic radiation is isotropic. Glashow discussed the profound physics consequences of the presence of such a reference frame and the third the well known time-dilation effect, then SR has been tested to be valid - at least within the experimental accuracy.

3. test of the time dilation (or of the Doppler effect).

The first tests are called Michelson-Morley tests (Michelson and Morley 1887), the second Kennedy-Thorndike tests (Kennedy and Thorndike 1932) and the last Ives-Stilwell tests (Ives and Stilwell 1938), according to the persons who carried them through for the first time.

Until the 1940s the constancy of the velocity (1. and 2. above) of light was tested with interferometers. Modern tests use optical resonators and lasers. Tests of the Doppler effect use spectroscopic techniques applied to fast atoms or ions.

An extension of the Robertson test theory is due to Mansouri and Sexl [MaSe77a,MaSe77b, MaSe77c], and it is generally known as Robertson-Mansouri-Sexl.

The Standard Model Extension

Relatively recently, Alan Kostelecky and co-workers [ColKos97, ColKos98], motivated initially by possible Lorentz violating phenomenological effects of string theory [KosSam89], have developed a new model called the general Lorentz violating Standard Model Extension (SME) [Wolf06]. The SME is a dynamical test theory. The SME is a parametrized version of the standard model Lagrangian that involves all Lorentz violating terms that can be formed from known fields, including gravity [Kosto04]. It includes the Standard Model coupled to GR along with all possible operators for Lorentz violation. Both global and local Lorentz violation are incorporated. Since CPT violation in realistic field theories is accompanied by Lorentz violation [Green02], parametrized the SME also describes general CPT violation. The fundamental theory of the SME as applied to electrodynamics, summarized below, is detailed in [KosMe02]. Its application to atomic physics, and in particular atomic clock experiments, is laid out in [KoLa99, Bluhm03] and summarized below. Usually, the SME describes a potential Lorentz violation using a number of parameters that are all zero in standard (non Lorentz violating) physics. These parameters depend on the frame and consequently vary as a function of the coordinate system chosen to analyze a given experiment. In principle they may be constant and non-zero in any frame (e.g. the lab frame). However, any non-zero values are expected to arise from Planck-scale effects in the early Universe. Therefore they should be constant in a cosmological frame (e.g. the one defined by the CMB radiation) or any frame that moves with

a constant velocity and shows no rotation with respect to the cosmological one. Consequently the conventionally chosen frame to analyze and compare experiments in the SME is a sun-centered, non-rotating frame as defined in [KosMe02]. The general procedure is to calculate the SME perturbation of the experimental observable in the lab frame (or cavity frame, or atom frame) and then to transform the lab frame SME parameters to the conventional sun-centered frame. This transformation will introduce a time variation of the frequency related to the movement of the lab with respect to the sun-centered frame (typically introducing time variations of sidereal and semi-sidereal periods for an Earth fixed experiment).

Selleri's approach

In recent years, Franco Selleri [RiRuSe04, Sel04, Sel99, Sel98, Sel96, Sel03] has refused to support at both the conventionalist approach and the SR, sustaining the cause of realism in a Lorentz-like background; yet he assumes the statement that "the constancy of the one-way speed of light is a mere convention without any empirical cornerstone"[4]. For a part of a scientific community Selleri approach is not formal but physical, conceptual, and even philosophical; such an approach gave rise to a discussion about the foundations of SR [Sel04, Sel99, Sel98, Bergia00, BerGui98, BeVa98].

Selleri has subjected to a critical analysis the two principles of SR (relativity principle and invariance of the velocity of light), emphasizing some aspects which, after a century from their first enunciation (1905), seem to be still somehow 'blurred': both concerning their formulation in precise operational terms and concerning their connection to precise empirical data. Selleri stressed that the existence of cosmic background radiation (or, in his other articles, the existence of light that reaches us from all directions by the various stars) can define a reference system that no one can ignore. Selleri bases his model of theoretical physics upon three "experimental evidences", on which the whole scientific community is in full agreement. They are, as Selleri himself stresses, hypotheses directly supported by the experimental data and, thus, wholly independent on any theoretical license. At variance with the two principles of SR that, being so loaded with theory, were formulated, in the celebrated 1905 paper, without any reference to experimental data.[5]

[4] Translation by [RiRuSe04].

[5] Einstein's aim was basically to recover the "unity of physics" which, at the beginning of the XX

Selleri shows that there exist not only a theory, but a whole set of theories in agreement with the "hard experimental evidences", which can be distinguished between each other by the value of a parameter e_1 (called "synchronization parameter"), which is *a priori* unconstrained. However, Selleri was not satisfied with this result, which apparently supports an unwanted operational viewpoint; in fact, this is only the first part of Selleri's approach. The second part, is the attempt to prove that a secret "nature's synchrony choice", although totally hidden in the class of IRF, actually exists, and can be unveiled by means of suitable experiments performed in non-IRF.
Selleri's approach can be briefly summarized by the following statements:

(i) in the ensemble of the theories consistent with the "hard experimental evidences", the synchronization parameter e_1 cannot be fixed by any experiment performed in a IRF;

(ii) the SR belongs to this ensemble and it corresponds to a definite value of the parameter e_1, namely $e_1 = -\beta\gamma/c$;

(iii) all the theories in which $e_1 \neq -\beta\gamma/c$ are inconsistent with SR;

(iv) even though statement (i) entails that the synchronization parameter cannot be fixed by any experiment performed in unaccelerated reference frames, such a parameter can be fixed by suitable experiments performed in accelerated, in particular rotating, reference frames. Selleri [Sel98] actually, considering some of such experiments (primarily the Sagnac effect), finds that nature forces the synchrony choice $e_1 = 0$, which is different from the relativistic one $e_1 = -\beta\gamma/c$.

That being stated, Selleri [Sel98] obtains the general coordinate transformations *from the optically isotropic IRF S_0 to a generic IRF S*, in motion with respect to S_0 with a dimensionless velocity $\beta \equiv \mathbf{v}/c$, which are in agreement with (i), (ii), (iii). If the x, y, z directions of the two frames are parallel, and the velocity β is along the x direction, the

century, seemed to have been lost because of the existence of two distinct invariance groups: one pertaining to Newton's mechanics and the other one valid for Maxwell-Lorentz's electromagnetism. Einstein aimed a rebuilding of the theoretical physics so that all its branches share the same invariance group.

coordinate transformations are:

$$\begin{cases} t &= \gamma^{-1}t_0 + e_1(x_0 - \beta c t_0) \\ x &= \gamma(x_0 - \beta c t_0) \\ y &= y_0 \\ z &= z_0 \end{cases} , \tag{3.8}$$

where $\gamma \equiv 1/\sqrt{1-\beta^2}$ and e_1 is an arbitrary function of β, whose dimension is $[velocity]^{-1}$. As a consequence, the general coordinate transformations consistent with the experimental evidences, in the kinematical conditions outlined above, turn out to be a family of transformations ("Selleri synchronization gauge") parameterized by the function $e_1(\beta)$. *Every $e_1(\beta)$ is admissible, and each of them corresponds to a different synchronization procedure in each IRF moving with dimensionless velocity β* with respect to S_0 *(hence, e_1 is called "synchronization parameter")*[6] *and, according to Selleri, "a different theory".* The choice $e_1 = 0$ turns out to be consistent with the relativity of space and time, but not with the relativity of simultaneity. As a consequence "absolute simultaneity" can be re-introduced in physics, against the "relative simultaneity" (which is a typical feature of SR) and in agreement with the "realistic" (Lorentz-like) ideological assumption that a privileged IRF, namely the IRF in which the ether is at rest, actually exists.

3.4.2 Testing the consequences

The consequences of SR have been widely tested. Furthermore, the results of SR are used in many areas of physics and are even important in everyday life. Most high-energy experiments at the big accelerators cannot be interpreted without SR. GPS, telecommunication, satellite ranging, etc. are heavily based on the validity of SR.

In addition, hundreds of dedicated experimental tests of SR that can be found in literature [Rob08]. They are using matter and light and have achieved very high sensitivities to hypothetical tiny deviations well below parts in 10^{30} from the Lorentz symmetry. Some of that (as, among the others, the tests of Michelson-Morley) have been realized before the Einstein's formulation and have been repeated and reproduced using modern techniques

[6] Of course all possible functions $e_1(\beta)$ must satisfy the limiting condition $\lim_{\beta\to 0} e_1(\beta) = 0$, so that eqns. (3.8) reduce to identity for vanishing β. Provided this obvious constraint is satisfied, the IRF S_0 turns out to be Einstein-synchronized for any choice of the synchronization parameter e_1.

to improve the accuracy of the results.

This thesis presents a novel test of anisotropy of nature performed by studying a possible anisotropy of time dilation. In particular, tests relevant for this thesis are those aimed at verifying the isotropy of physical quantities (in particular, the speed of light) and tests of time dilation (a possible anisotropy of time dilation might affect time dilation itself).

Tests of time dilation

The concept of time dilation was first introduced by Larmor in 1900 commenting the Fitzgerald-Lorentz contraction. According to Larmor's concept a clock moving with a velocity v through ether will go slower than a stationary clock by a factor of $\sqrt{1-v^2/c^2}$. This dilation has an absolute meaning.

In contrast with Larmor's concept, the time dilation of special relativity seems to be a relative concept so that the so called clock paradox or twin paradox has generated other controversies.

$$\Delta\tau'_A = \Delta t_{BA}\sqrt{1-\frac{v_R^2}{c^2}} \quad \text{or} \quad \Delta\tau_{\mathrm{A}} = \Delta \mathrm{t}_{\mathrm{B'A'}}\sqrt{1-\frac{\mathrm{v}_{\mathrm{R}}^2}{\mathrm{c}^2}}\,. \tag{3.9}$$

where

$$\begin{aligned} \Delta\tau'_A &= t'_{A'} - t_{A'} & \Delta t_{BA} &= t_B - t_A, \\ \Delta\tau_A &= t'_A - t_A & \Delta t_{B'A'} &= t_{B'} - t_{A'}. \end{aligned} \tag{3.10}$$

$\Delta\tau'_A$ and $\Delta\tau_A$ are proper time intervals, while $\Delta t_{B'A'}$ Δt_{BA} are coordinate time intervals. One clock A' is running slower than the difference between the readings of the two synchronized clocks A and B, or the one clock A is running slower than the difference between the readings of the two synchronized clocks A' and B'. A moving clock is running slower than two stationary separate clocks. The proper time interval $\Delta\tau'_A$ (or $\Delta\tau_A$) is smaller than the coordinate time interval Δt_{BA} (or $\Delta t_{B'A'}$). This statement is based on Einstein's synchronization between the two separate clocks.

Experimental tests on time dilation began in 1938 with Ives and Stilwell's work of the transverse Doppler effect due to atoms in inertial flight. Rossi and Hall (1941) inaugurated the era of fast moving elementary particles that dominated the scene until the discovery of the Mössbauer effect (1957).[7] This discovery suggested the use of photons emitted without

[7]The Mössbauer effect (1957) is a nuclear process permitting the resonance absorption of gamma rays.

recoil in crystalline solids for testing time dilation [BoGi00].

Direct tests of lifetime dilation of unstable particles in flight

The time dilation phenomenon of SR describes the observation that the lifetime of fast moving unstable particles would increase by a factor $(1 - v^2/c^2)^{-1/2}$ compared to the same particle at rest. A measurement of lifetime will provide a test of the prediction.
Let the number of unstable particles at the beginning be N_0. The rate at which a given type of particle decays is proportional to the number of particles, N, as follows:

$$\frac{dN}{dt} = -\alpha N \Longrightarrow N(t) = N_0 e^{-t/\tau_0} \,. \tag{3.11}$$

The "mean life" τ_0 of a particle at rest is called the "proper lifetime". Considering moving particles the time t in the equation 3.11 should be replaced by t/γ due to the time dilation effect, and thus the law of decay should be

$$N(t) = N_0 e^{-t/\gamma\tau_0} = N(t) = N_0 e^{-t/\tau} \tag{3.12}$$

where τ is the mean lifetime for unstable particles in flight: $\tau = \gamma\tau_0$. The equations above can be rewritten as

$$N(t) = N_0 e^{-vt/v\tau_0} = N_0 e^{-x/\lambda} \tag{3.13}$$

$$\lambda = v\tau = \frac{v\tau_0}{\sqrt{1 - v^2/c^2}} = \frac{p\tau_0}{M_0} \tag{3.14}$$

where $x = vt$ is the path through which the particles pass during the time t, λ is the mean free path for the particles (when $x = \lambda$, $N/N_0 = e^{-1}$), M_0 is the rest mass of the particles and p is the momentum.
There are two ways for testing 3.12 or 3.13. The first is to determine the number of unstable particles which have decayed in traversing a known flight path by measuring the number of remnants particle at two separate positions of flight path. The second is to measure the relationship between the decay rate of unstable particles and their velocity (or their momentum). In the performed experiment, the values of the proper time τ_0 where measured by making the flying particle stop in the targets, and the observed values of the mean lifetime (τ) of the particle were determined by means of the above two methods.

It is made possible by fixing atomic nuclei in the lattice of solids so that energy is not lost in recoil during the emission and absorption of radiation.

The theoretical values of τ to be used to compare with the observed values is calculated from time dilation, and the value of the factor γ is calculated using the equation of SR $p = (\gamma M_0 c^2)$ (or $E = \gamma \mathrm{M}_0 c^2$) and the observed values of the momentum p (or the energy E). The first experiment of this type was carried out by Rossi and Hall in 1941 [RoHa41].

Lifetime of cosmic muons. Time dilation is observed in cosmic radiation of particles like the muons, μ. The μ is a lepton[8] with an average lifetime $\tau_0 \simeq 2.2\,\mu$s. Cosmic muons are mostly created in the upper atmosphere when fast protons ($\sim$TeV energy) collide with nuclei.

About 1940, Rossi and Hall dealt with the decay of the muons. The measurements were taken around Denver (Colorado) at different altitudes. The decay of muons has provided verification of Lorentz's time dilation to a high degree of accuracy.

Lifetime of particles produced by accelerators. Various experiments have been conducted in laboratory measuring the lifetime of charged pions in flight. First Lederman observed in 1951 the decay process $\pi^- \rightarrow \mu^- \nu^0$ for a beam of flying π^-mesons with a velocity of $\sim 0.73c$ (corresponding to the dilation factor $\gamma \sim 1.5$) produced by an accelerator, and obtained the free path λ of (9.93 ± 1.10)m which implied a lifetime for a flying pion of $\tau = (4.55 \pm 0.52) \times 10^{-8}$s. When corrected for time dilation, this provided a lifetime of $\tau_- = (2.55 \pm 0.19) \times 10^{-8}$ s.

In 1971 Ayres et al. compared the lifetimes of 300 MeV ($\gamma = 2.45$) $\pi^\pm$ produced at a cyclotron by measuring the fraction of surviving pions at several positions along a 1000-cm (one-half lifetime) decay path. The velocity of the pions, measured by time-of-flight, was used to calculate γ. The time dilated lifetime was found to agree with the prediction of SR to within 4×10^{-3}.

A series of measurements for the lifetimes of muons in flight were realized at the last CERN g-2 experiment in muon storage ring by Bailey et al. [Bail77] In 1977 in separated measurement for μ^+ and μ^- the muons of velocity $0.9994c$ were found to have a lifetime 29.3 times the laboratory lifetime. For μ^+, where the lifetime at rest is known with the best accuracy, the ratio τ^+/τ_0 was found to agree with time dilation predicted by the Lorentz transformations to within $(2 \pm 9) \times 10^{-4}$.

[8] By mistake it was called μ-meson in the first, historical papers.

3.4.3 Miscellaneous experiments finding positive evidence for ether drift

The majority of the scientists does not recognize the need for an ether, today. However, the motion of the Solar System towards the CMB system seems established.

What does this mean? Orthodox scientists affirm that the apparent asymmetry is due to the existence of matter. However, it is difficult to think of a Universe without matter.

Besides the recognized (also by orthodoxy) experiments claiming evidence for motion with respect to the CMB, other experiments claiming detection of motion with respect to an ether exist, through anisotropy of the speed of light. Most such experiments use rotating frames. A list of peer-reviewed experiments follows.

Summary of ether drift experiments measuring a nonzero Earth velocity in absolute space

(Compiled by Stoyan Sarg [Sarg])

Authors I-st publ.date	Epoch	RA	δ	l	γ	V(km/s)	Type
Miller 1933	1925-26	4h54m	$-70°33'$	282°	-35.2°	208	Interferometer, continuous light
Illingworth anal. by Cahill 2003	1927					369±123	Interferometer continuous light
Marinov 1983	1973	Earth abs. velocity along instrument axis				130±100	Rotating mirrors chopped light
Marinov 1980	1975-76	$13h23' \pm 20'$	-23±4°	313°	38.9°	303±20	Interferometer, rotating mirrors
Muller et al.	1976	Velocity towards Leo				∼400	CMB
Smoot+ 1977	1977	11°±0.6°	6±10°	245±15°	54±10°	390±60	CMB
Wilkinson Corey	1978(?)	12h±1h	-21°±21°	288°	40°	320±80	CMB
Monstein Wesley 1996	1978-96	8.7°±3.5′	-1.1°±10°	227.9°	24.3	359±180	Muon flux anisotropy
Marinov 1995	1984	12.5h ±1h	-24°±7°	397.5°	38.4	362±40	Coupled shutters, chopped light
Silvertooth 1986						378±?	Rotating mirrors, chopped light
Consoli et al. 2006		202°	-44°	309°	18°	276±71	Analysis of rotating optical resonators

4

K^0_S lifetime and a novel test of the isotropy of the Universe

4.1 Introduction

This chapter is divided in two parts: the first part describes the analysis of the measurement of K^0_S lifetime performed by KLOE; the second one illustrates the study of the K^0_S lifetime measured in a frame of reference fixed to the solar system, in opposite directions with respect of the motion of the solar system in the CMB reference frame. The measurement uses the decays into $\pi^+\pi^-$ pairs.

The choice of the KLOE experiment for the measurement of K^0_S lifetime was made because it is the ideal to perform a measurement of lifetime having an almost monochromatic K^0_S beam and a very high statistics of events.

The statistical error on the lifetime depends on the number of events ($\propto 1/\sqrt{N}$) and, very strongly, on the time interval covered. The statistical error on the lifetime obtained fitting a decay curve over a time interval Δt can be approximated [Fra92] by:[1]

$$\frac{\delta\tau}{\tau} = \frac{1}{\sqrt{N}} \times \frac{e^T - 1}{\sqrt{1 + e^{2T} - e^T(2 + T^2)}} \tag{4.1}$$

where $T = \Delta T/\tau$ is the time interval observed in K^0_S lifetime units.

[1] This formula is the standard maximum likelihood estimator error evaluation for an exponential probability distribution function integrated over a finite time interval Δt. It neglects other sources of statistical error then the number of samplings.

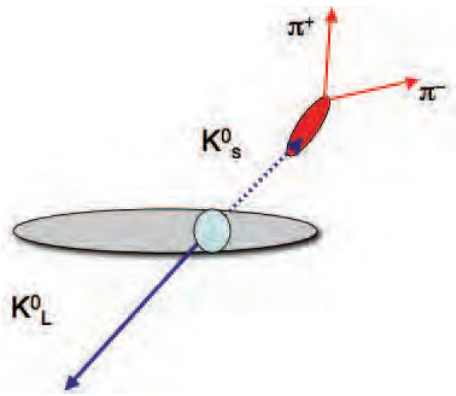

Figure 4.1: The K^0_S flight length is reconstructed in the xy plane perpendicular to the beam axis (z).

The K^0_S lifetime has been determined with the method of the measurement of decay length. The K^0_S proper time has been calculated. Then a fit to the proper time distribution (following, in the absence of errors, an exponential law) has been performed.

The main problem with measuring the K^0_S lifetime in KLOE is that the lifetime, ~ 90 ps, is comparable with the resolution in the proper time, which is of about 30 ps. That could be overcome by the very large statistics available in KLOE.

4.2 Determination of the proper decay time

The K^0_S mean lifetime measurement $\tau_{K^0_S}$ is calculated by fitting the distribution of the proper time. This is the time elapsed from K^0_S creation, that is when the incident electron and positron annihilate, until the decay, that is when the K^0_S creates a $\pi^+\pi^-$ pair. Figure 4.1 shows a K^0_S decaying to π^+ π^- after being produced in the beam interaction region. In Fig. 4.1 the K^0_S is produced at a point near the beam centre (the interaction point IP) and travels a certain distance (the flight distance d) in a time t before decaying in a point called the "vertex" into its π^+ π^- daughters. These daughters are subsequently measured by the tracking system. The distance traveled prior to decay is related to the proper time through the velocity $v_{K^0_S}$ of the kaon

$$d = v_{K^0_S} t = v_{K^0_S} \gamma t_0, \quad \gamma = 1/\sqrt{1-(v/c)^2}\,. \tag{4.2}$$

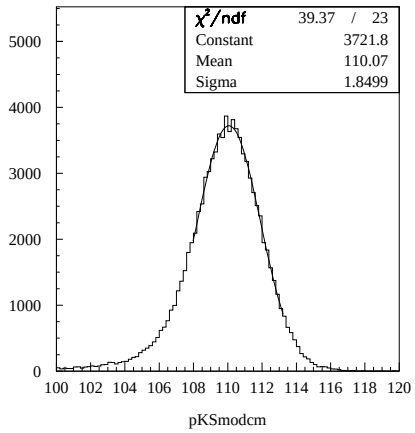

Figure 4.2: An example of the distribution of the momentum of the K_S^0.

The proper time t_0 of each K_S^0, t_0, is obtained from the relation

$$t_0 = \frac{d_{K_S^0}}{\beta_{K_S^0}\gamma c} = \frac{d_{K_S^0} M_{K_S^0}}{p_{K_S^0}} \tag{4.3}$$

being $p_{K_S^0}$, $M_{K_S^0}$ and d, respectively, the momentum, the mass of K_S^0 and the K_S^0 path, i.e., the distance of $K_S \to \pi^+\pi^-$ decay vertex from the interaction point (IP), evaluated event by event. All the kinematic variables that appear in the 4.3 are well known in KLOE. The mass of the K^0 as reported in Chapter 2 Section 2.5.1 is

$$m_{K^0} = (497.583 \pm 0.005_{\text{stat}} \pm 0.020_{\text{syst}}) \quad \text{MeV}. \tag{4.4}$$

The distribution of the K_S^0 momenta is shown in Fig. 4.2; it peaks at 110 MeV. As already mentioned, central to KLOE K_S^0 studies is the use of the $K_L - crash$ tag: the position of the $K_L - crash$, together with the kinematics of the $\phi \to K_S^0 K_L^0$ decay, determines the trajectory of the K_S^0 with a momentum resolution of approximately 0.6 MeV and an angular resolution of better than 1°.

Because of the correlation between the uncertainty in the momentum calibration and the vertex position a correct calibration of K_S^0 momentum has been carried out.

The particle's momentum is defined from the curvature of its trajectory in the magnetic field In KLOE a redundant information of the kaon momentum is available. The first obvious determination comes from adding the pion momenta, $\vec{p}_{\pi\pi}$. On the other hand, in the ϕ rest frame, kaons are produced back to back. Hence, from the knowledge of

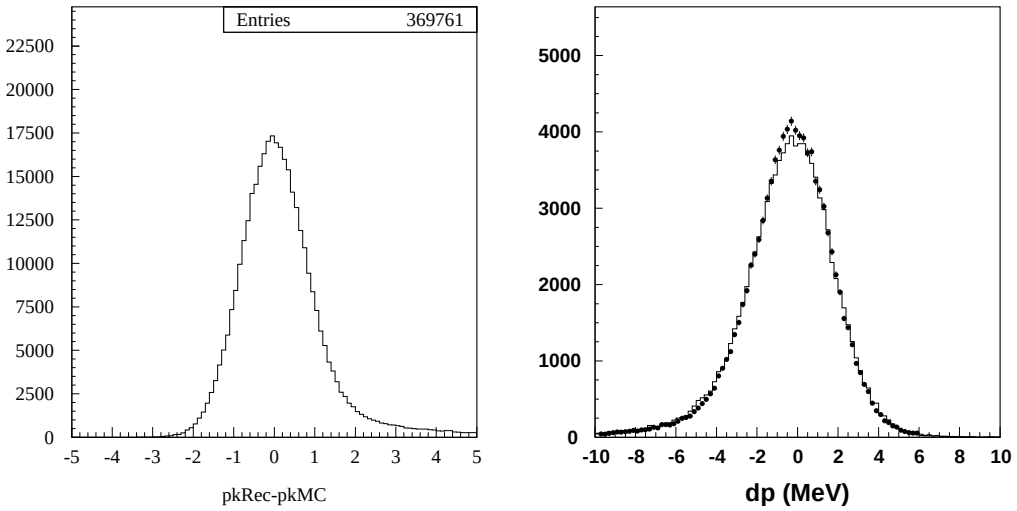

(a) (b)

Figure 4.3: K^0_S momentum. (a) MC: residual, $|\vec{p}_{K^0_S}|_{Rec} - |\vec{p}_{K^0_S}|_{MC}$; (b) $dp = |\vec{p}_{\pi\pi}| - \left|\vec{p}_{K^0_S}\right|$: dots are data, line is MC. The tails in (a) and (b) are due to ISR.

$\sqrt{s}$ the energy of each kaon is fixed and $K_S \to \pi^+\pi^-$ vertex decay position revels its direction, allowing in this way a straightforward determination of kaon momentum, $p_{K^0_S}$. The calibration has been applied on the data in order to reproduce the Monte Carlo result for $p_{K^0_S}$ (Fig.4.3 (a)). Based on this determination of $p_{K^0_S}$ and a comparison of $dp_{K^0_S}$ and on the redundancy of the parameters a comparison in determining $dp = |\vec{p}_{\pi\pi}| - \left|\vec{p}_{K^0_S}\right|$ has been performed (Fig.4.3 (a)). The tail that is visible on both the pictures of Fig.4.3 is due to an overestimate of the kaon momentum $|\vec{p}_{K^0_S}|$ with respect to $|\vec{p}_{\pi\pi}|$, the kaon momentum as obtained from pions. The center of mass energy, $\sqrt{s}$, is determined in each run from large angle Bhabha events, and the initial state radiation of hard photon emission (ISR) can affect, in a single event, the total energy. No cut is applied to remove the tail at this stage. Later, during the attempt to improve time resolution (see Sec.4.5.2), a tight cut on the invariant mass, $|M_{\pi\pi} - M^0_K| < 2\sigma$, was imposed to remove the tail (Fig.4.4).

Notice that in Eq. (4.3), when computing the proper time, the Lorentz transformations and the equations of Special Relativity have been used.

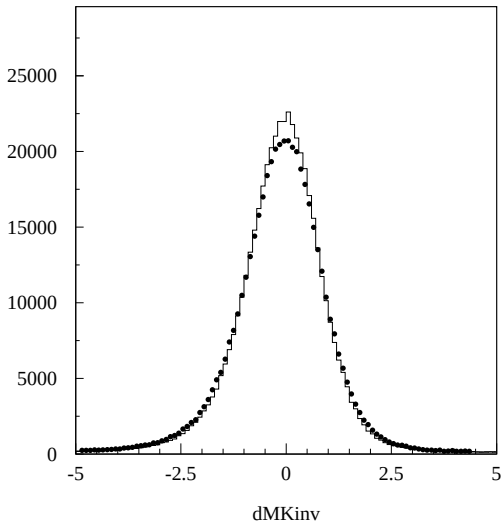

Figure 4.4: Invariant mass distribution (residual) from pions. Dots are data, line is MC.

4.3 Experimental setup

In both studies performed in this work, data collected with the KLOE detector [KLOE08] at the DAΦNE ϕ-factory are used. The peculiarity of a ϕ-factory is that kaons are produced in pairs, namely $K^+K^-$and $K^0_S K^0_L$. Therefore the detection of a K guarantees the presence of a $\bar{K}$ on the other side with known momentum and direction. The ϕ mesons decay with a branching ratio (BR) of $\sim 34\%$ into nearly collinear back-to-back $K^0_S K^0_L$ pairs. Kaons get a momentum of $\sim$ 100 MeV/c which translates into a low speed, $\beta_K \sim 0.2$. The decay products of a $K^0_{L,S}$ pair define two separated regions called hereafter tag and signal hemispheres. To measure the K^0_S lifetime the sub-sample of events is selected by the tag K^0_S and K^0_L have different mean decay lengths: $\lambda_S \sim 0.6$ cm, $\lambda_L \sim 340$ cm. The kaon pairs K^0_L and K^0_S from ϕ decay, produced in a pure $J^{PC} = 1^{--}$ quantum state, are observed in two well separated hemispheres, except for the events with prompt K^0_L decays. The K^0_S "fiducial volume" extends for a few centimeters around the interaction point (IP), while the K^0_L "fiducial volume" starts at least ∼50 cm far from the IP.

It is possible then to select a sample of K^0_S (K^0_L) with given momentum and direction by detecting the presence of K^0_L (K^0_S) decays or interactions in properly defined fiducial volumes. This procedure is called "$K^0_S(K^0_L)$ tagging" and the selected samples are said to be K^0_S–tagged (K^0_L–tagged).

4.4 Data and specifications

The lifetime of the short-lived neutral K meson has been determined based upon two series of data production of K^0_S, which subsequently decayed via the charged mode $K^0_S \to \pi^+\pi^-$ collected by the KLOE detector practically free of background. The full statistics of events $K^0_S K^0_L$ available was about 500 $\times 10^6$ corresponding to an integrated luminosity of 500 pb^{-1}, collected in the period from July 2004 to December 2004. During the year 2005 the statistics was off about 1250 $\times 10^6$ events. The 2004 data are divided into 34 run periods while the 2005 data are divided in 65 run periods, each period corresponding to an integrated luminosity of about 15 nb^{-1}. For each data period, there is a corresponding sample of Monte Carlo (MC) events with approximately 3 times equivalent statistics.

The K^0_S lifetime has been calculated using 2004 data only; the analysis of the systematic errors on 2005 data is in progress. However, the statistical error being smaller than the systematic error, the completion of the analysis is expected to add little to the result. Since in the study of asymmetries systematic errors largely cancel, the analysis of asymmetry has been performed on both the 2004 and the 2005 data.

In the following the analysis of K^0_S lifetime made with the data collected during 2004 is reported in detail. All the cuts made, specified in the following sections, have reduced the population of the 2004 data used in this analysis to about 17.8 million events.

All the results have been checked out and adjusted using MC simulation. The KLOE MC simulation program, GEANFI, is based on the GEANT 3.21 library [GEANT84, GEANT78] widely used in high-energy and astroparticle physics experiments. GEANFI incorporates a detailed description of the KLOE apparatus, to simulate the particle interactions inside the detector, including the tracking in the magnetic field, the electromagnetic shower development, the ionization energy loss, the multiple scattering, etc. The library provides also the tools for the description of the materials, the geometry and the magnetic fields of the experimental setup.

A set of specialized routines has been developed to simulate the response of each detector, starting from the basic quantities obtained from the GEANT particle-tracking and energy-deposition routines.

4.5 Measurement of the K_S^0 lifetime

The basic steps involved in measuring the kaon lifetime are:

1. sample selection and test with MC;
2. time resolution and analysis cuts; calculation of efficiency;
3. fit to proper time distribution;
4. fit result and stability;
5. evaluation of the systematic uncertainty.

4.5.1 Sample selection and tests with MC

As mentioned above, from a sample of $\sim 5 \times 10^8$ $K_S K_L$ pairs following the reaction $e^+e^- \to \phi \to K_S K_L$ collected during the year 2004, $\sim 17.8 \times 10^6$ $K_S^0 \to \pi^+\pi^-$ decays tagged by events $K_L^0 \to \pi^0\pi^0\pi^0$ have been selected.
The algorithm that determines the proper K_S^0 lifetime and the error of a single particle decay use the pion's tracks, the beam information and requires the reconstruction of the IP kaon decay vertex. The positions (hits) of the passage of charged particles are reconstructed to determine the trajectories of the charged tracks and therefore measure their directions and momenta. The reconstruction program was designed to search for events with a good track and a good vertex topology. To reach this goal it is necessary to make an accurate selection of the "good" events. A tracking fit is performed with the pions hits; quality cuts are applied on the fit.
Some basic cuts are made in order to have usable data:

- a cut on the quality of the fit of the secondary vertex;
- the invariant mass must be $|M_{\pi\pi} - M_K| < 5\ \sigma$, being $\sigma \sim 1$ MeV, assuming each track to be a pion.

This initial filtering process removes most background events with wrong topology, but a significant portion of background events with the desired topology survives. After the kinematic cuts described above, the contamination, dominated by $K_L^0 \to \pi e \nu$ decays, is

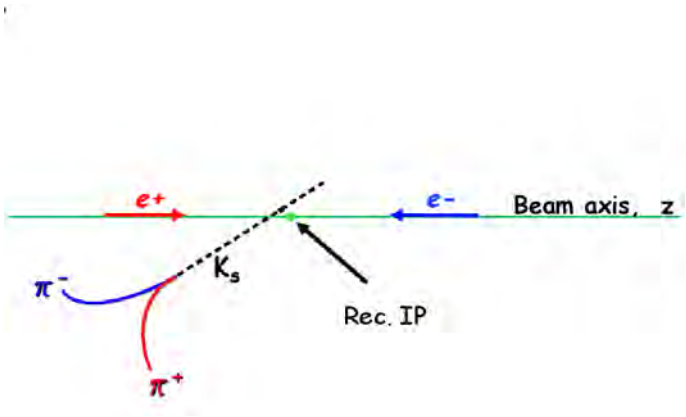

Figure 4.5: Determination of IP from K^0_S line of flight.

∼4%. The particle identification (PID), based on calorimeter information, can further reduce the contamination.

As said before for each event one has to evaluate the interaction point position, mainly in z position (along the beam axis), which is known only roughly, with an accuracy of about 2-3 cm only. The strategy chosen to evaluate the IP position is considering the line of flight of K^0_S as obtained from pion tracks: the IP is the point of minimum approach to this line on the (z) beam axis. The method is sketched in Fig.4.5. The correctness of the method is visible in Fig.4.6, where a resolution of about 2 mm has been obtained for the z coordinate of IP. Events with reconstructed IP with $|z_{IP}| > 2\,\text{cm}$ are rejected.

Test on K^0_S flight direction with $K_L - crash$

Testing the K^0_S line of flight has a relevant importance to avoid possible systematic errors. To do that a sample of K^0_L reaching the calorimeter before decaying ($K_L - crash$) is selected. The K^0_L impact point position on the calorimeter and the knowledge of the ϕ momentum in the lab frame constrain the K^0_S direction with a a good resolution due to the large distance of the calorimeter (about 2 m) with respect to K^0_S decay vertex. The K^0_S direction as obtained from the decay vertex is then compared with that obtained from the $K_L - crash$ method. The plot of Fig.4.7 shows the angle α between the two directions.

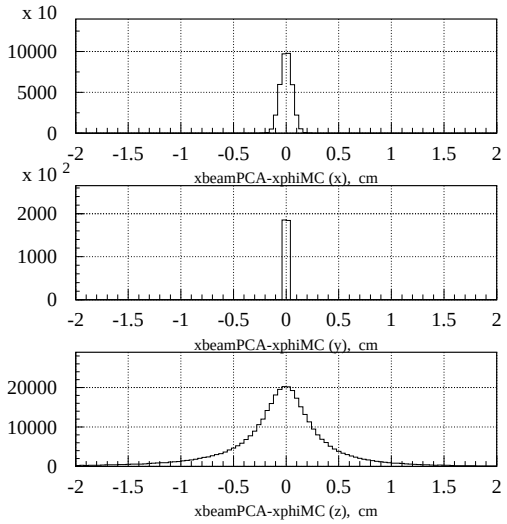

Figure 4.6: Monte Carlo: reconstructed interaction point. $IP_{rec} - IP_{MC}$ is shown for each coordinate.

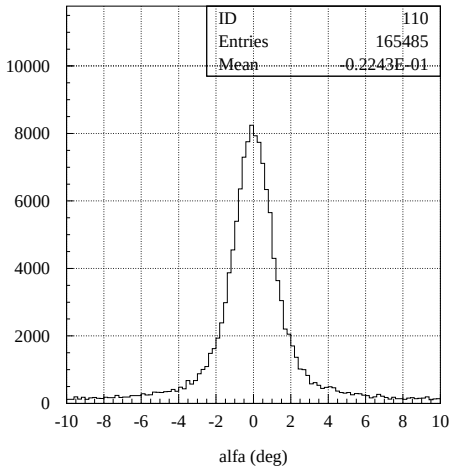

Figure 4.7: Angle between the K_S^0 direction as reconstructed from K_S^0 vertex decay and that obtained from the $K_L - crash$ method.

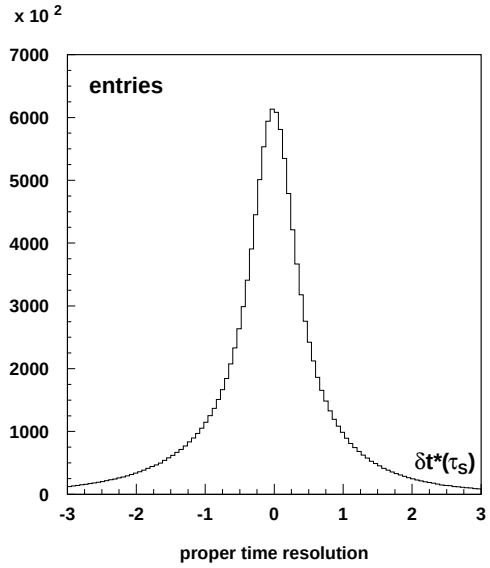

Figure 4.8: Monte Carlo: proper time resolution $t^\star - t^\star_{MC}$, in units of $\tau_{K^0_S}$, after the selection cuts.

4.5.2 Time resolution and analysis cuts. Efficiency.

After the sample selection described in Sec.4.5.1 the proper time distribution (residual) as obtained from Eq.4.3 is shown in Fig.4.8. The distribution has an RMS of $0.86\,\tau_{K^0_S}$ and shows a shape not perfectly symmetric. Hence, more cuts have been applied in order to improve the time resolution, i.e., the vertex resolution. A variable very sensitive to the vertex reconstruction is dp i.e. $|\vec{p}_{\pi\pi}| - |\vec{p}_K|$. The determination of the vertex position depends on the measurement of the tracks curvature. Therefore, a bias on the vertex position determination is correlated with a non zero value of the variable dp. The applied analysis cuts reject regions in which dp assumes too high values. In addition a correction to the vertex position has been applied in data to account for such a bias.

As said before, a first (hard) cut is applied on the pion's invariant mass, in order to remove the tail due to ISR, $|M_{\pi\pi} - M_K| < 2\ \sigma$.

Cut on $\cos\theta_{12}$**.**

Fig. 4.9a shows the $\cos\theta_{12}$ distribution, where θ_{12} is the pion opening angle, for data and Monte Carlo. In Fig.4.9 dp is shown as a function of $\cos\theta_{12}$. To avoid large values of dp only events satisfying $\cos\theta_{12} < -0.87$ have been retained.

Cut on $\cos\theta_1 + \cos\theta_2$**.**

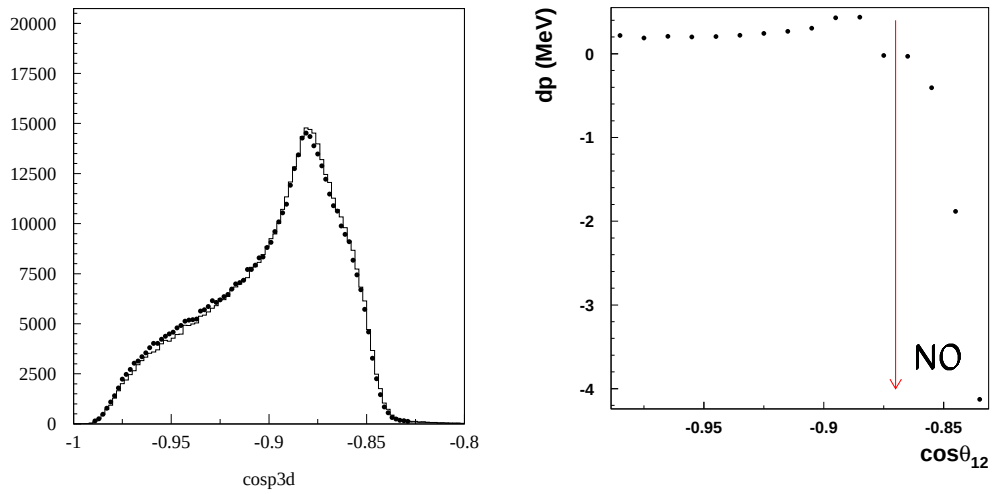

(a) (b)

Figure 4.9: (a) $\cos\theta_{12}$ distribution, with θ_{12} opening angle between the pions. Dots are data, line is Monte Carlo; (b) dp versus $\cos\theta_{12}$.

Fig. 4.10a shows the distribution of the sum of the pion polar angles, i.e., $\cos\theta_1 + \cos\theta_2$, for data and Monte Carlo. In Fig.4.10b is shown the dp as a function of $\cos\theta_1 + \cos\theta_2$. To avoid great values of dp only events satisfying $|\cos\theta_1 + \cos\theta_2| < 0.3$ have been retained.

Cut on $\cos\theta_1 + \cos\theta_K$.

Fig.4.11a shows the distribution of $\cos\theta_1 + \cos\theta_K$, with θ_1 and θ_K the polar angle of the positive pion and of the K^0_S respectively, both for data and Monte Carlo. In Fig.4.11b dp as a function of $\cos\theta_1 + \cos\theta_{K^0_S}$ is shown. To avoid large values of dp only events satisfying $|\cos\theta_1 + \cos\theta_K| < 1$ have been retained.

Cut on $\theta^{\perp}_{12}$.

A further cut is applied on the opening angle of the pions, projected on the transverse plane, $\theta^{\perp}_{12}$. In Fig.4.12a the distribution for data and Monte Carlo is shown. To avoid large values of dp only events satisfying $|\theta^{\perp}_{12}| > 2.6$ rad have been retained.

Cut on $\theta^{\perp}_{\pi K}$.

The last analysis cut concerns the opening angle, projected on the transverse plane, between the positive pion and the kaon, $\theta^{\perp}_{\pi K}$. In Fig.4.13a the distribution for data and Monte Carlo is shown. This is a very important variable because the reconstruction of the K^0_S vertex position, VTX, produces a little bias depending on this angle .

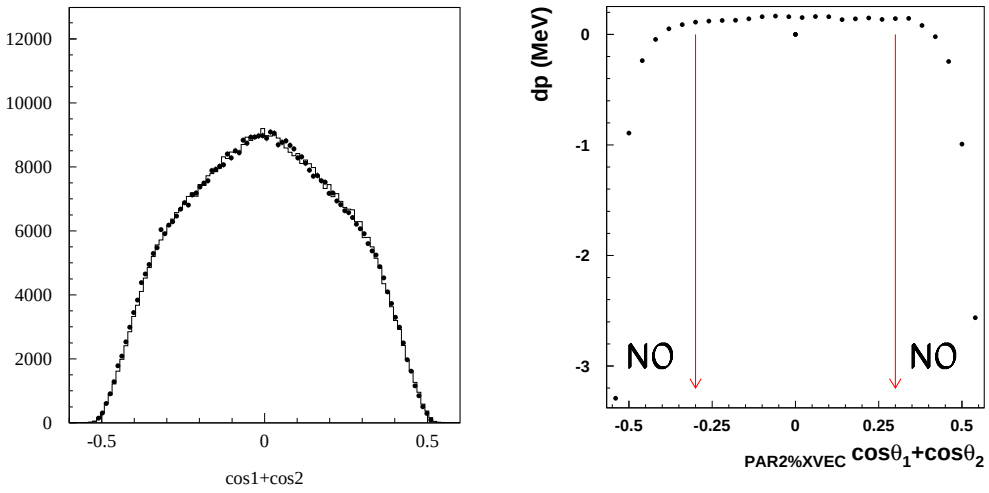

(a) (b)

Figure 4.10: (a) $\cos\theta_1 + \cos\theta_2$ distribution. Dots are data, line is Monte Carlo; (b) dp versus $\cos\theta_1 + \cos\theta_2$.

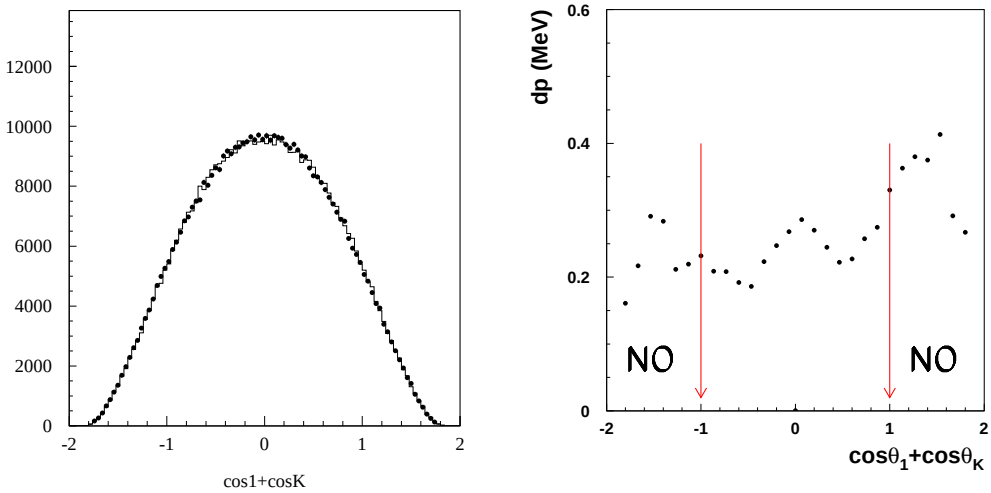

(a) (b)

Figure 4.11: (a) $\cos\theta_1 + \cos\theta_K$ distribution. Dots are data, line is Monte Carlo; (b) dp versus $\cos\theta_1 + \cos\theta_K$.

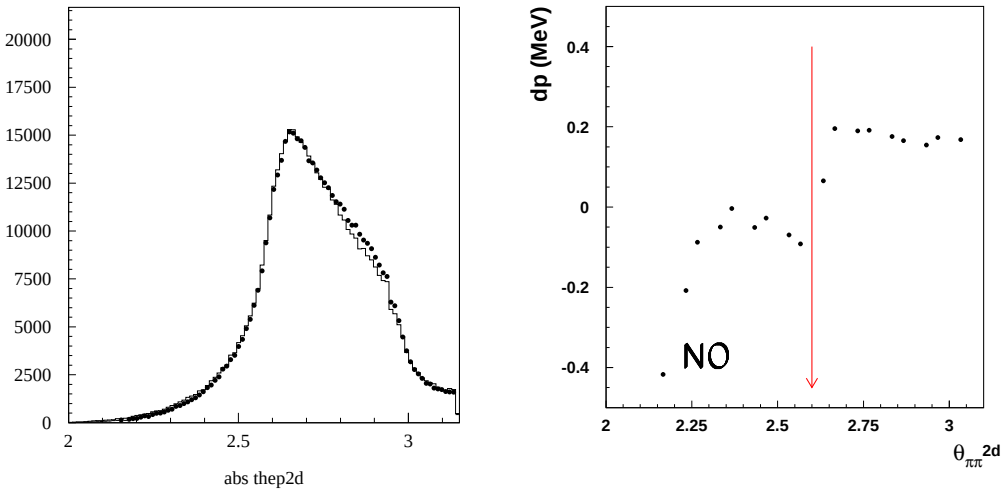

(a) (b)

Figure 4.12: (a) $|\theta^{\perp}_{12}|$ distribution. Dots are data, line is Monte Carlo; (b) dp versus $|\theta^{\perp}_{12}|$.

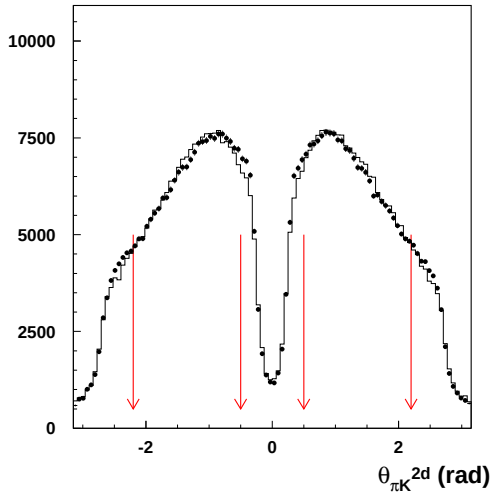

(a)

Figure 4.13: $\theta^{\perp}_{\pi K}$ distribution, rad. Dots are data, line is Monte Carlo.

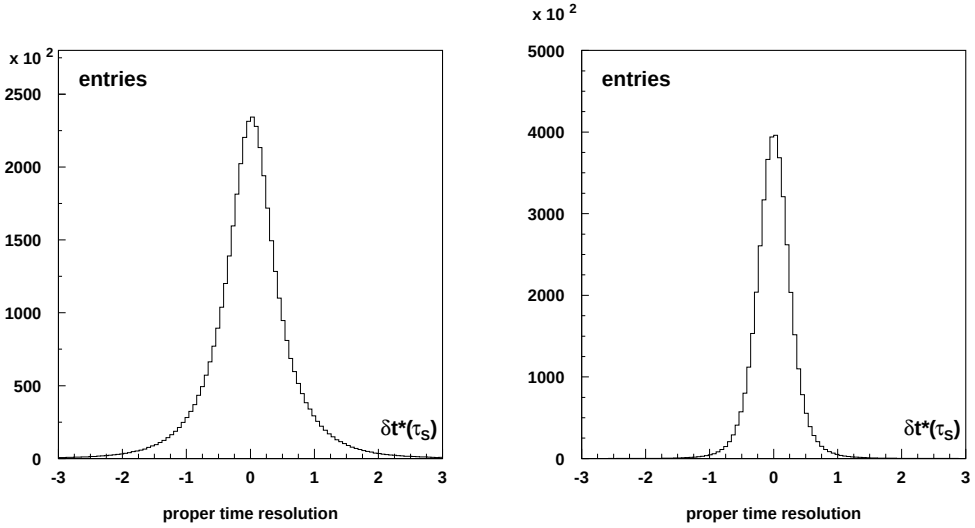

(a) (b)

Figure 4.14: Monte Carlo: proper time resolution $t^\star - t^\star_{MC}$, in units of $\tau_{K^0_S}$: (a) after the cuts described in this section ; (b) after geometrical fit method.

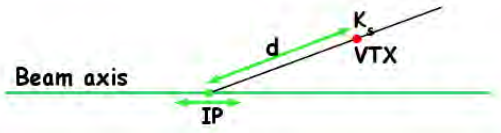

Figure 4.15: Geometrical fit method. Assuming as correct the K^0_S line of flight the IP is moved along the beam (z) axis.

At the cost of reducing by a factor of about three the efficiency, these cuts improve the time resolution. The distribution is now more symmetrical with an RMS of $0.63\,\tau_{K^0_S}$ (Fig. 4.14a). After all these cuts the contamination from $K_S \to \pi^+\pi^-\gamma$ decay is at level of $\sim 10^{-4}$. A further, very meaningful improvement in the proper time resolution is finally obtained by applying a geometrical fit method. Event by event, as described in Sec.4.5.1, the position of the K^0_S decay vertex (VTX) and the IP have been evaluated. In particular, the IP determination refers basically to the z position on the beam axis. Assuming as correct the kaon line of flight (KLF) direction, the method (Fig.4.15) adopted consists in moving the IP along the z axis and searching for a new VTX which belongs to the line, parallel to the KLF direction and originating from the new IP, in order to minimize a

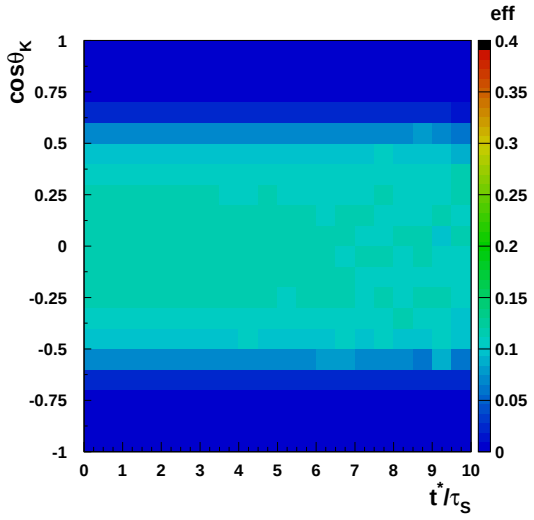

Figure 4.16: Final efficiency as a function of proper time and kaon polar angle (MC).

χ^2-like function

$$\chi^2 = \frac{\left|\vec{x}^{new}_{vtx} - \vec{x}^{old}_{vtx}\right|^2}{\sigma^2_{vtx}} + \frac{(z^{new}_{IP} - z^{old}_{IP})^2}{\sigma^2_{z,IP}} \,. \tag{4.5}$$

Fit parameters are the IP position on the beam axis, z^{new}_{IP}, and the distance d, evaluated along the K^0_S line of flight, which constrain the new vertex position, $\vec{x}^{new}_{vtx}$. In Fig.4.14 b the proper time distribution (residual) after applying this method is shown. The improvement was by more than a factor of two, i.e., a RMS error of $0.32\,\tau_{K^0_S}$. After all cuts described in this section the final efficiency, as a function of proper time $t^\star$ and kaon polar angle $\theta_{K^0_S}$, is shown in Fig.4.16. Flat in $t^\star$, efficiency on average is about 9%.

4.5.3 Fit to proper time distribution

The proper time distribution fit is performed as a function of the kaon direction, because time resolution slightly depends on $\theta_{K^0_S}$. Because of that, and also because of the lacking of a control sample, a 18×20 $\left[\phi_{K^0_S}, \cos\theta_{K^0_S}\right]$ binned analysis has been performed.
After many checks a fiducial volume (FV) with $-0.5 < \cos\theta_{K^0_S} < +0.5$ and $-0.5 < \cos\theta_\pi < +0.5$ for both pions is then selected, assuring in this way a good result stability. With these conditions 180 independent fits have been performed. Fit parameters are the lifetime $\tau_{K^0_S}$, the three parameters $(\sigma_1, \sigma_2, \alpha)$ describing the two-gaussian resolution and their relative weight used to convolute the exponential decay function and a shift parameter, δ: this last has not a physical meaning, but it is mandatory to remove any

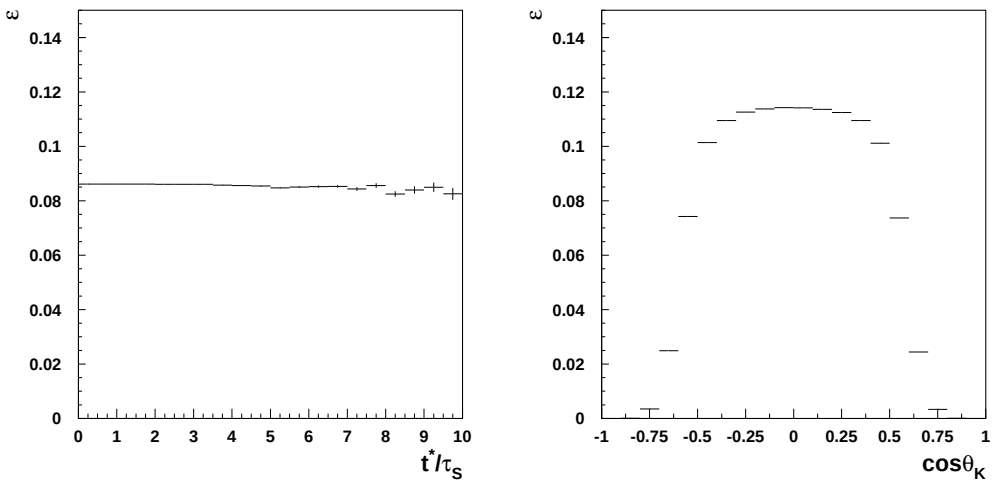

(a) (b)

Figure 4.17: Final efficiency as a function of: (a) proper time; (b) kaon polar angle.

possible further bias in IP or VTX determination. The transverse position of IP is assumed in each run from Bhabha events.

The fit range covers from -1 to +6.5 $\tau_{K^0_S}$ (15 time bins), in order to have enough statistics in each bin.

The binned fit function is derived from:

$$f(t) = A \int_{\infty}^{\infty} \theta(x) \frac{1}{\tau} \exp(x/\tau)\, \varepsilon(x)\, g(t + \delta - x)\, dx \tag{4.6}$$

where $\varepsilon(x)$ is the parameterized efficiency obtained from the simulation, $g(z)$ is the resolution function:

$$g(z) = \frac{\alpha}{\sigma_1 \sqrt{2\pi}} e^{-z^2/2\sigma_1^2} + \frac{1-\alpha}{\sigma_2 \sqrt{2\pi}} e^{-z^2/2\sigma_2^2} \tag{4.7}$$

and the constant A is normalized to the total number of events.

Obtaining and controlling an absolute result at a level of 10^{-4} is very hard to achieve. For this reason each of the 180 fits is made for Data and MC and the final result is obtained according to

$$\tau_S = \frac{\tau^{DT}_{fit}}{\tau^{MC}_{fit}} \times \tau_{MC} \tag{4.8}$$

where τ_{MC} is the K^0_S lifetime in the Monte Carlo.

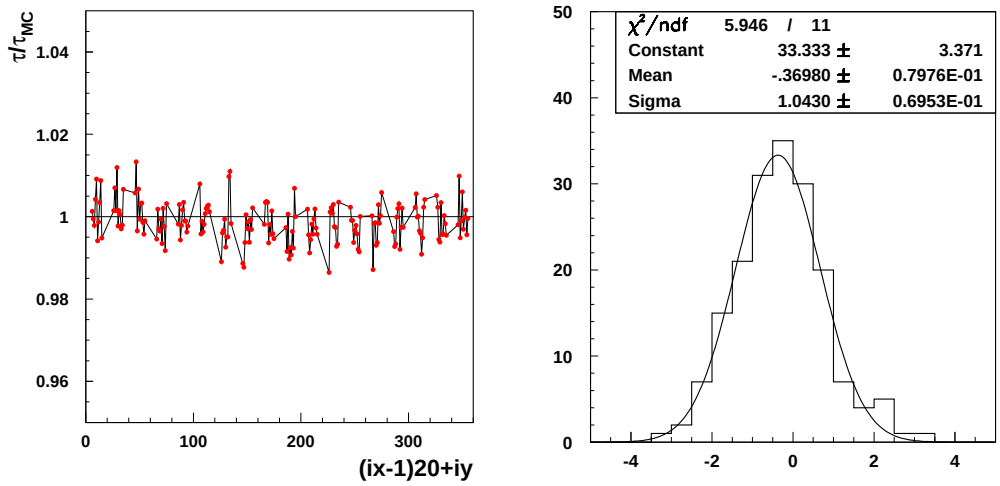

(a) (b)

Figure 4.18: Result of the 180 independent fits: (a) lifetime in units of τ_S, as a function of ϕ_K (ix) and $\cos\theta_K$ (iy); (b) corresponding pull distribution.

	τ_S	σ_1	σ_2	α	δ
τ_S	1	-0.001	-0.006	-0.06	+0.03
σ_1		1	+0.21	+0.14	-0.05
σ_2			1	+0.13	-0.09
α				1	-0.13
δ					1

Table 4.1: Correlation of the fit parameters.

Fit result and stability

Fig.4.18 a shows the distribution of lifetime result for the 180 independent fits, while Fig.4.18 b shows the corresponding pull distribution.

Fig.4.19 a shows a bin-fit example with 10 degrees of freedom (dof). Hence, the χ^2 distribution resulting from the 180 fits is compared with the expected one (Fig.4.19 b). In Tab.4.1 are shown the correlations of fit parameters. A check to the run stability has been performed. The 34 run periods have been divided in 5 groups of almost the same statistics. Fig.4.20 shows the stability for each group. The stability of the fit results as shown in Fig.4.18 is given separately for ϕ_K and $\cos\theta_K$ in Fig. 4.21.

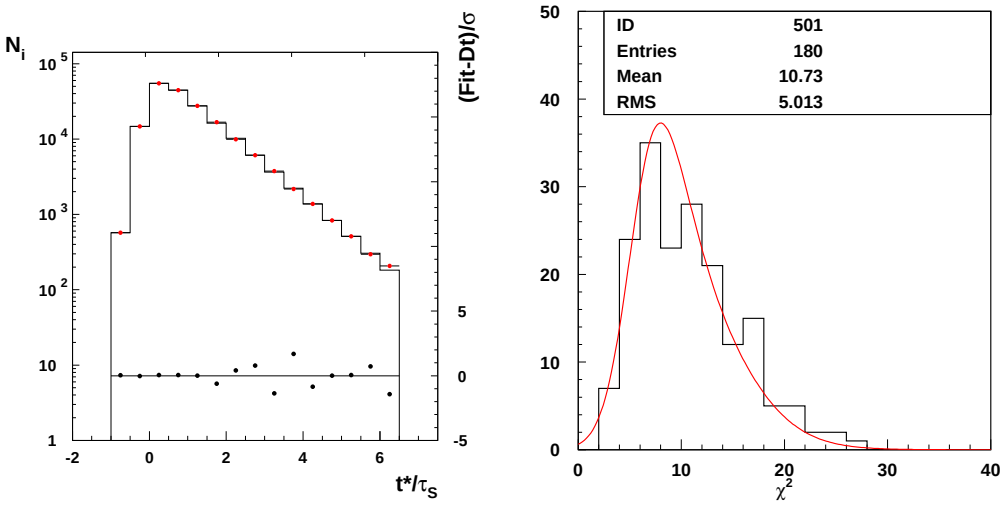

(a) (b)

Figure 4.19: Proper time fit: (a) a fit example with $\chi^2/\text{dof} = 8/10$ (dots and boxes are data and fit function, respectively); (b) χ^2 distribution for the 180 fits (histogram) compared with the expected χ^2 for dof=10 (line).

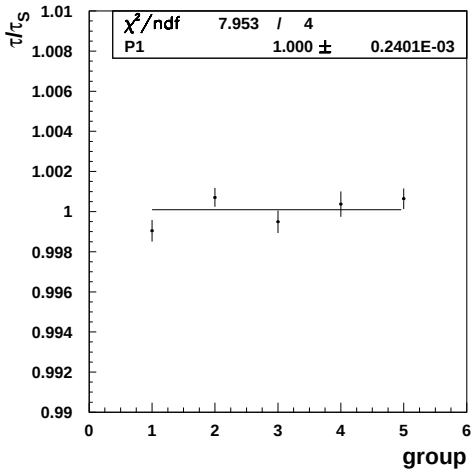

Figure 4.20: Stability of the fit result as a function of the period.

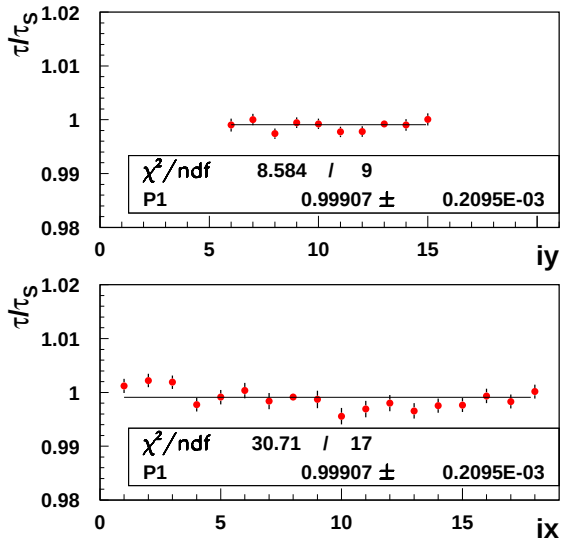

Figure 4.21: Stability of fit result. When ix ranges from 1 to 18 ϕ_K ranges from 0° to 360°; when iy ranges from 6 to 15 $\cos\theta_K$ ranges from -0.5 to +0.5.

Study of systematic errors

Systematic errors due to the sample selection have been evaluated with the variation cuts method. In Table 4.2 are shown the standard cuts applied to retained events and the cuts used to evaluate the systematic effect on the results. The variation of the total efficiency applying loose cuts is about +60%; applying tight cuts the variation is -70%. The systematic contribution from FV cut is obtained by restricting and expanding the cut on $\cos\theta_K$ and $\cos\theta_\pi$. Another effect derives from the uncertainty on K^0_S mass, which

variable	standard	loose	tight
$\lvert m_{\pi\pi} - M_K \rvert$	< 2 MeV	< 2.2 MeV	-
$\cos\theta_{12}$	< -0.87	< -0.86	< -0.88
$\cos\theta_1 + \cos\theta_2$	$\in (-0.3, 0.3)$	-	$\in (-0.4, 0.4)$
$\cos\theta_1 + \cos\theta_K$	$\in (-1, 1)$	$\in (-0.8, 0.8)$	$\in (-1.2, 1.2)$
$\theta^\perp_{12}$ (rad)	> 2.6	> 2.5	> 2.7
$\lvert\theta^\perp_{\pi K}\rvert$ (rad)	$\in (0.5, 2.2)$	-	$\in (0.6, 2.0)$

Table 4.2: Applied selection cuts (standard) and range used to evaluate systematic effects.

source	absolute value (ps)
selection cuts	0.062
FV cut	0.009
kaon mass	0.004
fit range	0.035

Table 4.3: Contributions to the systematic error.

directly translates (see Eq.4.3) on the proper time measurement. The last contribution derives from the used fit range. In Table 4.3 the systematic contributions from the different sources are summarized.

4.5.4 Results

The preliminary KLOE result for the K^0_S lifetime is the one coming from this analysis; it has been presented at HEP 2009 (The 2009 Europhysics Conference on High Energy Physics) [Dreu09]:

$$\tau_{K^0_S} = (89.56 \pm 0.03_{\rm stat} \pm 0.07_{\rm syst})\,{\rm ps} \tag{4.9}$$

consistent with the most precise recent measurements by KTEV and NA48, presented in Chapter 1. This is the third best individual measurement in the literature.

The systematic error, evaluated in [Dreu09] as $\pm 0.07_{\rm syst}$ ps (see Table 4.3), has been been recently shown to be reducible to 0.04-0.05 [KLOE10b]. The final result will probably become the first or the second best measurement in the literature. The final result in under the assessment of the KLOE Collaboration.

The statistical error is consistent with what expected from equation (4.1), which would give, for the total sample of about 17.8 million events left after the selection cuts and a fit range up to 6 proper lifetimes, an expected relative statistical error of 2.5×10^{-4}. The actual statistical error is a bit larger (3.3×10^{-4}) since the analytical formula does not take into account the statistical errors from the fit (and, to a smaller extent, contaminations). The analysis has been performed also on the 2005 data ($\sim$2.5 times the 2004 statistics), without evaluating for the moment the systematic errors. The K^0_S lifetime result is consistent.

4.6 A test of the isotropy of the Universe

As referred in Chapter 3, many experiments performed up to now using particle lifetimes give evidence for time dilation. These experimental verifications do not rule out that the lifetime of the particles depends on their direction of motion.

The search for possible anisotropies is performed examining the values of K_S^0 mean lifetime in different directions in a frame of reference fixed to the solar system. This methods is analogous of that adopted by Alessandro De Angelis and Barbara Smalska. This technique uses the fact that collider detectors with 4π acceptances can be used as a probe for detecting asymmetries in the Universe. The rotation of the Earth provides in the different seasons and hours of the day different orientations of the symmetry axes with respect to arbitrary directions that allow averaging detector effects. The electron-positron collider chosen is DAΦNE located at the Laboratori Nazionali di Frascati of INFN, at 41.8238 degree latitude and 12.6725 degree longitude in the geographic coordinate system.

Due to the rotation of the Earth, every about 86,400 s the KLOE detector makes a complete rotation as seen from the Sun. The yearly revolution around the Sun causes the rotational period to be about 86,164.09 s with respect to the fixed stars (sidereal day).

For this analysis a larger sample of decays than considered to determine the K_S^0 lifetime is used, corresponding to both the data from the 2004 runs and from the 2005 runs.

The velocity of the Sun with respect to the CMB rest frame is of 369 ± 2 km/s toward $(l, b) = (263.86°, 48.24°)$. In the earths frame, the CMB is moving toward the earth from that direction: so first it is interesting to study the measurement of K_S^0 mean life for in a cone lying along that direction.

Let v be the speed (unless otherwise specified, units $c = 1$ will be used throughout) of a particle in a system Σ moving with speed V with respect to this hypothetical ether. The speed $\tilde{v}$ of the same particle seen by will be

$$\tilde{v} = \frac{\sqrt{v^2 + V^2 + 2vV\cos\alpha - v^2V^2\sin^2\alpha}}{1 + vV\cos\alpha} \tag{4.10}$$

where α is the angle between the particle momentum in Σ and the absolute velocity of the frame with respect to the ether. If the decay process is absolute, and driven by Σ^0, the lifetime τ of the particle will be dilated by a factor

$$\gamma' = \gamma\Gamma(1 + vV\cos\alpha) \tag{4.11}$$

where $\gamma \equiv \sqrt{1-v^2}$ and $\Gamma \equiv \sqrt{1-V^2}$. Thus, averaging along α, $\gamma' = \gamma\Gamma$. In any lifetime measurement averaging particles with random directions, the observers in the frame will verify the Lorentz transformation, because they will think that the lifetime of the particle $\tau' = \Gamma\tau$. In the following, the ether defined in this paragraph will be called *Lorentzian ether* .

The average difference (asymmetry) between the lifetimes of particles parallel and antiparallel to the direction of motion must be

$$\frac{\Delta\tau}{\tau} = -\frac{1}{2}\int_0^1 2vV\cos\alpha \; d\cos\alpha = \frac{vV}{2}. \tag{4.12}$$

The equation obtained accomplishing the integration on a cone around the direction sampled is:

$$\frac{\Delta\tau}{\tau} = -\frac{1}{2}\int_{\cos\alpha_0}^1 2vV\cos\alpha \; d\cos\alpha = \frac{vV}{2}(1+\cos\alpha_0). \tag{4.13}$$

The sensitivity for the determination of v with respect to $\cos\alpha_0$ was determined to be maximum around $\cos\alpha_0 = 0.5$. The investigation of anisotropy of the Universe reported in this work is based on the search for difference in lifetimes of particles according to their direction.

4.6.1 Data analysis

In the search for anisotropy of time dilation, the same sample of selected K^0_S as described in the previous section was used. The procedure followed in searching the possible asymmetry in the measurement of the K^0_S mean life can be summarized as follows:

1. the proper lifetime has been calculated event per event transforming the directions of the K^0_S decay in the galactic frame;

2. the population of events has been selected for the specified galactic directions;

3. the fit has been performed.

Then the asymmetry in the lifetime of the in the positive and negative directions with respect to an arbitrary axis in the fixed frame has been explored.

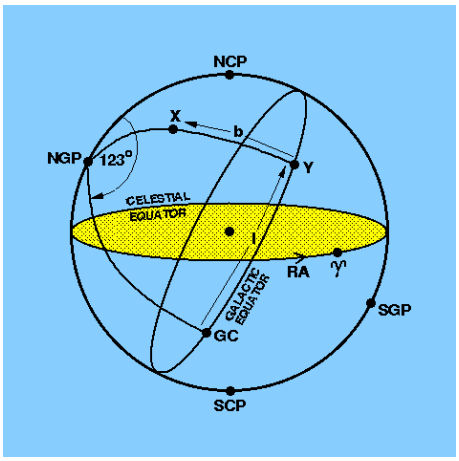

Figure 4.22: Galactic coordinates.

4.6.2 K^0_S coordinates in a frame fixed to the Milky Way

The algorithms used are sketched in Appendix A.

First the directions of the K^0_S were expressed in a frame of reference centered on the Earth and aligned with the apparent center of the Milk Way[2]. The zero-point of galactic longitude is in the direction of the Galactic Centre (GC), in the Sagittarius [ReBr04].

The system of galactic coordinates used in this article is a spherical polar coordinate system centered on the Earth[3], referenced to the Milky Way. The galactic longitude, l, is measured counterclockwise as seen from the North galactic pole and runs from 0° to 360° starting from the line joining the Earth and the GC. The galactic latitude, b, is the angle above or below the galactic equator, which is coincident with the plane of the Milky Way. b runs from +90 to -90 degrees, with positive angles in the Northern hemisphere and negative angles in the Southern hemisphere.

In order to get the equatorial coordinates (EQC), from which the galactic coordinates (GLC) are easily derived, it is useful to make use of an intermediate reference frame, KRF', obtained from KRF with a simple anti-clockwise θ_0 rotation around the Y axis, making in this way the $Y'Z'$ plane coincident with the Frascati-KLOE EarthSun meridian and X' perpendicular to it (of course $Y \equiv Y'$).

[2]It is defined precisely by taking the galactic longitude of the north celestial pole to be 122.932°. This will be called the galactic frame in the following.

[3]In other articles a similar system centered on the Sun is used.

A generic momentum $\vec{p} = (p_x, p_y, p_z)$, passing from KRF to KRF', is then transformed according to the relations :

$$\begin{cases} p'_x = p_x \ \cos\theta_0 - p_z \ \sin\theta_0 \\ p'_y = p_y \\ p'_z = p_x \ \sin\theta_0 + p_z \ \cos\theta_0 \end{cases} . \tag{4.14}$$

4.6.3 Search for possible asymmetries with respect to directions fixed to the Milky Way

A possible difference in the lifetime of the K^0_S in the positive and negative directions with respect to special axes in the Galactic frame was explored. The quantity that has to be measured is is

$$A_{\vec{u}} = \frac{\tau_+ - \tau_-}{\tau_+ + \tau_-} , \tag{4.15}$$

where τ_+ is the apparent lifetime of particles along the positive direction of a generic $\vec{u}$ axis, and τ_- is the apparent lifetime of particles along the negative direction.
As directions for the test, two different directions (and a pair of directions normal to each of them) where studied:

1. The direction of the motion of the Solar System with respect to the CMB system [PDG08], $\vec{V}_{CMB}$:

   $$(l_{CMB}, b_{CMB}) = (l_1, b_1) = (263.86^\circ, 48.24^\circ) .$$

   As a cross check, a pair of directions perpendicular to it was studied: $(l_2, b_2) = (173.86^\circ, 0^\circ)$, $(l_3, b_3) = (263.86^\circ, -41.76^\circ)$.

2. The so-called "absolute direction" [Cah04] corresponding to $\alpha = 5.2^{hr}, \delta = -67^0$, i.e. $\vec{V}_{ABS}$:

   $$(l_{ABS}, b_{ABS}) = (l_1, b_1) = (277.46^\circ, -34.47^\circ) .$$

   As a cross check, a pair of directions perpendicular to it was studied: $(l_{2'}, b_{2'}) = (173.86^\circ, 0^\circ)$, $(l_{3'}, b_{3'}) = (263.86^\circ, -41.76^\circ)$.

For each axis, a cone was selected such that the K^0_S direction formed an angle ϑ smaller than 30 degrees with the axis itself. Monte Carlo studies [DeSm96] demonstrated that this

criterion maximizes the sensitivity to asymmetries. The relation between the measured asymmetry in a cone and the asymmetry with respect to a fixed a direction is, in case of uniform population (which is a good approximation for the data set):

$$A_{\vec{u}} = \frac{A_{cone}}{< \cos\vartheta >_{cone}} \simeq 1.072 A_{cone} \,. \tag{4.16}$$

4.6.4 Fit to proper time distribution in the galactic plane

The average lifetime for the population of K_S^0 with direction of the momentum vector that belongs to a given cone for each cone was determined with the same procedure used in the previous section. Fit parameters are the lifetime $\tau_{K_S^0}$ and the parameters describing the two-gaussian resolution used to convolute the exponential decay function. The fits were performed in a region of proper time between $-0.5\tau_{K_S^0}$ and $6.5\tau_{K_S^0}$ in which the fit function was proven to give a reasonable description of the data (χ^2 per degree of freedom smaller than 3). Bins at the border are discarded if the number of entries is below 30.
The efficiency $\varepsilon(j)$ is calculated on the basis of the efficiency assigned to each event. The momentum of K_S^0 calculated in the galactic frame depends of course on the flight direction of the K_S^0 but also on the sidereal time. So the population of K_S^0 of each cone in the galactic plane comes from events that can be reconstructed in different zones of the detector for different sidereal time with assigned quite different efficiency. The proper time distribution is fitted with a convolution of an exponential and the efficiency function.

4.6.5 Results

The systematic errors largely cancel in a difference between lifetimes; the errors used are thus just the statistical ones. The results are:

1. For the motion with respect to the CMB system:

$$A_{cone,1} = \frac{\tau_+ - \tau_-}{\tau_+ + \tau_-} = (-1.3 \pm 4.0) \times 10^{-4} \tag{4.17}$$

with central values of $\tau_+ = (89.59 \pm 0.11)$ ps and $\tau_- = (89.43 \pm 0.11)$ ps, and $\chi^2/n.d.f.$ of 1.3 and 1.6 respectively for the 2004 sample; $\tau_+ = (89.58 \pm 0.06)$ ps and $\tau_- = (89.65 \pm 0.05)$ ps, and $\chi^2/n.d.f.$ of 2.1 and 2.6 respectively for the 2005 sample. As a comparison, the tests in two directions perpendicular to $\vec{V}_{CMB}$ gave $A_{cone,2} = (-3 \pm 3) \times 10^{-4}$ and $A_{cone,3} = (-5 \pm 3) \times 10^{-4}$.

2. For the test with respect to the direction of $\vec{V}_{abs}$:

$$A_{cone,1'} = \frac{\tau_+ - \tau_-}{\tau_+ + \tau_-} = (-1 \pm 3) \times 10^{-4} \,. \tag{4.18}$$

As a comparison, the tests in two directions perpendicular to $\vec{V}_{abs}$ gave $A_{cone,2'} = (2 \pm 4) \times 10^{-4}$ and $A_{cone,3'} = (-2 \pm 3) \times 10^{-4}$.

Translated by the use of Eq. (4.16) into a result with respect to $\vec{V}_{CMB}$, Eq. (4.17) gives:

$$A_{\vec{V}_{CMB}} = (-1.4 \pm 4.3) \times 10^{-4} \,. \tag{4.19}$$

This translates into upper limits at 95% confidence level (CL):

$$|A|_{\vec{V}_{CMB}} \quad < \quad 9.8 \times 10^{-4} \,. \tag{4.20}$$

4.6.6 Interpretation of the results

Being the velocity of the Solar System with respect to the CMB system of about $(12 \times 10^{-4})c$ [PDG08], one would expect, in a naive model in which time dilation is physically meaningful when computed with respect to the CMB frame, that K^0_S traveling at a speed of $v_K \simeq 0.21c$ (the average velocity in the sample) with respect to the Solar System would display an asymmetry in lifetime of

$$A_{ether} \simeq \frac{1}{2} \left(\frac{1}{\sqrt{1 - \frac{(v_K + V_{CMS})^2}{c^2}}} - \frac{1}{\sqrt{1 - \frac{(v_K - V_{CMS})^2}{c^2}}} \right) \simeq 27 \times 10^{-4} \,.$$

The result in Eq. (4.20) rules out this hypothesis.

The upper limit $|A| < 9.8 \times 10^{-4}$ is the best limit on asymmetry of lifetimes ever published. However, it is far from being sensitive enough to test models in which a possible anisotropy is induced by the interaction with a standard QED vacuum (being the expected refractive index [EuKo35] different with respect to 1 by some 10^{-8}).

4.7 Conclusion

In this work a direct measurement of the K^0_S lifetime has been performed; although preliminary, it is among the three most precise in the literature.

A direct search for asymmetries in time dilation has been performed with respect to the direction of motion of the solar system with respect to the CMB. Although the preliminary result is negative, this test is the most sensitive direct test in the literature.

5

Appendix A

5.1 Coordinate systems

This appendix reviews the seven coordinate systems used in the spin analysis, and gives the relevant transformations between them.

5.1.1 Geocentric Equatorial Coordinates

The *Geocentric Equatorial Coordinates (GEI)*, also called Celestial Coordinates, are a spherical polar coordinate system that have the centre represented by the earth and the equatorial plane called celestial equator. The equatorial coordinates system has its X-axis pointing from the Earth towards the first point of Aries, the vernal point γ (the position of the Sun at the vernal equinox), so each movement of this plane with respect to the fixed stars will result in a time variation of the coordinates. This direction is the intersection of the Earth's equatorial plane and the ecliptic plane and thus the X-axis lies in both planes. The Z-axis is parallel to the rotation axis of the Earth and Y completes the right-handed orthogonal set ($Y = Z \times X$). The Equatorial coordinates are measured in Right Ascension (RA; α), which is the equivalent of geographic longitude, and runs from 0° to 360° counterclockwise around the earths rotation axis. Right Ascension is also measured in units of time. Declination, δ, is the angle above or below the earths equator, runs from +90°to -90°, with positive angles in the northern hemisphere and negative angles in the southern hemisphere.

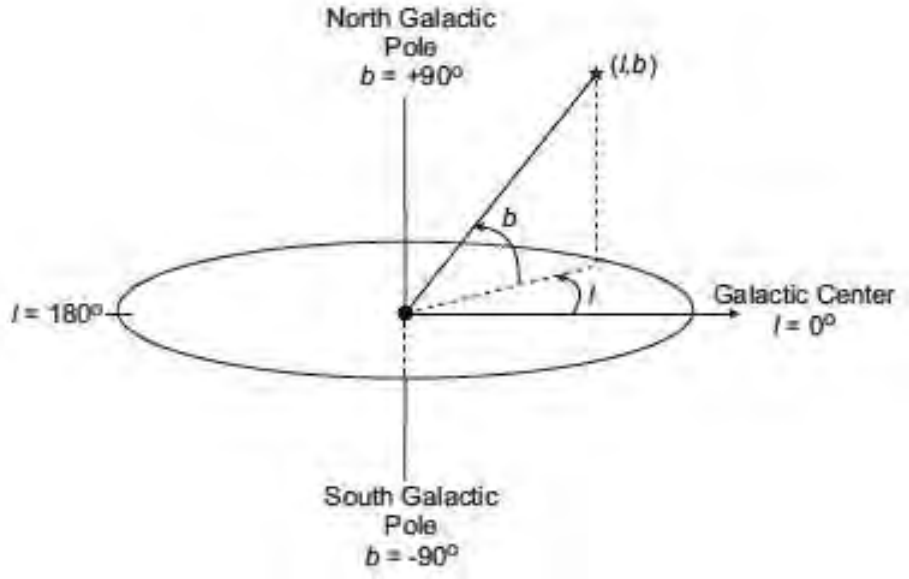

Figure 5.1: The Galactic Coordinate System.

5.1.2 Galactic Coordinates

The Galactic coordinate system (Fig. 5.1) is a spherical polar coordinate system that has as reference the Milky Way galaxy plane. The first system was defined in 1932 using optical observations of the Milky Way Galaxy. Galactic longitude, l, is measured counterclockwise as seen from the north galactic pole and runs from 0°to 360 °starting from the line joining the earth (or sun) and the galactic center. Galactic latitude, b, is the angle above or below the galactic equator, which is coincident with the plane of the Milky Way galaxy. b runs from +90°to -90°, with positive angles in the northern hemisphere and negative angles in the southern one. In this thesis, galactic coordinates centered on the earth are used. The Particle Data Groups value for the earths velocity vector is given in galactic coordinates.

5.2 The KLOE detector reference frame

In Fig. 5.2 the KLOE detector and the KLOE reference system (KRS) are shown: the Z axis is the beam axis, forming an angle of $\theta_0 = 57.8$ deg with the Frascati meridian, Y is the vertical axis and the X axis, perpendicular to the previous ones, points in the direction opposite respect to the DAΦNE hall center. The components of a momentum

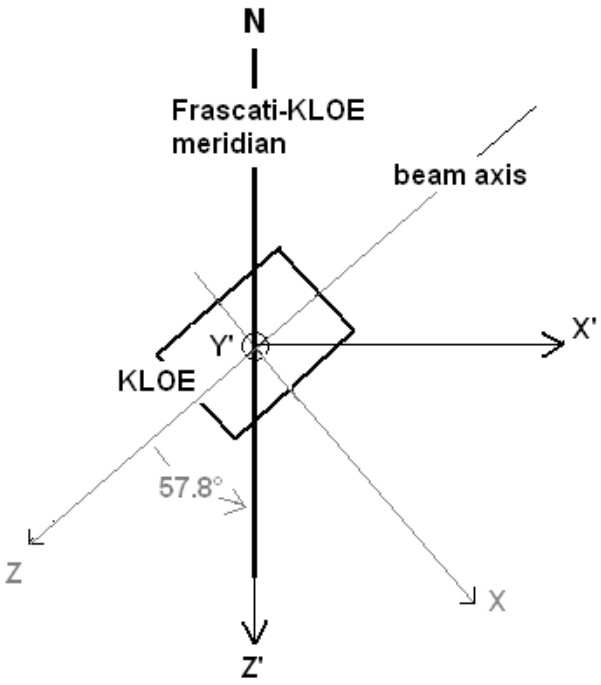

Figure 5.2: The intermediate KLOE reference system, KRS', obtained with a simple rotation from KLOE reference system, KRS.

$\vec{p} = (p_x, p_y, p_z)$ are usually referred to this reference system. In order to get the equatorial coordinates (EQC), from which the galactic coordinates (GLC) are easily derived, is useful to make use of an intermediate reference system, KRS', obtained from KRS with a simple anti-clock wise θ_0 rotation around the Y axis, making in this way the $Y'Z'$ plane coincident with the Frascati-KLOE earth meridian and X' perpendicular to it (of course $Y \equiv Y'$). A generic momentum $\vec{p} = (p_x, p_y, p_z)$, passing from KRS to KRS', is then transformed according to the relations:

$$\begin{cases} p'_x = p_x \ \cos\theta_0 - p_z \ \sin\theta_0 \\ p'_y = p_y \\ p'_z = p_x \ \sin\theta_0 + p_z \ \cos\theta_0 \end{cases} . \tag{5.1}$$

5.3 The equatorial coordinates

The EQC assumes as equatorial plane that containing the earth equatorial plane. The right ascension (RA) is similar to the earth longitude: it is measured in degrees, from 0° to 360° or, which is the same, from 0^h to 24^h. In this last case is referred to it as the sidereal time. The RA angle (Fig.5.3) is computed starting from the semi-axis intersecting

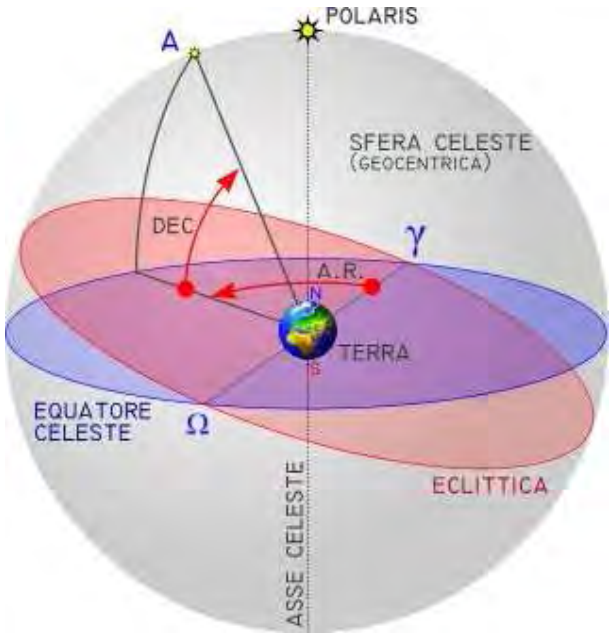

Figure 5.3: The equatorial coordinates.

equatorial and ecliptic planes, directed toward the γ point, being positive a rotation in West-East direction. The γ or *vernal* point is the point where the sun rises on march, 21^{th}. Also the declination δ is similar to the earth latitude, defined as the angle with the equatorial plane, from $-90°$ to $+90°$.

In order to evaluate the right ascension RA and declination δ it has been first calculated the coordinates of the versors $\hat{N}$ and $\hat{O}$ in KRS': (Fig. 5.4). The result is

$$\begin{cases} n_1 = 0 \\ n_2 = +\cos(90 - \lambda) \\ n_3 = -\sin(90 - \lambda) \end{cases} \tag{5.2}$$

and

$$\begin{cases} o_1 = 0 \\ o_2 = +\cos\lambda \\ o_3 = +\sin\lambda \end{cases} \tag{5.3}$$

where $\lambda = 41.823\,8^\circ$ is the Frascati-KLOE latitude. The $\hat{N}$ versor points toward the north celestial pole, while the $\hat{E}$ versor, entering the plane of the figure, has the same direction of X' axis. Working in KRS' reference, it is possible to obtain the declination starting

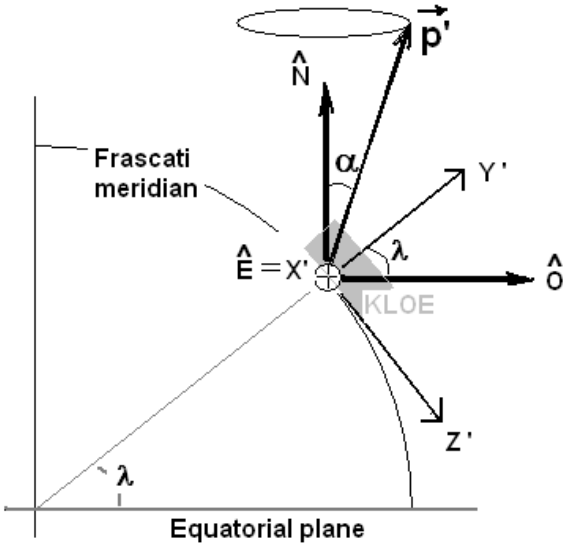

Figure 5.4: Meridian plane view. $\hat{N}$, $\hat{O}$, Y' and Z' lay on the meridian plane. λ is the Frascati-KLOE latitude.

from the angle α between the transformed vector $\vec{p}\,'$ and the $\hat{N}$ versor:

$$\begin{cases} \alpha = \cos^{-1}\left(\frac{\vec{p}\,'\cdot\hat{N}}{|\vec{p}\,'|}\right) \\ \delta = 90^\circ - \alpha \end{cases} \tag{5.4}$$

Fig.5.5 shows a section parallel to the equatorial plane: the RA coordinate is the sum of RA_1, contribution from Frascati-KLOE meridian and ϕ, the angle which the projection of momentum $\vec{p}\,'$ on the equatorial plane forms with the meridian plane. Once obtained the $\vec{p}\,'$ component with respect to $\hat{O}$ and $\hat{E}$ versors, i.e., $p_O = \vec{p}\,' \cdot \hat{O}$ and $p_E = \vec{p}\,' \cdot \hat{E}$, the ϕ

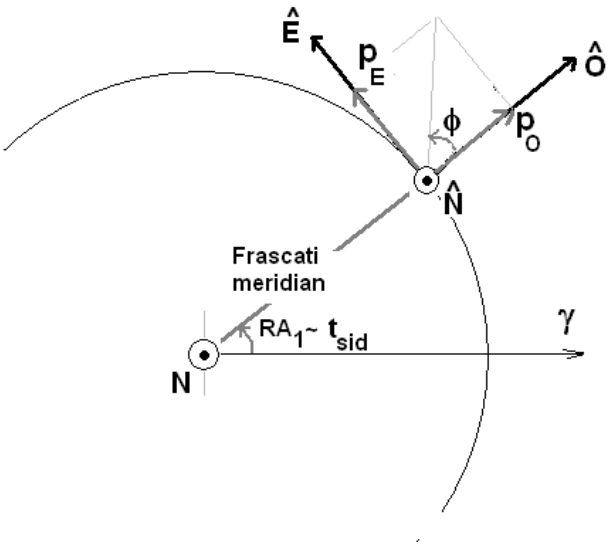

Figure 5.5: Equatorial plane view. RA is obtained adding RA_1 and ϕ.

angle is:

$$\phi = \tan^{-1}(p_O, p_E) \tag{5.5}$$

where $\tan^{-1}(x, y)$ ranges from 0 to 2π. The RA_1 contribution, coming from the Frascati-KLOE meridian, is the **sidereal time**, obtained starting from local longitude and time (see next section). Adding the two terms gives

$$RA = RA_1 + RA_2 = 360^\circ \; t_{sid} + \phi \tag{5.6}$$

where t_{sid}, the sidereal time in daily fraction, ranges from 0 to 1.

5.4 Sidereal time evaluation

The sidereal time is computed considering the earth motion related with fixed stars. In fact, due to the revolution motion, the solar day is longer than the sidereal day by an amount of almost 4 min/day.

The currently adopted expression for the relationship between universal time, UT, and the observed Greenwich Mean Sidereal Time, t^G_{sid}, *i.e*, $GMST$ of 0^h UT is [AK82]

$$t^G_{sid} = 24\,110.548\,41 + 8\,640\,184.812\,866\; T + 0.093\,104\; T^2 - 6.2\; 10^{-6}\; T^3 \tag{5.7}$$

where t^G_{sid} is expressed in seconds and T is the number of Julian centuries of universal time elapsed since Julian day number JD0 = 2 451 545.0 UT (2000 January 1, 12^h UT):

$$T = \frac{JDN - 2\,451\,545}{36\,525}\,. \tag{5.8}$$

Julian day number computation is described in the appendix. We must now relate local time into Greenwich time, taking into account for the local time zone, tz:

$$t^G = t^{LOC} - tz\,. \tag{5.9}$$

Passing from solar to sidereal time requires a factor conversion, $\eta = 1.002\,737\,909\,3$. In fact, due to the earth revolution, a sidereal interval of time is longer than the corresponding solar interval of time:

$$\langle \Delta t_{sid} \rangle = \langle \Delta t_{sun} \rangle \left(1 + \frac{1}{365.2422}\right) = \langle \Delta t_{sun} \rangle\, \eta\,. \tag{5.10}$$

The formula for sidereal time to be used in Eq.5.6 is then

$$t_{sid} = \eta\; t^G + t^G_{sid} + \frac{L}{360} \tag{5.11}$$

representing the mean sidereal time of Frascati-KLOE meridian. Greenwich time, t^G and t^G_{sid} are both in daily fraction. L is the Frascati-KLOE longitude, i.e., $L = +12.6725^\circ$.

5.5 Moving to galactic coordinates

The galactic coordinate system is a celestial coordinate system which is centered on the Sun and is aligned with the apparent center of the Milk Way Galaxy. Galactic longitude, ℓ, is analogous to RA and is measured along the galactic equator in the same direction as RA. The zero-point of galactic longitude is in the direction of the Galactic Centre (GC), in the constellation of Sagittarius [ReBr04]. It is defined precisely by taking the galactic longitude of the north celestial pole to be exactly 122.932°. The galactic longitude of the star X in Fig. 5.6 is given by the angle between GC and Y. Once evaluating EQC it is possible to obtain the **galactic coordinates** (GLC) because passing from one system to the other requires a fixed spherical angle rotation. The following formulae relate Galactic

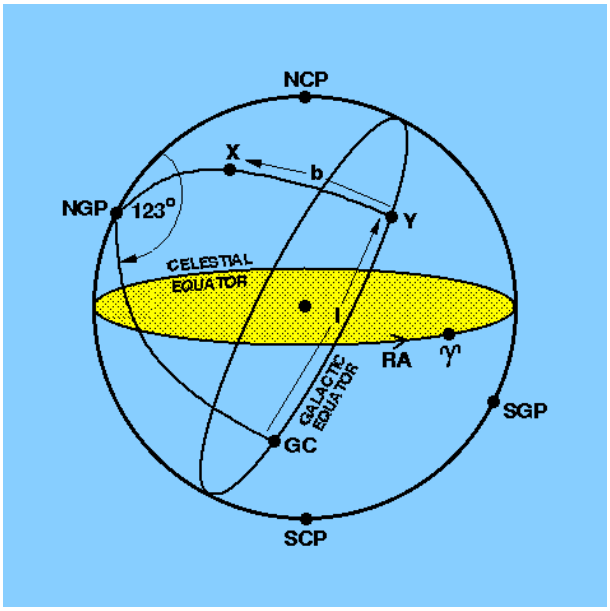

Figure 5.6: Galactic coordinates

latitude b and longitude ℓ to the declination δ and right ascension RA [Buf89]:

$$\begin{cases} b = \sin^{-1}\left[\cos\delta\cos\delta_{NGP}\cos(RA - RA_{NGP}) + \sin\delta\sin\delta_{NGP}\right] \\ \ell = \tan^{-1}(A, B) + \ell_{ascend} \\ \text{where} \\ A = \sin\delta\cos\delta_{NGP} - \cos\delta\cos(RA - RA_{NGP})\sin\delta_{NGP} \\ B = \cos\delta\sin(RA - RA_{NGP}) \end{cases} \tag{5.12}$$

$\tan^{-1}(x, y)$ ranges from 0 to 2π, RA_{NGP}=192.859 5° and δ_{NGP}= 27.128 3° are, respectively, the right ascension and the declination (epoch J2000) of the north galactic pole and ℓ=33° is the longitude of the ascending node of the galactic plane on equator.

5.6 Fortran code source to evaluate the sidereal time

The following is an example of Fortran code to evaluate sidereal time.

```
      Subroutine Temposid(tloc,G,M,A,tsid)
c ---------------------------------------------
c      Ref: S.Akoi et al., Astron.Astrophys. 105, 359-361 (1982)
c      tloc = decimal local time; tsid = local sidereal time
c      fuso account legal hour
c      A = year, M = month, G = day
c      (Frascati-KLOE: 12^40'21,1")

      Real tloc,tsid,ora
      real A,M,G,fuso,GG,longit
      Integer sec,b,c,d
      Double precision T,T3
      parameter (long=12.6725)

      fuso = +1
      if(M.ge.4.AND.M.le.9) fuso = +2

      if (A.eq.2001) then
         if(M.eq.3.and.G.eq.25.and.tloc.ge.2) fuso=+2
         if(M.eq.3.and.G.gt.25) fuso=+2
         if(M.eq.10.and.G.lt.28) fuso=+2
         if(M.eq.10.and.G.eq.28.and.tloc.lt.3) fuso=+2
      endif

      if (A.eq.2002) then
         if(M.eq.3.and.G.eq.31.and.tloc.ge.2) fuso=+2
         if(M.eq.3.and.G.gt.31) fuso=+2
         if(M.eq.10.and.G.lt.27) fuso=+2
         if(M.eq.10.and.G.eq.27.and.tloc.lt.3) fuso=+2
      endif

      if (A.eq.2004) then
         if(M.eq.3.and.G.eq.28.and.tloc.ge.2) fuso=+2
         if(M.eq.3.and.G.gt.28) fuso=+2
         if(M.eq.10.and.G.lt.31) fuso=+2
```

```
      if(M.eq.10.and.G.eq.31.and.tloc.lt.3) fuso=+2
    endif

    if (A.eq.2005) then
      if(M.eq.3.and.G.eq.27.and.tloc.ge.2) fuso=+2
      if(M.eq.3.and.G.gt.27) fuso=+2
      if(M.eq.10.and.G.lt.30) fuso=+2
      if(M.eq.10.and.G.eq.30.and.tloc.lt.3) fuso=+2
    endif

    if (M.eq.1.or.M.eq.2) then
      A=A-1
      M=M+12
    endif

    sec = int(A/100)
    b = 2-sec+int(sec/4.)
    c = int(365.25*A)
    d = int(30.6001*(M+1))
   GG = b+c+d+G+1720994.5
    ora = 1.0027379093*(tloc-fuso)/24.
    longit=long/360.
    T = (GG-2451545.)/36525.
    T3 = + 24110.54841
   &     + 8640184.812866*T
   &     + 0.093104*T**2
   &     - 6.2D-6*T**3
    T3 = T3/86400.
    tsid = ora + longit + sngl(T3)
    tsid = tsid - int(tsid)
    if (tsid.lt.0) tsid=tsid+1
    tsid=24.*tsid

    return
    end
```

Second Part

Abstract

Ground-based gamma-ray astronomy is part of a field of fundamental research called Astroparticle Physics; spectacular discoveries were recently done in this field. Most such discoveries have been made thanks to Imaging Air Cherenkov Telescopes (IACT), which allow one to detect Cherenkov light from extended air showers initiated by cosmic gamma-rays and charged cosmic particles.

The MAGIC telescope is a new generation IACT located at La Palma, Canary Islands, Spain. Composed by two reflectors with 17 m diameter each, MAGIC has the largest optical surface in the world, and it has the lowest threshold energy (25 GeV). MAGIC started operations in 2004 in the single-detector configuration, and in 2009 as a stereo detector. Since then, it has discovered many new sources and classes of sources, both galactic and extragalactic.

Large data volumes (up to 1 TByte for a single telescope) are collected every night; the trigger rate is about 300 Hz in normal conditions, but it can increase in special data acquisition modes. To deal with the large storage requirements, a cluster of computers with concurrent access to the same shared storage units, based on the distributed file system GFS, has been installed. The system can handle a sustained data acquisition (DAQ) write rate above 1.2 kHz for MAGIC-I, and it allows other nodes to perform concurrent access to the data on the shared storage units. Various simultaneous tasks can be used at any time, in parallel with data taking, including data compression, tape recording, calibration, on-line analysis. The system is designed to quickly recover after the failure of one node in the cluster and to be easily extended as more nodes or storage units can be required in the future.

In this second part the main results of MAGIC are described, and the DAQ system, to which I contributed, is described.

1

Recent results from MAGIC

1.1 Introduction

The Major Atmospheric Gamma Imaging Cherenkov (MAGIC) telescope is a last generation instrument for very high energy (VHE, in the energy region > 30 GeV [DAMaPe08])γ ray observation exploiting the Imaging Air Cherenkov technique. This kind of instrument images the Cherenkov light produced in the particle cascade initiated by a particle hitting the atmosphere [DAMaPe08].

MAGIC (Fig. 1.1) is composed by two 17 m. diameter telescopes located on the Roque de los Muchachos Observatory, in La Palma (Spain), and it is thus the largest optical reflector in the world. MAGIC incorporates a number of technological improvements in its design and achieves the lowest energy threshold (55 GeV with the standard trigger, 25 GeV with a special trigger, activated in particular conditions) among instruments of its kind. The signal digitization utilizes 2GSample/s Flash ADCs.

Figure 1.1: The MAGIC telescopes.

The sensitivity for a single telescope is such that, at a flux peak energy of 300 GeV, a source as faint as of 1.6% of the Crab Nebula can be detected at 5σ in 50 hours of observations. The relative energy resolution above 200 GeV is below 25%; the angular resolution is about 0.1 degrees. MAGIC is also unique among Cherenkov telescopes by its capability to operate under moderate illumination (i.e., moon or twilight); this allows to increase the duty cycle.

Operating as a single telescope since 2004, MAGIC has started stereo observations at end 2009, with the basic parameters summarized in the following Table (in comparison with the other large gamma experiments, H.E.S.S. in Namibia and VERITAS in Arizona).

Instrument	Tels.	Area Tel. (m^2)	Field of View (°)	Area Total (m^2)	Thresh. (TeV)	Angular res. (°)	Sensitivity (% Crab)
H.E.S.S.	4	107	5	428	0.1	0.06	0.7
MAGIC	2	236	3.5	472	0.05	0.08	0.8
VERITAS	4	106	4	424	0.1	0.07	0.7

MAGIC has developed a physics program which includes topics of both fundamental physics and astrophysics. In the following sections are illustrated some of the MAGIC latest contributions to Galactic and extragalactic astrophysics and the technical aspects of the data acquisition system related to the storage and distribution of a huge quantity of data.

1.2 Highlights on Galactic observations

In this section the latest MAGIC results on Galactic astrophysics are reviewed.

MAGIC has discovered 4 new Galactic sources at VHE: the supernova remnant MAGIC J0616+225 [MAG07a], consistent with IC443; the first binary periodic source, LSI+61 303 [MAG06a]; Cygnus X-1 [MAG07b]; the pulsar from Crab [MAG08a]. They are all likely to indicate new classes of emitters. For some 20 other Galactic sources MAGIC has confirmed the discovery, performing flux and morphology measurements. Finally, MAGIC has published significant flux upper limits for interesting classes of sources, like, e.g., Wolf-Rayet binaries.

1.2.1 Shell-type Supernova Remnants: Cassiopeia A and MAGIC J0616+225

MAGIC observed the shell-type supernova remnant (SNR) Cassiopeia A during 47 good-quality hours and detected a point-like source of VHEγ-rays above $\sim$250GeV [MAG07c]. The measured spectrum is consistent with a power law with a differential flux at 1 TeV of $(1.0\pm0.1_{stat}\pm0.3_{sys})\times10^{-12}$ TeV^{-1}cm^{-1}s^{-1} and a spectral index of Γ=2.4$\pm$0.2$_{stat}\pm$0.2$_{sys}$. The spectrum measured by MAGIC is consistent with that measured by HEGRA [HEG01] 8 years before for the energies above 1 TeV, i.e., where the two measurements overlap. The MAGIC results favor a hadronic scenario for the γ-ray production, since a leptonic origin of the TeV emission would require low magnetic field intensities, which are difficult to reconcile with the high values required to explain the rest of the broad-band spectrum. In addition, MAGIC has discovered a new source of VHE γ-rays located close to the Galactic plane, which has been called MAGIC J0616+225 [MAG07a]; this source is spatially coincident with the SNR IC 443. The measured energy (E) spectrum is well fitted by the power law: $\frac{dN}{dEdAdt} = (1.0 \pm 0.2) \times 10^{-11}(E/0.4 \text{ TeV})^{-3.1\pm0.3}$ TeV^{-1}cm^{-2}s^{-1}. MAGIC J0616+225 is point-like for the MAGIC spatial resolution, and appears to be displaced from the center of the SNR shell. The observed VHE radiation may be due to π^0 decays from the interaction between cosmic rays accelerated in IC 443 and the dense molecular cloud. A possible distance of this cloud from IC 443 could explain the steepness of the measured VHE γ-ray spectrum.

1.2.2 Compact binaries: Cygnus X-1 and LS I +61 303

Cygnus X-1 is the best established candidate for a stellar mass black-hole and one of the brightest X-ray sources in the sky. MAGIC has observed it for 40 hours along 26 different nights between June and November 2006. The MAGIC observations obtained a very strong evidence (4.1 σ post-trial significance) of a short-lived, intense flaring episode during 24th September 2006, in coincidence with a historically high flux observed in X-rays. The detected signal is point-like. The energy spectrum fits well extrapolations from Integral.

LS I +61 303 is a binary system containing a main-sequence star together with a compact object (neutron star or black hole), which displays periodic emission throughout the spec-

trum from radio to X-ray wavelengths. Observations with MAGIC have determined that this object produces γ-rays up to at least $\sim$4 TeV [MAG06a], and that the emission is periodically modulated by the orbital motion ($P_{\mathrm{TeV}} = (26.8 \pm 0.2)$ d) [MAG09]. The peak of the emission is found at orbital phases around 0.6–0.7. During December 2006 MAGIC detected a secondary peak at phase 0.8–0.9.

In a multiwavelength campaign involving radio (VLBA, e-EVN, MERLIN), X-ray (Chandra) and TeV (MAGIC) observations [MAG08b], a hint of temporal correlation between the X-ray and TeV emissions and evidence for radio/TeV non-correlation were found.

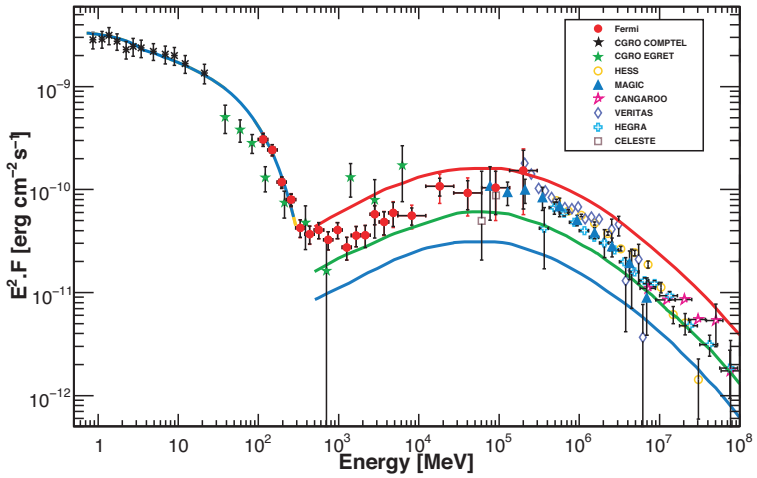

Figure 1.2: Differential flux from the Crab pulsar as measured from different detectors.

The Crab Nebula is a SNR with a pulsar at its center. Crab is the standard candle for VHE astrophysics and as such, a big fraction of the observation time from MAGIC and from the other Cherenkov telescopes is devoted to this object. The VHE source is point-like and its position coincides with that of the pulsar.

Recently, thanks to a special trigger setup, MAGIC has detected pulsed emission coming from the Crab pulsar above 25 GeV, with a statistical significance of 6.4 σ [MAG08a]. This result has revealed a relatively high energy cutoff, indicating that the emission occurs far out in the magnetosphere, hence excluding the polar-cap scenario as a plausible explanation for the high-energy origin. This is also the first time that a pulsed γ-ray emission is detected from a ground-based telescope, and opens the possibility of a detailed study of the pulsar's energy cutoff, which will help elucidate the mechanism of high energy radiation

in these objects.

The non-pulsed emission is also very relevant, and it extends up to some 100 TeV (at the limit of the sensitivity of the Cherenkov telescopes). The particular characteristics of MAGIC allow measuring the Crab energy spectrum in the continuum at low energies, overlapping with the Fermi satellite (Fig. 1.2). This fact can permit cross-calibration [Bast05] among the space-based and ground-based detectors, which will decrease the relative energy uncertainty to some 15% for the latter.

1.3 Highlights on extragalactic observations

MAGIC, the Cherenkov telescope with the lowest energy threshold (and, as a consequence, the largest optical depth), contributed to the discovery of 8 Active Galactic Nuclei: 1ES 1218+304 [MAG06b] at $z = 0.182$, Markarian 180 [MAG06c] at $z = 0.045$, BL Lacertae [MAG07d] at $z = 0.069$, 1ES 1011+496 [MAG07e] at $z = 0.212$, PG 1553+113 [MAG07f] at $z > 0.09$ (co-discovered with H.E.S.S.), S5 0716+71 [Tesh08] at $z = 0.31 \pm 0.08$, MAGIC J0223+430 [MAG09] at unknown redshift, possibly coincident with 3C66B, and last but not least the farthest one, 3C 279 [MAG08c], at the unexpectedly large redshift of $z = 0.54$. MAGIC has studied most of the AGN in its field of view, often detecting new physics features.

One of the main features of the emissions by AGN is variability. Such a variability can be very rapid, of the order of some 10 seconds or so (the typical size of the central black hole can be 100 to 1000 times larger).

In the following sections some of the main results are summarized.

1.3.1 Blazars detected during optical outbursts

Observations triggered by high optical states of potential VHE blazars have proven very successful with the detection of Mkn 180, 1ES 1011+496, 3C 279, and recently S5 0716+71. The observation of 1ES 1011+496 was triggered by an optical outburst in March 2007, resulting in a 6.2 σ detection [MAG07e] of a flux $(1.58 \pm 0.32) \times 10^{-11}\mathrm{cm}^{-2}\mathrm{s}^{-1}$ above 200 GeV. An indication for a long-term optical–VHE correlation is given, in that in spring 2007 the VHE γ-ray flux was $> 40\%$ higher than in spring 2006, when MAGIC had observed

this blazar for the first time without finding a significant signal.

In April 2008, the optical telescope supporting MAGIC, KVA, reported a bright optical state of the blazar S5 0716+71, triggering VHE observations which resulted in a 6.8 σ detection, corresponding to a flux of $F_{>400\mathrm{GeV}} \approx 10^{-11}\mathrm{cm}^{-2}\mathrm{s}^{-1}$. The source was also in a high X-ray state.

1.3.2 Multiwavelength campaigns

For an advanced understanding of AGNs, simultaneous multiwavelength (MW) observations are essential, as they allow the determination of spectral energy distributions (SEDs) spanning over 15 orders of magnitude in energy. MAGIC recently participated in MW campaigns carried out on the blazars Mkn 421, Mkn 501, PG 1553+113, 1ES 1218+304, 1H 1426+428, and on the radio galaxy M 87. These campaigns involved the X-ray satellites INTEGRAL, Suzaku and Swift, the γ-ray telescopes H.E.S.S., VERITAS, and MAGIC, and other optical and radio telescopes.

Among the main results, a 120-hour observational campaign on the giant radio galaxy M87 in spring 2008 detected two major outbursts of gamma-ray emission, while simultaneous high resolution radio observations of the activity of this radio galaxy were performed. The increase of the radio flux could be located from the innermost core of M87, associated with the immediate vicinity of the central black hole. The combined observation pins down the location of activity during the gamma-ray outbursts and thus the site of the particle accelerator. This is the first time that the imaging of a galaxy different from the Milky Way has been performed [HESS09].

1.4 Impact of the MAGIC results on fundamental physics

MAGIC has set upper limits on possible signals from the annihilation of Dark Matter particles in channels involving high-energy photons, for the Galactic Center and for dwarf Spheroidals [LOM09].

The imaging and the study of the SEDs from Galactic objects by MAGIC indicates that Galactic sources (PWN in particular) are likely to generate charged cosmic rays up to some 10^{15} eV.

The two additional subjects investigated thanks to the study of AGN.

1.4.1 Does the speed of light depend on the photon energy?

The constancy of the speed of light, c, is one of the postulates of the theory of relativity; it has been extensively tested in the recent years against a possible dependence on the photon energy E, which is predicted, for example, by theories inspired by Quantum Gravity. At first order, such a dependence is usually parametrized [AC98] as

$$c' = c\,[1 \pm (E/E_{s1})]\ . \tag{1.1}$$

The energy scale E_{s1} which parametrizes the scale of violation of relativity in the above expression is usually expressed in units of the Planck mass, $M_P \simeq 1.22 \times 10^{19}$ GeV.

A favored way to search for such a dispersion relation is to compare the arrival times of photons of different energies arriving on Earth from pulses of distant astrophysical sources. The greatest sensitivities may be expected from sources with short pulses, at large redshifts z, of photons observed over a large range of energies: γ-ray bursts (GRBs) and AGN.

MAGIC [MAG08d] has published the results of the analysis of a giant flare of the Mrk 501 blazar, at $z = 0.034$. A correlation has been observed (with a probability of 2.5% of coming from a statistical fluctuation) between the photon energy and the arrival time. The correlation is *subluminal*, i.e., the minus sign holds in Eq.(1.1) (higher energy photons are delayed) with a coefficient $dt/dE = (0.030 \pm 0.012)$ s/GeV. Later, the Fermi/LAT detector has registered the most energetic photon, at $E \sim 13.2$ GeV, from the GRB080916C [FERMI09a] at z 4.34, 16.5 s after the primary burst. The delays from the GRB080916C are consistent within errors with the same energy scale [Ellis09], although the sources are very different as their distance is.

However, the recent results by Fermi [FERMI09b] do not fit in the exciting picture outlined above. The most conservative conclusion is that before making any statement is necessary to understand better the time/energy correlation of the photon emission at the source. Anyway, it is proved that the sensitivity of Cherenkov telescopes is such that it is possible to detect effects at the Planck mass scale.

1.4.2 Anomalies in the propagation of gamma-rays?

The horizon of the observable Universe is expected to rapidly shrink in the VHE band as the energy increases, due to the scattering of VHE photons off background photons permeating the Universe, which produces electron-positron pairs [FaSte71]. The corresponding cross section $\sigma(\gamma\gamma \rightarrow e^+e^-)$ peaks where the VHE photon energy E and the background photon energy ϵ are related by $\epsilon \simeq (500\,\mathrm{GeV}/E)\,\mathrm{eV}$. Therefore, for observations performed by Cherenkov Telescopes the resulting cosmic opacity is dominated by the interaction with ultraviolet/optical/infrared diffuse background photons, usually called Extragalactic Background Light (EBL), which is produced by galaxies during the whole history of the Universe.

The absorption is usually parametrized as $e^{-\tau(E,z)}$. The mean free path of VHE photons decreases like a power law from the Hubble radius 4.2 Gpc around 100 GeV to 1 Mpc around 100 TeV [CoAh97]. Thus, the observed flux is exponentially suppressed both at high energy and at large distances, so that sufficiently far away sources become hardly visible in the VHE range and their observed spectrum should be steeper than the emitted one.

Observations have not detected such a behavior. Strong evidence comes from the observation of 3C279, which would be expected to be attenuated by a factor e^{-3} at the maximum energies detected of about 400 GeV. Another evidence comes from the fact that one does not observe a steepening of the SED of blazars with increasing distances [DARMa07].

A possible explanation [DARMa07] requires that photons oscillate into a new Axion-Like Particle (ALP) and vice-versa in the presence of cosmic magnetic fields (the so-called "DaRMa scenario"); once ALPs are produced close enough to the source, they travel unimpeded throughout the Universe and can convert back to photons before reaching the Earth. Since ALPs do not undergo EBL absorption, the effective photon mean free path is increased. An ALP of mass $\ll 10^{-10}$ eV could explain the observed results.

2

A Storage System for MAGIC

2.1 Data Requirements fro the MAGIC experiment

MAGIC belongs to the latest generation IACTs; such detectors are characterized by a high sensitivity. MAGIC is also the IACT with the lowest energy threshold, thanks to the large diameter (17 m) of its reflectors and to its high quantum efficiency photomultipliers. The low energy threshold of the telescopes can be further reduced when the so-called *Sum Trigger* [Cort09] is used. Thanks to this trigger, the MAGIC telescope has been able to reach an energy threshold of only 25 GeV and has detected for the first time the VHE pulsed emission from the Crab Nebula pulsar [MAG08a] above 30 GeV.

The MAGIC low energy threshold results in high event rates that impose demanding requirements both on the data acquisition system (DAQ) and on the data storage devices. The DAQ of MAGIC stores the complete waveform from all the pixels in the camera. The sampling is done using 10 bits and a sampling rate of 2 GHz [Goebel07]. A total of 50 samples per event and pixel are stored. The total size of an event is 60.7 kByte and the average trigger rate is around 300 Hz. The average raw data volume is around 21 MByte/s. Sum trigger observations can increase the trigger rate above $\sim$1 kHz. In that case, the raw data volume reaches 60 MByte/s and one night of observation can exceed 1 TByte of data for a single telescope.

The DAQ is only one of the processes with high demanding requirements in terms of storage. Other processes executed at the telescope site need access to the written data and also have important I/O requirements. During observation, the on-line analysis program produces a fast analysis using the data just being taken. To perform this task, the on-line analysis software accesses the raw data a few seconds after they have been written to the

disks. Events are processed at a speed similar to that of the DAQ, thus requiring a reading performance comparable to the writing performance needed by the DAQ.

The large data volumes generated by the MAGIC telescopes cannot be transferred directly through network to the datacenter [Rei09], but have to be processed first. Data are first compressed to reduce their volume in disk (factor ∼3.1 reduction) and later taped. Several CPU cores are used in parallel to perform the compression of the data, so the speed of the compression process is usually limited by the I/O speed of the disks where the raw data are stored. Taping is done in order to have a backup copy of the data and to transfer the data to the datacenter. The taping process requires a speed up to 60 MByte/s (MAGIC-I uses LTO3 tapes).

In order to make the data available as soon as possible, the on-site analysis software performs the calibration of the data also at the telescope site. Calibrated data (factor ~ 30 reduced in comparison to raw data) can hence be easily transferred to the datacenter using a fast network connection. Typically, calibrated data is available at the datacenter less than 24 hours after the data taking is finished. Calibration and data transfer are two of the most demanding processes in terms of I/O performance. The read and write disk speed must be as high as possible in order not to be limited by the disk access. These processes are also quite demanding in terms of CPU and typically several instances of the on-site analysis and the data transfers must be executed in several CPU cores.

The second MAGIC telescope [Cort09] (currently under commissioning) is equipped with 1039 pixels and the DAQ works also with a sampling rate of 2 Gsamples/s. As a result, the event size increases to ∼110 kByte, doubling the expected data volumes. Similar processes as those described for the first MAGIC telescope have to be executed for the data coming from the second MAGIC telescope, the difference being the data flow and the CPU needed to process the double amount of data. Although the storage systems for MAGIC-I and MAGIC-II data can be completely independent, a system where both telescopes are integrated would allow us to dynamically choose which resources (CPUs or storage) are to be used in each telescope.

Many of the MAGIC requirements can be provided by a Storage Area Network (SAN) solution. A SAN is an architecture to attach remote computer storage devices to servers, such that the devices appear as locally attached to the operating system. This can provide

the required high I/O performance but does not solve the problem of offering a consistent view of the file system to all computers directly attached to the storage devices. In addition, the required solution should also be flexible and scalable in order to accept the changes that will be introduced when the second telescope starts its operation.

2.2 The Red Hat Cluster Suite and the GFS Filesystem

When two or more computers work together to perform the same task they form a cluster. Clusters of computers are built to provide storage, high availability, load balance and/or high performance. In the case of MAGIC, a cluster of computers is used to provide a consistent file system image across the servers in the cluster. All members of the clusters (nodes) have simultaneous read and write access to a shared file system. The storage cluster solution used in MAGIC uses the Red Hat Cluster Suite (RHCS) [RHCS] and the Red Hat Global File System (GFS) [GFS].

The RHCS is an integrated set of software that can be configured to suit the needs of each cluster system. RHCS provides the basic functionality for the nodes to work together: configuration-file management, membership management, lock management and fencing. This functionality is provided by the different daemon process executing in all nodes: CCSD, CMAN, LOCKD and FENCED.

- CCSD manages the cluster configuration, making sure that all cluster members have the same cluster configuration. Changes in the cluster configuration can be propagated to all nodes by the CCSD.

- CMAN manages cluster quorum an cluster membership. CMAN keeps track of cluster quorum by monitoring the number of cluster nodes. When more than half of the nodes are active the cluster reaches quorum. When the cluster does not have quorum all cluster activity is blocked, preventing the cluster fragmentation that could lead in a storage cluster to data corruption in the file system. Membership is tracked by monitoring the messages that the nodes exchange. These messages are communicated between nodes via Ethernet.

- LOCK is a service that provides the mechanism to synchronize access to shared resources. In the RHCS the Distributed Lock Manager (DLM) is the lock manager.

It runs in each cluster node, distributing the lock management across all nodes in the cluster.

- FENCED manages the disconnection of a node from a cluster shared storage, cutting I/O from shared storage and ensuring data integrity. When a CMAN process determines that a node has failed this information is communicated to all nodes. When notified, the fenced daemon fences the failed node. Different fencing methods exist to guarantee that the fenced node does not have access to the shared storage. Two of the most widely used fencing methods are *Power fencing* (power off the failed device), *Fibre Channel switch fencing* (close the Fibre Channel switch port of the failed node).

On top of the cluster services the GFS can be installed (see Fig. 2.1). GFS is a native file system directly connected to the Linux kernel file system interface. Although GFS can work in a stand alone node, it shows all its capabilities when implemented as a cluster file system. GFS provides data sharing among GFS nodes in a cluster, providing a single, consistent view of the file system. With GFS, applications running on different nodes can share files in the shared storage in the same way as applications running in the same machine can share files in a local file system (Fig. 2.1).
Finally, GFS can be deployed in a variety of configurations that can fit any user needs. This is an open source solution supported by different widely used Linux distributions like RHEL or Scientific Linux. This solution is also highly flexible and can be easily scaled as new needs appear.

2.3 Implementation in MAGIC

MAGIC has implemented at the telescope site a SAN solution with Fibre Channel technology that uses the RHCS cluster suite and the GFS file system. At present seven nodes running Red Hat Enterprise Linux (RHEL) 4.3 and Scientific Linux (SL) 4.4 are members of the cluster. At a low level, the connection between the cluster nodes and the storage devices is done using Fibre Channel technology.
MAGIC has installed 4 RAID (Redundant Array of Independent Disks) systems with capacities between 7 and 21 TByte. The RAID units consist of several physical SATA disks

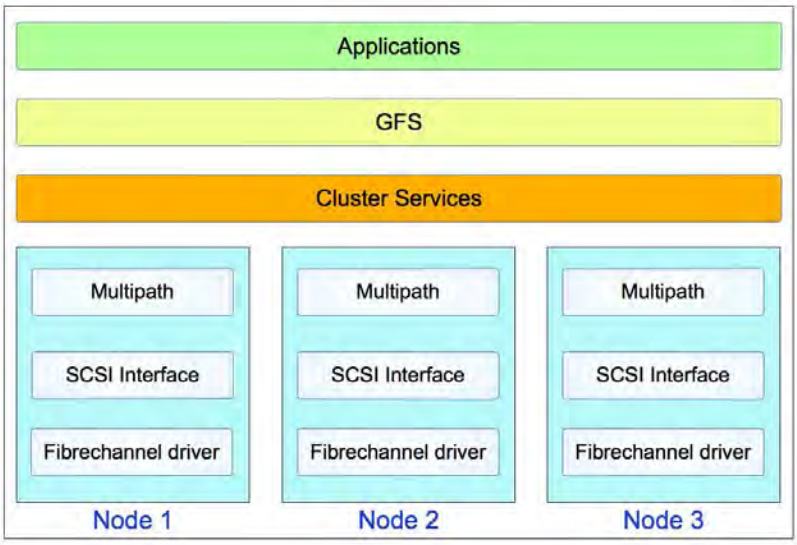

Figure 2.1: Software layers involved in the SAN storage solution with GFS implemented for MAGIC.

configured in RAID5 (redundancy based on parity data distributed across all member disks), which offers redundancy without sacrificing much of the I/O performance. Maximum read/write (R/W) speed of the RAID systems is between 250 and 300 MByte/s. The RAID systems are equipped with two Fibre Channel interfaces each.

The speed of the Fibre Channel connection is 2 or 4 Gbps (250 and 500 MByte/s) for the different RAID systems and nodes. All devices in the storage network are connected to Fibre Channel switches that are configured to work in a fabric topology. A total of three switches are used in our current configuration to guarantee the access to the storage devices in case of a switch failure. The switches can be cascaded if a special license is purchased. Currently only two of the switches are connected (see Fig. 2.2).

The RHCS-GFS suite has been installed in all nodes as well as the tools and drivers needed for the Fibre Channel connections. Currently the system is running using the same RHCS and GFS versions installed in two different Linux distributions and different kernel versions. The software structure is organized as follows. At the lowest level the Fibre Channel driver connects the nodes to the switches and the storage devices. The

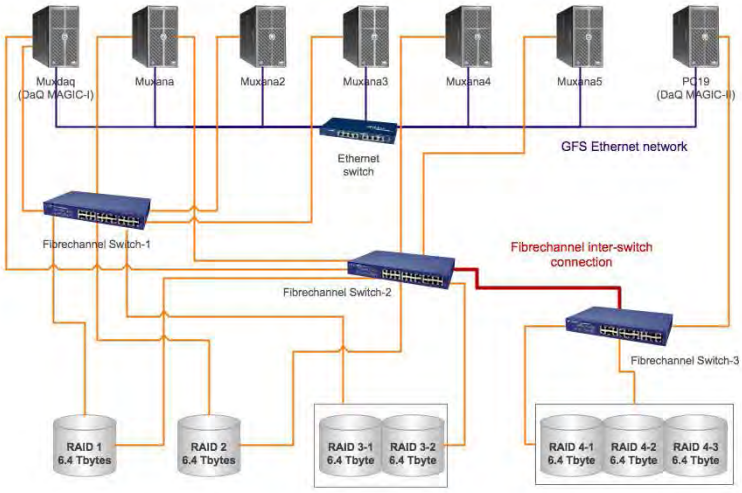

Figure 2.2: Topology of the Fibre Channel storage network. Most nodes are equipped with one single Fibre Channel interface but all RAID systems are equipped with two interfaces to achieve higher reliability and performance. Cluster messages among the nodes are exchanged through a dedicated ethernet network.

operating system can access the devices as SCSI devices directly attached to the node. The multipath service combines all different routes to the same device under a common device. The cluster services of the RHCS run on each node providing all services needed for the GFS layer. The GFS provides the consistent view of the file system to all nodes in the cluster, mounting the device provided by multipath and formatted with the GFS file system. The different applications are executed in each node.

The storage cluster is composed of seven nodes. Due to GFS layer the maximum R/W speed in the RAID systems is limited to only ∼200 MByte/s for a single RAID system. Different nodes can have access at the highest rates to different RAID systems simultaneously. The RAID systems with higher capacities are subdivided in partitions with the same size as the smallest RAID systems (∼ 6.4 Tbytes/partition). This size was limited by the first GFS version installed in the system. The seven nodes contain 42 cores that have direct access to storage devices and share the same consistent view of the file system. All messages exchanged by the CMAN daemon are transmitted through a dedicated 1 Gbps ethernet network and a dedicated ethernet adaptor in each node.

2.4 Performance

Additional aspects that were considered when adapting this solution include the reliability, the flexibility and the scalability of the system. The GFS solution implemented in MAGIC offered excellent characteristics in all these aspects.

2.4.1 Reliability

At the lowest level, the RAID units are configured in RAID5 which guarantees that no data is lost when one of the disks in the RAID units fails. The control software of the RAIDs uses the units configured as spares in the RAID when a disk failure occurs.

At the Fibre Channel level, a failure in one of the connections or in a full switch can be handled by the multipath daemon. When a node or a storage device has more than one Fibre Channel interface, different routes exist to access the same device. The multipath daemon unifies all possible paths to a storage device as one unique device. In case of a failure, multipath automatically routes the traffic using the working paths without any action required. Three Fibre Channel switches are used also to provide higher reliability.

Node failures are handled by the CMAN service, part of the RHCS. When a node failure happens the FENCE service blocks all nodes access to the shared storage units until the non-responding node is blocked. This is done to prevent data corruption in the file system. The fencing of a node is done in our implementation by closing the ports in the Fibre Channel switches where that node is connected. This guarantees that the non-responding node cannot access the RAID disks. After the node is fenced, the access to the RAIDs system is enabled again for all members of the cluster. The time needed for this operation is of only a few seconds and it is automatically handled by the CMAN and fence services.

2.4.2 Flexibility

Cluster configuration is contained in a single file that is identical in all nodes belonging to the cluster. Any change in the cluster configuration (like adding a new node) can be easily propagated to all nodes in the cluster with the CCSD daemon.

Since all nodes have direct R/W access to the GFS file systems, applications running in any node can choose where to read or write data. This allows for the dynamical choice

regarding how many applications are needed for each task and where they have to be executed, and provides a high flexibility that could not be reached with other solutions.

2.4.3 Scalability

This system can be easily extended by adding either more nodes or more storage devices. At present, less than 30% of the Fibre Channel switch ports are used. The Fibre Channel devices use the fabric topology making it possible to add more nodes or storage devices just by plugging them to a new port in the switch.

Adding more nodes to the storage cluster is also not a problem. At present seven nodes are connected and is planned to add more nodes to the cluster. The only limitation when adding more nodes is that the GFS file system must have a number of journals equal or larger than the number of nodes connected. That number is configured when the GFS partition is formatted. GFS supports over 100 nodes.

2.5 Conclusions

The MAGIC detector at La Palma has discovered many new sources and classes of sources, both galactic and extragalactic. Thanks to its low energy threshold, the lowest among Cherenkov telescopes, it can contribute to many new discoveries, also in the field of fundamental physics.

The high demands that the data taking and the data process impose on the on site storage systems used in the MAGIC telescopes have been addressed using the RHCS and the distributed filesystem GFS. This Linux open source solution offers a consistent view of the file system and high I/O performance since all nodes in the cluster have direct access to the storage devices. It also provides high reliability and high flexibility that allows us to allocate resources dynamically where they are more needed or to change the configuration if a failure in a node or a storage device occurs. The system is also designed to provide easy scalability in the midterm future when new needs appear in the MAGIC-II phase of the experiment when the upgrade to stereoscopy is guaranteeing since end 2009 a further improvement in data quality.

Bibliographies

Bibliography for the First Part

[AbGue05] R. de Abreu and V. Guerra, *Einstein's lost frame* E]m[Lisboa 2005, and references therein

[Adl04] S.L. Adler, "Remarks on the History of Quantum Chromodynamics" arXiv:hep-ph/0412297 (2004)

[AK82] S. Akoi et al., Astron. Astrophys. 105 (1982) 359

[Aml08] C. Amsler et al., (Particle Data Group), Phys. Lett. B 667 (2008) 1

[Anton05] P. Antonini et al., Phys. Rev. A 71 (2005) 050101

[Aron83] S.H. Aronson et al., Phys. Rev. D 28 (1983) 476

[AVS98] R. Anderson, I. Vetharaniam and G.E. Stedman, Phys. Rep. 295 (1998) 93

[Bail77] J. Bailey et al., Nature 268 (1977) 301

[BCP58] E. Boldt, D.O. Caldwell, Y. Pal, Phys. Rev. Lett. 1 (1958) 150

[Belt05] P. Beltrame, Diploma Thesis, Università degli Studi di Roma La Sapienza (2005)

[Bergia00] S. Bergia, G. Fis. 41 (2000) 13

[BerGui98] S. Bergia and M. Guidone, Found. Phys. Lett. 11 (1998) 549

[BeVa98] S. Bergia and M. Valleriani, G. Fis. 39 (1998) 199

[Bluhm03] R. Bluhm et al., Phys. Rev. D68 (2003) 125008

[BoGi00] I. Bonizzoni and G. Giuliani, "The interpretations by experimenters of experiments on time dilation: 1940-1970 circa" arXiv:physics/0008012 [physics.hist-ph]

[Brax01] C. Braxmaier et al., Phys. Rev. Lett. 88 (2001) 010401

[BrilHall79] A. Brillet and J.L. Hall, Phys. Rev. Lett. 42 (1979) 549

[Buf89] P. Buffet-Smith, *Practical astronomy with your calculator*, Cambridge Cambridge University Press (1989)

[Cab63] N. Cabibbo, Phys. Rev. Lett. 10 (1963) 531

[Cah04] R.T. Cahill, "Absolute motion and gravitational effects", Apeiron 11 (2004) 53

[Cah07] R.T. Cahill, "Dynamical 3-Space: A Review" arXiv:0705.4146v2 [physics.gen-ph]

[Christ64] J.H. Christenson et al., Phys. Rev. Lett. 13 (1964) 138

[ChaMo61] D.C. Champeney and P.B. Moon, "Absence of Doppler Shift for Gamma Ray Source and Detector on Same Circular Orbit", Proc. of the Physical Society 77 (1961) 350

[ChIK63] D.C. Champeney, G.R. Isaac and A. M Kahn, Phys. Lett. 7 (1963) 241

[ColKos97] D. Colladay and V.A. Kostelecký, Phys. Rev. D 55 (1997) 6760

[ColKos98] D. Colladay and V.A.Kostelecký, Phys. Rev. D 58 (1998) 116002

[Dam97] T. Damour, "Gravity, Equivalence Principle and Clocks" arXiv:gr-qc/9711060v1

[DeSm96] A. De Angelis and B. Smalska, "Search for Intrinsic Anisotropies of Time Dilation", DELPHI note 1996 141 PHYS 640 (1996)

[Dreu09] M. Dreucci, Proc. of the EPS-HEP 2009 Krakow, Poland (2009) 198

[DrYan79] M. Dresden and C. N. Yang, Phys. Rev. D 20 (1979) 1846; J. J. Sakurai, Phys. Rev. D 21 (1980) 2993

[Dyson03] F. Dyson, The New York Review of Books 50 (2003)

[Einst1905] A. Einstein, "Zur Elektrodynamik bewegter Körper " Ann. Phys. 17 (1905) 891 English translation in *The Principle of Relativity* London Methuen and Company (1923)

[Eisl57] F. Eisler et al., Phys. Rev. 108 (1957) 1353

[EuKo35] H. Euler and B. Kochel, Naturwissenschaften 23 (1935) 246

[Feyn63] R.P. Feynman, *Lectures on Physics* vol 1 , New York Addison Wesley (1963)

[Field05] J.H.Field, "Proposals for Two Satellite-Borne Experiments to Test Relativity of Simultaneity in Special Relativity" arXiv:physics/0509213v3 [physics.gen-ph]

[Fix83] D.J. Fixsen et al., Phys. Rev. Lett. 50 (1983) 620

[Fra92] P. Franzini, "Predicting the statistical accuracy of an experiment" The DAPHNE physics handbook, 1 (1992) 15; F. Ambrosino et al (KLOE Collaboration) JHEP 073 (2008) 0801

[FX00] H. Fritzsch and Z-Z. Xing, Prog. Part. Nucl. Phys. 45 (2000) 1

[Gal1632] G. Galilei, *Dialogo (...) sopra i due massimi sistemi del mondo tolemaico e copernicano* Firenze (1632)

[GaPu05] R. Gambini and J. Pullin, Phys. Rev. D 59 (1999) 124021

[Garw57] R.L. Garwin, L.M. Lederman and M. Weinrich, Phys. Rev.105 (1957) 1415

[Gatti02] C. Gatti, Diploma Thesis, Università degli Studi di Pisa (2002)

[Gatti06] C. Gatti, Eur. Phys. J. C 45 (2006) 417

[GEANT78] R. Brun, et al., GEANT *Simulation program for particle physics experiments, user guide and reference manual*, CERN-DD-78-2-REV (1978)

[GEANT84] R. Brun, et al., GEANT3 CERN-DD/EE/84-1 (1984)

[GelMa64] M. Gell-Mann, Phys. Lett. 8 (1964) 214

[GelMaPa55] M. Gell-Mann and A. Pais, Phys. Rev. 97 (1955) 1387

[Glash61] S. L. Glashow, Nucl. Phys. 22 (1961) 579

[Govor09] L.I. Govor et al., Phys. Atom. Nucl. 72 (2009) 561

[Green02] O.W. Greenberg, Phys. Rev. Lett. 89 (2002) 231602

[Gwin05] G. Gwinner, Mod. Phys. Lett. A 20 (2005) 791

[HafKea72] J.C. Hafele and R.E. Keating, Science 177 (1972) 166

[Hafele72] J.C. Hafele, Am. J. Phys. 40 (1972) 81

[Haz79] R. Hazelett and D.Turner, *The Einstein Myth and the Ives Papers: A Counter-Revolution in Physics* Old Greenwich The Devin-Adair (1979)

[Herr05] S. Herrmann et al., Phys. Rev. Lett. 95 (2005) 150401

[Herr06] S. Herrmann et al., Lect. Notes Phys. 702 (2006) 385

[Herr09] S. Herrmann et al., Phys. Rev. D 80 (2009) 105011

[HilsH90] D. Hils and J.L. Hall, Phys. Rev. Lett. 64 (1990) 1697

[IvSt38] H.E. Ives and G.R. Stilwell, J. Opt. Soc. Am. 28 (1938) 215

[Jarlsk85] C. Jarlskog, Phys. Rev. Lett. 55 (1985) 1039

[Kajari09] E. Kajari et al., "Rotation in relativity and the propagation of light" arXiv:0905.0765v1 [gr-qc]

[KenTh32] R.J. Kennedy and E.M. Thorndike, Phys. Rev. B 42 (1932) 400

[KLOE95] M. Greco et al., The Second DAΦNE Physics Handbook SIS-Pubblicazioni Frascati (1995) 629

[KLOE04] F. Ambrosino et al. (KLOE Collab.), Nucl. Inst. Meth. A 534 (2004) 403

[KLOE06] F. Ambrosino et al. (KLOE Collab.), Phys. Lett. B 636 (2006) 173

[KLOE08] F. Bossi et al. (KLOE Collab.), Riv. Nuovo Cim. 31 (2008) 531 and references therein

[KLOE10a] KLOE Collaboration, "Measurement of K_S^0 lifetime from KLOE data", to appear (2010)

[KLOE10b] KLOE Collaboration, Private Note (2010)

[KM73] M. Kobayashi and T. Maskawa, Prog. Theor. Phys. 49 (1973) 652

[KoLa99] V.A. Kostelecký and C. Lane, Phys. Rev. D 60 (1999) 116010

[KostRus10] V.A. Kostelecký and N. Russell, "Data Tables for Lorentz and CPT Violation" arXiv:0801.0287v3 [hep-ph]

[KosMe02] V.A. Kostelecký and M. Mewes, Phys. Rev. D66 (2002) 056005

[KosSam89] V.A. Kostelecký and S. Samuel, Phys. Rev. D 39 (1989) 683

[Kosto04] V.A. Kostelecký, Phys. Rev. D 69 (2004) 105009

[Kuhn70] T.S. Kuhn, *The Structure of Scientific Revolutions* Chicago University of Chicago Press (1996)

[Land57] L.D. Landau, Zh. Eksp. Teor. Fiz. 32 (1957) 405

[LeYo56] T.D. Lee and C.N. Yang, Phys. Rev. 104 (1956) 254

[Lipa03] J.A. Lipa et al., Phys. Rev. Lett. 90 6 (2003) 060403

[Lub83] P.M Lubin et al., Phys. Rev. Lett. 50 (1983) 616

[Mac86] D.W. MacArthur, Phys. Rev. A 33 (1986) 1

[MaSe77a] R. Mansouri and R.U. Sexl, Gen. Relativ. Gravit. 8 7 (1977) 497

[MaSe77b] R. Mansouri and R.U. Sexl, Gen. Relativ. Gravit. 8 7 (1977) 515

[MaSe77c] R. Mansouri and R.U. Sexl, Gen. Relativ. Gravit. 8 10 (1977) 809

[Mash98] B. Mashhoon et al., Phys .Lett. A 249 (1998) 161

[Mill33] D.C. Miller Rev. Mod. Phys. 5 (1933) 203

[MiMo1887] A.A. Michelson and E.W. Morley, Amer. Jour. of Sci. 34 (1887) 1333

[Mul02] H. Müller et al., Int. J. Mod. Phys. D 11 (2002) 1101

[Mull03a] H. Müller et al., Phys. Rev. Lett. 91 2 (2003) 020401

[Mull03b] H. Müller, et al., Phys. Rev. D 67 (2003) 056006

[Mull03c] H. Müller et al., Phys. Rev. D 68 (2003) 116006

[Mull05] H. Müller, Phys. Rev. D 71 (2005) 045004

[PDG06] W. M. Yao et al. (Particle Data Group), J. Phys. G33 (2006) 1

[PDG08] C. Amsler et al. (Particle Data Group), Physics Letters B667 (2008) 1 and 2009 partial update for the 2010 edition

[Quigg01] C. Quigg, arXiv:hep-ph/0204104v1

[ReBr04] M.J. Reid and A. Brunthaler, Astrophys. J. 616 (2004) 872

[Rei05] S.B. Reinhardt, Phd Thesis University of Heidelberg (2005)

[Riis88] E. Riis et al., Phys. Rev. Lett. 60 (1988) 81

[RiRuSe04] G. Rizzi, M.L. Ruggiero and A. Serafini, Found. Phys. 34 (2004) 1835 and references therein

[RiSe04] G. Rizzi, A. Serafini, *Relativity in Rotating Frames* in "Fundamental Theories of Physics" Dordrecht Kluwer Academic Publishers (2004)

[Rob06] T.J. Roberts, arXiv:physics/0608238v3 [physics.class-ph]

[Rob08] T. J. Roberts, `www.math.ucr.edu/home/baez/physics/Relativity/SR/experiments.html` April 30th 2010

[Robn49] H.P. Robertson, Rev. of Mod. Phys. 21 3 (1949) 378

[RoHa41] B. Rossi and D.B. Hall, Phys. Rev. 59 (1941) 223

[Russel06] N. Russell, "The Standard-Model Extension and Tests of Relativity" arXiv:hep-ph/0612367v1

[Saat03] G. Saathoff et al., Phys. Rev. Lett. 91 (2003) 190403

[Sagn13] G. Sagnac C. R. Acad. Sci., Paris 157 (1913) 708

[Sarg] S. Sarg, www.helical-structures.org/new_evidences/modern-ether-drift-exp/ether-drift-exp.pdf April 30th 2010

[Sar96] L. Sartori, *Understanding Relativity. A Simplified Approach to Einstein's Theories* Berkeley University of California Press (1996)

[Sel96] F. Selleri, Found. Phys. 26 (1996) 641

[Sel98] F. Selleri, *La scienza e i vortici del dubbio* Napoli Edizioni Scientifiche Italiane (1998);
F. Selleri in *Open questions in Relativistic Physics"*, Proc. of Special Relativity and Some of its Applications Montreal, ed. F. Selleri, Apeiron (1998)

[Sel99] F. Selleri, G. Fis. 40 (1999) 19

[Sel03] F. Selleri, "Lezioni di relatività. Da Einstein all'etere di Lorentz", Bari Progedit (2003)

[Sel04] F. Selleri, Apeiron 11 (2004) 246

[SmGoMu77] G.F. Smoot, M.V. Gorenstein and R.A. Müller Phys. Rev. Lett. 39 (1977) 898

[Smoot07] G.F. Smoot, Rev. Mod. Phys. 79 4 (2007) 1349

[SolEin87] M.Solovine and A. Einstein, *Letters to Solovine* New York Philosophical Library (1987) Originally published in French: *Lettres Maurice Solovine* Paris Gauthier-Villars (1956)

[Stan05] P.L. Stanwix, et al., Phys. Rev. Lett. 95 (2005) 040404

[Stan06] P.L. Stanwix et al., Phys. Rev. D 74 (2006) 081101

[Sted97] G.E. Stedman, Rep. Prog. Phys 60 (1997) 15

[Tobar05] M.E. Tobar et al., Phys. Rev. D 71 (2005) 025004

[Tobar09] M.E. Tobar et al., Phys. Rev. D 81 2010 022003

[Weyl83] H. Weyl, *Symmetry* Princeton Princeton University Press (1983)

[Will01] C.M. Will, *The Confrontation between General Relativity and Experiment* Living review `relativity.livingreviews.org` 4 (2001)

[Will05] C.W. Will, *Einstein, 1905-2005: PoincaréSeminar* 2005 Basel Birkhauser (2006)

[Will92] C.M. Will, Phys. Rev. D 45 (1992) 403

[Will93] C.M. Will, *Theory and Experiment in Gravitational Physics* Cambridge Cambridge University Press (1993)

[Wolf03] P. Wolf et al., Phys. Rev. Lett. 90 (2003) 060402

[Wolf04a] P. Wolf et al., Gen. Relativ. Gravitat. 36 10 (2004) 2351

[Wolf04b] P. Wolf et al., Phys. Rev. D 70 (2004) 051902

[Wolf06] P. Wolf et al., Lect. Notes Phys. 702 (2006) 451

[Wolfs83] L. Wolfenstein, Phys. Rev. Lett. 51 (1983) 1945

[WoPe97] P. Wolf and G. Petit, Phys. Rev. A 56 (1997) 4405

[Wor09] E.T. Worcester, To be published in Proc. of DPF-2009, Detroit MI, July 2009 arXiv:0910.3160v1 [hep-ex]

[Wu57] C.S. Wu e al., Phys. Rev. 105 (1957) 1413

[Zha97] Y.Z. Zhang, *Special Relativity and Its Experimental Foundations* Singapore World Scientific Pub (1997)

Bibliography for the Second Part

[AC98] G. Amelino-Camelia et al., Nature 393 (1998) 763

[Bast05] D. Bastieri et al., Astropart. Phys. 23 (2005) 572

[CoAh97] P. Coppi and F. Aharonian, Astrophys. J. 487 (1997) L9

[Cort09] J. Cortina et al., Proc. of the 31^{st} ICRC (2009) arXiv:0907.1211v1 [astro-ph.IM]

[DAMaPe08] For a review on the Cherenkov technique and experiments see for example A. De Angelis, O. Mansutti and M. Persic, Riv. Nuovo Cim. 31 (2008) 187

[DARMa07] A. De Angelis, M. Roncadelli and O. Mansutti, Phys. Rev. D76 (2007) 121301; A. De Angelis et al., Mon. Not. R. Astron. Soc. 394 (2009) L21 (updated in M. Roncadelli et al., Contribution to SciNeGHE 2009, to appear in the Proceedings)

[DMP] `www.mppmu.mpg.de/~rwagner/sources/` and references therein April 30th 2010

[Ellis09] J. Ellis et al., Phys. Lett. B674 (2009) 83

[FaSte71] G.G. Fazio and F.W. Stecker, Nature 226 (1970)135

[FERMI09a] A.A. Abdo et al. (Fermi Coll.), Science 323 (2009) 1688

[FERMI09b] A.A. Abdo et al. (Fermi Coll.), Nature 462 (2009) 331

[GFS] GFS On Line Documentation
`www.redhat.com/docs/en-US/Red_Hat_Enterprise_Linux/5.4/pdf/Global_File_System.pdf`

[Goebel07] F. Goebel et. al., Proc. of the 30^{th} ICRC, (2007)

[HEG01] F.A. Aharonian et al. (HEGRA Coll.), Astron. Astrophysics 112 (2001) 307.

[HESS09] V.A. Acciari et al. (H.E.S.S., MAGIC, VERITAS and VLBA Coll.), Science 325 (2009) 444

[LOM09] S. Lombardi for the MAGIC Collaboration, Contribution to the XXXI ICRC, Lodz 2009

[MAG06a] J. Albert et al. (MAGIC Coll.), Science 312 (2006) 1771

[MAG06b] J. Albert et al. (MAGIC Coll.), Astrophys. J. 642(2006) L119

[MAG06c] J. Albert et al. (MAGIC Coll.), Astrophys. J. 648 (2006) L105

[MAG07a] J. Albert et al. (MAGIC Coll.), Astrophys. J. 664 (2007) L87

[MAG07b] J. Albert et al. (MAGIC Coll.), Astrophys. J. 665 (2007) L51

[MAG07c] J. Albert et al. (MAGIC Coll.), Astron. Astrophysics 474(2007) 937

[MAG07d] J. Albert et al. (MAGIC Coll.), Astrophys. J. 666 (2007) L17

[MAG07e] J. Albert et al. (MAGIC Coll.), Astrophys. J. 667(2007) L21

[MAG07f] J. Albert et al. (MAGIC Coll.), Astrophys. J. 654 (2007) L119

[MAG08a] E. Aliu et al. (MAGIC Coll.), Science 322 (2008) 1221

[MAG08b] J. Albert et al. (MAGIC Coll.), Astrophys. J. 684 (2008) 1351

[MAG08c] J. Albert et al. (MAGIC Coll.), Science 320 (2008) 1752

[MAG08d] J. Albert et al. (MAGIC Coll.), Phys. Lett. B668 (2008) 253

[MAG09] J. Albert et al. (MAGIC Coll.) Astrophys. J. 693 (2009) 303

[MAG09] E. Aliu et al. (MAGIC Coll.), Astrophys. J. 692 (2009) L29

[Rei09] I. Reichardt et al. *The MAGIC DataCenter*, Proc. of the 31^{st} ICRC, 2009

[RHCS] RHCS On Line Documentation
`www.redhat.com/docs/en-US/Red_Hat_Enterprise_Linux/5.4/html/Cluster_Administration/index.html` April 30th 2010

[Tesh08] M. Teshima et al. (MAGIC Coll.), ATel 1500 (2008)

List of Collaboration Publications by MAGIC

[1] MAGIC Collaboration, "Gamma-ray excess from a stacked sample of high-frequency peaked blazars observed with the MAGIC telescope" arXiv:1002.2951 (2010)

[2] MAGIC Collaboration, "MAGIC TeV Gamma-Ray Observations of Markarian 421 during Multiwavelength Campaigns in 2006" arXiv:1001.1291(2010)

[3] MAGIC Collaboration, "Simultaneous multi-frequency observation of the unknown redshift blazar PG 1553+113 in March-April 2008" arXiv:0911.1088 (2009)

[4] MAGIC Collaboration, Astrophys. J. 706 L27 (2009)

[5] MAGIC Collaboration, Astrophys. J. 710 (2010) 634

[6] MAGIC Collaboration, AIP Conf. Proc. 1018 (2008) 180

[7] MAGIC Collaboration, Astrophys. J. Lett. 692 (2009) 29

[8] MAGIC Collaboration, Astroparticle Physics 30 (2009) 293

[9] MAGIC Collaboration, Astrophys. J. 697 (2009) 1299

[10] MAGIC Collaboration, "A novel background reduction strategy for high level triggers and processing in gamma-ray Cherenkov detectors" AIP Conf. Proc. 1018 (2008) 180 arXiv:0804.3896

[11] MAGIC Collaboration, "Monte Carlo Simulation for the MAGIC-II System" Contribution to the 30th ICRC, Merida, Mexico, July 2007 arXiv:0709.2959